ISOBARIC YIELD DISTRIBUTION IN PROTON-INDUCED FISSION OF URANIUM

S.S. Parikh

ISOBARIC YIELD DISTRIBUTION IN FISSION OF URANIUM BY 20-85 MeV PROTONS

by

Sarvabhaum S. Parikh, M.Sc. (Ohio State U.)

A thesis submitted to the Faculty of Graduate Studies and Research in partial fulfilment of the requirements for the degree of Doctor of Philosophy

Department of Chemistry,
McGill University,
Montreal.

March 1966.

Ph.D. Chemistry

Sarvabhaum S. Parikh

ISOBARIC YIELD DISTRIBUTION IN FISSION OF URANIUM BY 20-85 MeV PROTONS

A B S T R A C T

The independent formation cross-sections of ^{139}Ba, ^{139}Ce, ^{141}La, ^{141}Ce, and ^{143}Ce and the cumulative formation cross-sections of ^{139}Cs, ^{141}Ba, and ^{143}La produced in the fission of natural uranium by protons of energies 20-85 MeV have been measured radiochemically. Excitation functions were constructed and the proton energies at which the excitation functions reach their maxima fall on a smooth curve when plotted against neutron-to-proton ratio of the product. Nuclear charge dispersion curves were constructed at 20, 30, 40, 50, 60, 70, 80, and 85 MeV. The general behaviour is similar to that observed by previous workers. With increasing proton energy the curves broaden and the most probable charge approaches the line of beta-stability. These phenomena are qualitatively explained in terms of neutron evaporation. Experimental yields showed good agreement when compared with Wahl's empirical charge distribution curve. It seems that charge dispersion can be very adequately represented in the form of a Gaussian distribution.

ACKNOWLEDGEMENTS

The author gratefully acknowledges his indebtedness to the following persons and institutions:

Professor L. Yaffe for his guidance and constant encouragement throughout the course of this work.

Dr. N.T. Porile for his helpful direction.

Dr. D.A. Marsden for his advice and for many valuable discussions.

Dr. G.B. Saha, Messrs. D.R. Sachdev, M.K. Dewanjee and all other members of the Radiochemistry Laboratory for their help in many ways.

Dr. R.E. Bell, Director of the Foster Radiation Laboratory, McGill University, for permission to use the cyclotron facilities, and Mr. R.H. Mills for his cooperation and assistance in carrying out the bombardments.

Mrs. C. Macfarlane for excellent typing of this thesis and her painstaking pursuit of grammatical errors, and Mr. P. Shah for his proof reading.

My wife, Jyotsna, for her patience and encouragement during the course of this work.

The Chemistry Department of McGill University for Demonstratorships and for National Research Council support.

TABLE OF CONTENTS

I. INTRODUCTION

I-A. GENERAL

The work of Fermi and his collaborators[1] on the interaction of neutrons with heavy nuclei and resultant production of new radioactive species led Hahn and Strassmann[2] to show that, when neutrons react with uranium, elements with much smaller atomic weight and atomic number are formed. Meitner and Frisch[3] named this new type of reaction 'Fission', which is broadly defined as the break-up of a nucleus into two roughly equal fragments.

Fission can occur spontaneously or be induced. Spontaneous fission was first observed by Flerov and Petrzhak[4] in uranium. It is another mode of radioactive decay (different from alpha decay) of nuclides in their ground state with atomic numbers $\geqslant$ 90. Induced fission occurs when sufficient excitation energy is given to a nucleus by photons or particles of varying energy. The characteristics of this nuclear reaction depend upon the energy of the projectiles.

(1) Nuclear Reactions

Nuclear reactions are arbitrarily divided into low-, medium-, and high-energy reactions. Low-energy reactions are induced by projectiles with eneggy less than 40 MeV. The areas between 40 MeV and 100 MeV and that greater than 100 MeV are called medium- and high-energy reactions respectively.

(a) Low Energy Nuclear Reactions:

In order to explain the mechanism of nuclear reactions at low energies, N. Bohr[5] introduced the idea of a compound nucleus. When a projectile impinges upon a target nucleus, the incoming energy and momentum are shared among all the nucleons of the nucleus, resulting in a 'compound' nucleus. The excitation of this nucleus is equal to the kinetic energy of the projectile plus the binding energy of the incident particle. The mean lifetime of the compound nucleus is of the order of 10^{-14} to 10^{-17} seconds, which is quite long compared to the time required for a particle to traverse the nuclear diameter, about 10^{-22} seconds.

The decay of a compound nucleus is independent of its mode of formation but dependent upon its excitation energy, momentum and parity. A particle will be emitted only when it acquires sufficient energy (its binding energy plus energy to overcome the barrier) by random collisions among the nucleons. Therefore the formation cross-section can be expressed as

$$\sigma(A,B) = \sigma_c(A)\, P_c(B) \qquad (I\text{-}1)$$

where $\sigma_c(A)$ is the formation cross-section of the compound nucleus with projectile A, and $P_c(B)$ is the probability that the compound nucleus will de-excite by the emission of particle B. Furthermore, if we consider the cross-section for the emission of particle X from the above compound nucleus, and the emission of particles B and X from the same compound nucleus

formed by a different projectile D, and if the compound nucleus has the same excitation energy in each case, then the following expression should hold:

$$\frac{\sigma(A,B)}{\sigma(A,X)} = \frac{P_c(B)}{P_c(X)} = \frac{\sigma(D,B)}{\sigma(D,X)} \qquad \text{(I-2)}$$

where $P_c(X)$ is the probability of a compound nucleus de-exciting by the emission of a particle X.

Weisskopf[6] and Shapiro[7] gave a detailed mathematical treatment for compound nucleus formation and derived a formula to calculate the formation cross-section values.

Experimental evidence for the compound nucleus formation was supplied by Ghoshal.[8] He bombarded ^{60}Ni with alpha particles and ^{63}Cu with protons and formed ^{64}Zn compound nuclei in both cases. He found that the experimental cross-section values satisfy Bohr's prediction as given by the following equation:

$$\frac{\sigma(p,n)}{\sigma(\alpha,n)} = \frac{\sigma(p,2n)}{\sigma(\alpha,2n)} = \frac{\sigma(p,pn)}{\sigma(\alpha,pn)} \qquad \text{(I-3)}$$

John[9] further verified this in the same fashion. He obtained (α,xn) cross-section values by bombarding ^{206}Pb with alpha particles forming the ^{210}Po compound nucleus and compared his values with the (p,xn) cross-section values from ^{210}Po compound nucleus at the same excitation energy formed by Kelley[10] in his studies of ^{209}Bi with protons. He found

similar results as those reported by Ghoshal.

The prediction that the angular distribution of the emitted nucleons should be symmetric about 90^{o} in the centre-of-mass system was proved experimentally by Armstrong and Rosen[11] among others from their studies on different elements bombarded by 14 MeV neutrons.

Similarities in the shapes of energy spectra of emitted particles from the same compound nucleus formed in two different ways were shown by Sherr and Brady.[12] They studied the $^{59}Co(p,\alpha)^{56}Fe$ reaction and found the shapes of alpha-particle spectra similar to those from $^{56}Fe(\alpha,\alpha')^{56}Fe$ obtained by Lassen et al.[13] at the same energies.

(b) High Energy Nuclear Reactions:

As the energy of the projectile is increased, the compound nucleus mechanism does not explain all the observed characteristics of the reaction. At medium energies (40 MeV - 100 MeV), the reaction proceeds through both compound nucleus formation and the process called direct interaction. The latter process becomes increasingly prominent with increasing projectile energy and at high energies ($>$ 100 MeV) the reaction proceeds predominantly through the direct interaction mechanism.

Serber[14] suggested a two-step process to explain the direct interaction mechanism. First, direct nucleon-nucleon collision or cascade, which is a fast process, followed by nucleon evaporation, which is a slow process.

In the cascade, also called the knock-on, phase, the reaction is assumed to proceed through successive two-body collisions between the incident nucleon and the individual nucleons in the target nucleus. This assumption of Impulse Approximation (the collisions can be considered as those between free nucleons) is justifiable because the effective wave-length of the high energy incident nucleon is very small compared to the inter-nucleon distance. The incident nucleon has a long mean free path; therefore, either it may traverse through the target nucleus without suffering any collisions or it may make a collision with a nucleon in the nucleus. After the first collision, both or either of the collision partners may be emitted or further collide with other nucleons of the target nucleus, depending upon the kinematics and energetics of the process. In this way, an inter-nuclear cascade is generated and a few prompt nucleons with varying kinetic energy are emitted leaving residual nuclei in different excited states.

Since the collisions occur within nuclear matter, each cascade step is governed by (1) the Pauli exclusion principle which prohibits collisions leading to occupied states, (2) the momentum distribution of the nucleons in the nucleus, and (3) the change in the kinetic energy of the incident nucleon as it crosses the nuclear boundary of the target nucleus.

The cascade phase continues until prompt nucleons can no longer be emitted and a state of equilibrium is then

established through multiple collisions among the nucleons. Nuclei in this equilibrium state still possess sufficient excitation energy to evaporate one or more nucleons. This evaporation phase is a slow, random process and proceeds in much the same way as the de-excitation of the compound nucleus. The result of the cascade-evaporation process is a spectrum of the end-products.

Experimental evidence for the cascade-evaporation process is provided by several workers. For example, Meadows[15] bombarded copper with protons up to 100 MeV and found his results of (p,xn) and (p,pxn) excitation functions agreeing with compound nucleus formation only at low energies, but those at higher energies were in agreement with the cascade-evaporation mechanism.

When various elements were bombarded by protons of energies 18 MeV[16], 23 MeV[17], and 31 MeV[18], asymmetry in angular distribution of inelastically scattered protons was observed, and this was attributed to the direct interaction mechanism.

Caretto and Wiig[19] studied the absolute cross-sections for a number of nuclides formed by the action of 60-240 MeV protons on yttrium and explained qualitatively their results in terms of cascade-evaporation process.

(b) Monte Carlo Calculations:

The random nature of cascade and evaporation processes suggests the use of Monte Carlo calculations.

Goldberger[20] first tested quantitatively the cascade theory by using the Monte Carlo method. This method of calculation involves the use of various nuclear parameters, such as nuclear radius, the depth of the potential well, and cut-off energy. The nucleus is looked upon as a degenerate Fermi gas in a square potential well with a uniform density distribution. Several workers[21-25] have used this method for a variety of reaction conditions but with some refinements for the technique. The results of Metropolis et al.[24,25] are the most complete. They have calculated results for various target nuclei and several incident energies by following a large number of cascades for each set of initial conditions, giving better statistical accuracy than the previous calculations. They reported the calculated values of the distribution in atomic number, mass number and excitation energy of the residual nuclei. They also calculated type, number, energy, and angular distribution of the emitted particles.

Le Couteur[26] and Jackson[27], among others, have performed calculations of the evaporation process using Weisskopf's[6] evaporation formalism to compute analytically the average behaviour in the de-excitation process. Rüdstam[23] and Dostrovsky et al.[28,29] have also applied the Monte Carlo method to the evaporation calculations. This calculation involves the use of the mass number (A), nuclear charge (Z), and excitation energy of the original nucleus with appropriate selections of the nuclear radius, level density parameter, potential barrier, etc. The output of this calculation gives

the average nuclear charge and mass number of the product nuclei, and also the energies and multiplicities of the evaporated particles.

The probability of the formation cross-section of a nuclear reaction product is obtained by combining the results of the calculations of both the cascade and the evaporation processes. In general, the calculated values agree quite well with experimental results, except for a few discrepancies. For example, Metropolis et al.[24] and others[30,31] found that the calculated yields of the (p,pn) reaction are lower than the experimentally determined yields by a factor of two or three. They suggested that this may be due to faulty input information concerning the nuclear boundary, i.e. it should probably be a diffuse edge rather than a sharp boundary.

(2) Fission

(a) Fission Phenomena:

Fission of heavy elements induced at low energies proceeds predominantly through compound nucleus formation. For example, in thermal neutron fission of ^{235}U, the neutron is captured to form a compound nucleus in an excited state, which then undergoes fission. This process is represented by the following expression:

$$^{235}_{92}U + ^{1}_{0}n \rightarrow [^{236}_{92}U]^{*} \rightarrow ^{A_1}_{Z_1}X_1 + ^{A_2}_{Z_2}X_2 + \nu\, ^{1}_{0}n + \gamma + Q. \qquad (I\text{-}4)$$

In the above representation, $^{A_1}_{Z_1}X_1$ and $^{A_2}_{Z_2}X_2$ are the

primary light and heavy fragments respectively, formed in the fission process. ν is the total number of neutrons released. Most of these neutrons (99%) are emitted within about 10^{-14} seconds and are called prompt neutrons. About 1% of the total neutrons are emitted with gradually decreasing intensity for several minutes after the actual fission process, and these are known as delayed neutrons. The average number of neutrons emitted in each thermal neutron fission event is 2.5, and thus it can be seen that the fissioning nucleus divides itself in more than one way. γ is the energy released as electromagnetic radiation at the instant of fission. Q is the kinetic energy of the fission fragments and fission neutrons. The total energy released in the fission process is approximately 190 MeV.

In the above representation of the fission process, the laws of conservation of mass (A) and charge (Z) must be satisfied. Therefore the sum of mass numbers of complementary fission fragments plus the actual (integral) number of neutrons emitted, for a given pair, must be equal to the mass of the compound nucleus:

$$A_1 + A_2 + \nu = 236 \qquad \text{(I-5)}$$

Also, the sum of the nuclear charges of the complementary fission fragments must be equal to the nuclear charge of the fissioning nucleus:

$$Z_1 + Z_2 = 92 \qquad \text{(I-6)}$$

However, the above equations are not intended to define ${}^{A_1}_{Z_1}X_1$ and ${}^{A_2}_{Z_2}X_2$ uniquely because as stated before the number of neutrons ν emitted vary for every fission event. The equations merely identify complementary fragments with average mass numbers A_1 and A_2.

When heavy elements are bombarded by high energy particles, competition between fission and particle-evaporation becomes increasingly important. Processes like fragmentation and secondary reactions are also observed. A typical chain of fission-particle-evaporation competition can be given as follows:[32]

$$\begin{array}{ccccccc} {}^{A}X(E) & \xrightarrow[\text{Emission}]{\text{Particle}} & {}^{A'}X'(E') & \xrightarrow[\text{Emission}]{\text{Particle}} & {}^{A''}X''(E'') & \longrightarrow & (1\text{-}7) \\ \downarrow & & \downarrow & & \downarrow & & \\ \text{Fission} & & \text{Fission} & & \text{Fission} & & \end{array}$$

In the above scheme, a nucleus of mass A with an excitation energy E evaporates particles to form successively nuclei of masses A', A'', etc., and energies E', E'', ---- with fission as an alternative to each particle evaporation step. Fission may take priority over particle emission or vice-versa, depending upon the energetics of the system. Evaporated particles are generally neutrons rather than charged-particles because the latter require an additional energy to overcome the Coulomb barrier. So competition between fission and neutron evaporation is usually considered at each step. The Monte Carlo technique, with some modifications to include the possibility of fission at each step, is used to calculate the formation cross-sections of reaction products.

Several workers[33-36] have studied the reactions of

fission-evaporation competition. Pate[37] has performed the systematic calculations by combining nuclear cascade and nuclear evaporation processes to compute the average neutron-to-proton ratios of fission products from thorium bombarded by 8 MeV and 87 MeV protons[38], and uranium bombarded by 480 MeV protons.[39]

(b) Fission Probability:

The probability of fission seems to be related to nuclear charge (Z) and mass number (A) of the fissioning nucleus. In order to distinguish between fissile and non-fissile nuclides, a parameter, x , called the 'fissionability parameter' is obtained by considering Coulomb and surface energies of the spherical nucleus.[40] The Coulomb energy is proportional to $(Ze)^2/R$, where R is the radius of the nucleus, and the surface energy is proportional to $4\pi R^2$. Thus the parameter x is proportional to Z^2/R^3, and hence the term Z^2/A enables one to estimate the fissionability of a nuclide. Those nuclei with a value of Z^2/A greater than about 45 are unstable towards fission.

However, measurements made for photo-fission and neutron fission cross-sections indicated that the fission thresholds do not depend upon the value of Z^2/A alone. Similar conclusions were drawn from the studies of half-lives of spontaneous fission of even-even nuclides. Seaborg[41] has developed an empirical relation to calculate the slow-neutron fission threshold, E_b, as given by the following equation:

$$E_b = (19.0 - 0.36 \frac{Z^2}{A} + \epsilon) \text{ MeV} \qquad \text{(I-8)}$$

where ϵ = 0 for even-even,

ϵ = 0.4 for even-odd, and

ϵ = 0.7 for odd-odd nuclides.

Since a measurable amount of neutron-induced fission occurs at an excitation energy less than the fission threshold E_b, it was further proposed that the activation energy, E_a, is about 0.9 MeV less than E_b. The values of E_b, and hence E_a, can be calculated and also the neutron binding energy, B_n, for a nuclide with mass number A + 1 can be obtained. If the difference between $B_n - E_a$ is positive, then the fission cross-sections will be greater than about one barn. If the difference $(B_n - E_a)$ is negative, then the fission cross-sections will be less than about one barn. However, even though the correlation between calculated and observed values for slow-neutron fission is good, this line of demarcation of fissile and non-fissile nuclides is quite arbitrary.

In fission induced by particles with high energies, where the competition between fission and neutron evaporation has to be considered and the probability of neutron emission is comparable to that of fission, the relative probability for neutron emission or fission is expressed in terms of the partial 'width' ratio Γ_n/Γ_f. This ratio, though subject to a mass number dependence, decreases as the nuclear charge increases. There is no marked dependence of the above ratio on excitation energy.

I-B. FISSION STUDIES

(1) Mass Distribution

The distribution of mass in fission has been determined by two types of measurements: (a) physical measurements, where the kinetic energy distribution of fission fragments is determined, and (b) chemical measurements for which there are two methods available, (i) radiochemical, (ii) mass spectrometric. In the radiochemical method, the cumulative yields of radioactive nuclides near the end of the mass chain are measured. With the mass spectrometric technique, the yields of stable and long-lived members at the end of the mass chain are determined.[42]

(a) Physical Measurements:

Kinetic energy distribution of fission fragments is determined either by measuring the ionization produced by fragments in an ionization chamber or by measuring the velocity distribution of the fragments by the time-of-flight method. Both techniques are outlined below.

(i) Ionization Measurements:

Two back-to-back ionization chambers, having a common cathode made of a very thin foil, are used for the simultaneous measurements of the ionization produced by a pair of fission fragments each travelling in an opposite direction. If the fissioning nucleus is considered initially at rest, then the law of conservation of momentum, neglecting emitted neutrons, gives

$$M_L V_L = M_H V_H \qquad (I\text{-}9)$$

where M = mass of fission fragment,

V = velocity of fission fragment, and

L and H refer to light and heavy fragments respectively.

Also, it can be easily derived from equation (I-9) that

$$\frac{E_L}{E_H} = \frac{\frac{1}{2}M_L V_L^2}{\frac{1}{2}M_H V_H^2} = \frac{M_H}{M_L} \qquad (I\text{-}10)$$

where E = kinetic energy of the fission fragment.

Equation (I-10) shows that the masses are inversely proportional to kinetic energies; hence, from the measurements of kinetic energy distribution of fission fragments, the mass distribution can be determined.

(ii) Velocity Measurements:

The distribution of the velocity of fission fragments is measured directly by irradiating a target film deposited on a thin foil. Measurements are made by the time-of-flight method. The fission fragments are detected by scintillation detectors. One fragment travels only about a centimeter before striking a detector, while the other fragment travels about 350 centimeters along an evacuated tube. The pulses are projected on a cathode ray tube and photographed. The distance between the two peaks gives the velocity which is then converted into the kinetic energy of the fission fragments.

The energy distribution of the fission products formed in thermal neutron induced fission of ^{233}U, ^{235}U, and ^{239}Pu[43,44] and in fast neutron fission of ^{235}U, ^{238}U, ^{232}Th, and ^{239}Pu[45,46] have been measured.

Leachman[47], and Milton and Fraser[48] have measured the velocities of fission fragments produced in thermal neutron fission of ^{233}U, ^{235}U, and ^{239}Pu.

Britt and Whetstone[49] studied the fission of ^{230}Th, ^{232}Th, and ^{233}U induced by alpha particles of various energies and determined the mass and total kinetic energy distributions of the fragments. They also reported the average number of prompt neutrons emitted as a function of the fragment mass.

Whetstone[50] measured the velocities of the coincident fission fragments emitted in fission of ^{230}Th, ^{232}Th, and ^{233}U induced by alpha particles of various energies, and in fission of ^{230}Th induced by 12 MeV and 14 MeV deuterons. In each case, he found that there was a decrease in the average total kinetic energy of the fragments for symmetric mass division. He also determined the dependence of prompt neutron emission upon fragment mass by comparing the primary mass yields he obtained with those measured by radiochemical methods.

Milton and Fraser[51] have reported the energies, angular distribution, and yields of the prompt neutrons from individual fragments in the thermal neutron fission of ^{233}U and ^{235}U by velocity measurements.

(b) Chemical Measurements:

(i) Radiochemical Method:

This method involves the separation of the fission product of interest in a radiochemically pure form, free from contaminating activities. Since the amount of a nuclide formed in fission is small, a known amount of the element to be separated is added in inactive form as a carrier. In order to ensure complete exchange between the inactive carrier and the active isotope, the two must at some time be in the same or readily exchangeable valence state.

The element of interest is isolated by specific precipitations, solvent extraction, ion-exchange separation, etc. 'Hold-back' carriers and scavengers are used to remove the suspected contaminants. Finally, samples of the radioactive nuclide are measured with a radiation detection instrument to determine the number of active atoms present. The total number of atoms formed in fission is determined after applying necessary corrections, such as chemical yields, counter efficiencies, branching ratios, etc. The fission yields are then calculated by applying appropriate equations. (Details of these equations are given in Appendix A.) The yields are usually expressed as a 'cross-section', σ. This is defined as the probability that a particular type of nuclear reaction will occur at a certain bombarding energy for a given target and projectile. The cross-section values have the dimensions of an area and are given in the units of barn ($1b = 10^{-24}$ cm^2).

(ii) Mass Spectrometric Method:

This is a very sensitive method with good precision ($\pm$ 1%) to determine relative or absolute fission product yields. It is possible to determine the yields of stable and long-lived isotopes that grow from active fission products and that may be formed directly in fission. Fission yields for several mass chains can be determined at the same time for a mixture of fission products from a single irradiation.

(iia) Relative Fission Yields:

To determine relative fission yields, a mass spectrogram for a certain element is compared with a standard of known isotopic abundances of the same element. The relative cumulative fission yields of the fission products having an end-product element, as that of the standard, are then determined simply by comparing the mass spectrogram for the fission end-product with that for the standard. The mass numbers of the fission products are determined from the respective positions of the mass peaks in the end-product spectrogram, and the mass peak height ratios of standard to fission product give the relative fission yields. Absolute yields are calculated either by (a) normalizing the measured relative yields together with yields determined radiochemically to 100% for either the light mass region or the heavy mass region, or (b) by normalizing through a particular, precisely-known fission product yield.

(iib) Absolute Fission Yields:

The absolute number of atoms of each nuclide in a mixture of fission products can be determined by the method of isotope dilution. A known amount of an isotope, or of the naturally occurring element itself, is added to the sample to be analysed. The element is separated chemically or by the mass spectrometer, and the resultant change in isotopic abundances of the element in question in the mixed sample is determined mass spectrometrically. The concentration of the nuclide of interest in the sample is then calculated from the change in isotopic abundances and the known amount of the tracer added. A quantitative recovery of the tracer-sample mixture is not necessary because the analysis depends only upon the ratio of the isotopes in the mixture.

Absolute fission yields are determined by measuring the total number of fissions, in addition to the absolute number of atoms of a nuclide produced in fission. For neutron bombardments, the total number of fissions in an irradiated sample is generally determined by the use of flux monitors such as BF_3, Co, or Sm.

The mass distribution curves are constructed by plotting the percentage yields of the various fission products against the respective mass numbers. A comparison of the three distribution curves determined[52] in thermal neutron fission of ^{233}U, ^{235}U, and ^{239}Pu is shown in Fig. 1. The general behaviour is similar. The curves are approximately

FIGURE 1

MASS DISTRIBUTION IN THERMAL NEUTRON FISSION

FROM KATCOFF[52]

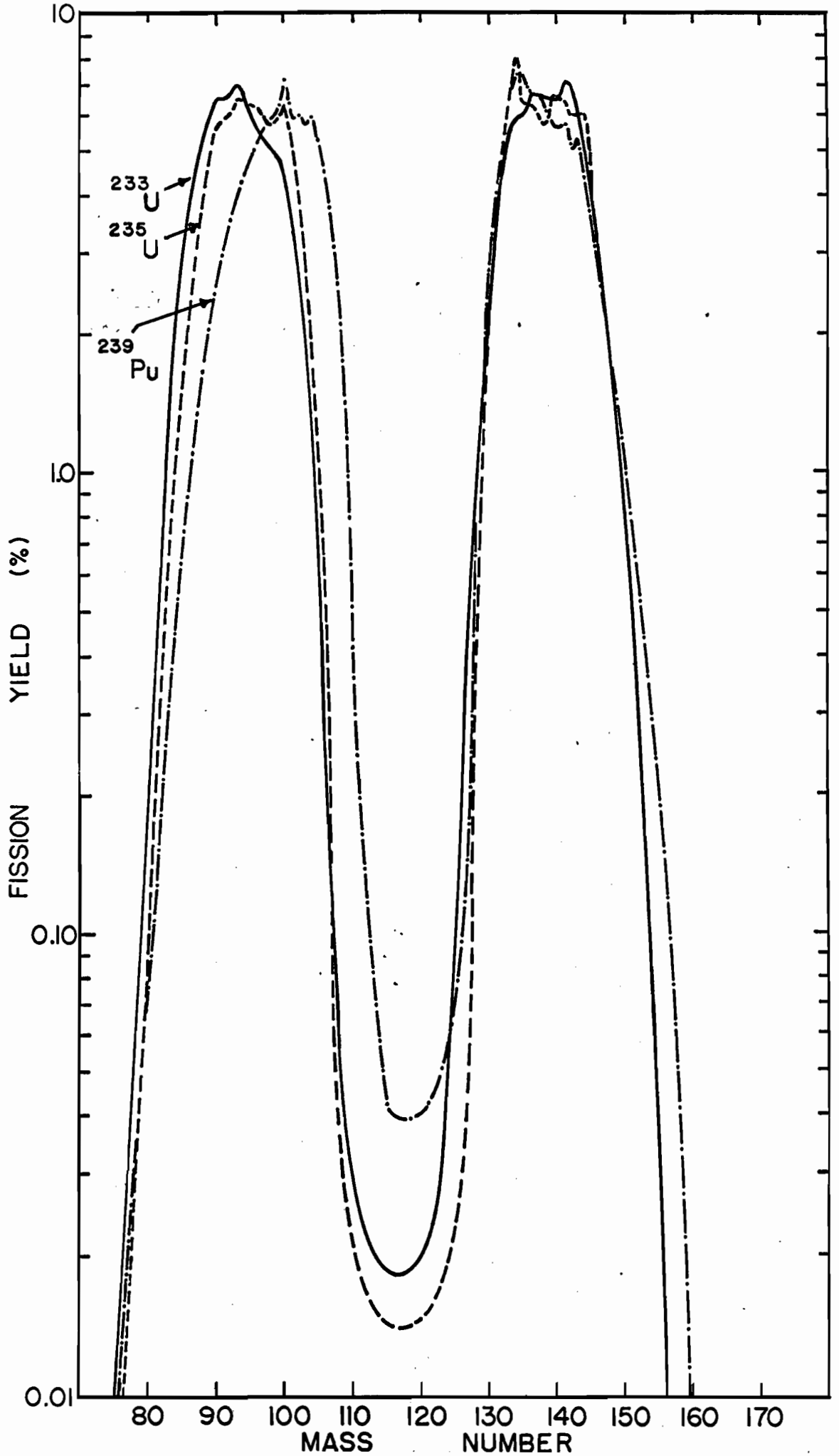
10
1.0
0.10
0.01
FISSION YIELD (%)
233 U
235 U
239 Pu
80
90
100
110
120
130
140
150
160
170
MASS NUMBER

symmetric in nature but the mode of fission is asymmetrical as exhibited by the occurrence of two, light and heavy, mass peaks. The nuclides which lie at the bottom of the valley typify symmetric fission and those which lie on the peaks typify asymmetric fission. The maxima of the heavy mass peaks seem stationary near about mass number 137, and those of the light mass peaks vary approximately between mass numbers 94 to 99 in going from ^{233}U to ^{239}Pu. The mass distribution extends almost from mass number 70 to mass number 160, and the full width at half maximum for each peak is about 15 mass numbers. Spikes occur near the top of each peak. This 'fine structure' has been attributed to shell effects, but no real explanation consistent with all the experimental facts has yet been offered.

The asymmetric fission mode seems to be persistent also in fission of heavy elements induced by charged particles of low energies. However, with increasing projectile energy, the symmetric fission mode becomes more probable.

Stevenson et al.[53] from their work together with data of others[54-56] have reported the fission product distribution of ^{238}U at various proton energies. These curves are shown in Fig. 2. It can be seen that, with increasing projectile energy, the distribution becomes broad and the two humps slowly disappear forming a single-peaked curve. The greatest change is the increase in the probability of symmetric fission with increasing projectile energy. The distribution extends approximately from mass number 79 to mass number 159 at

FIGURE 2

FISSION-PRODUCT DISTRIBUTIONS OF ^{238}U BOMBARDED WITH PROTONS OF VARIOUS ENERGIES[53]

● - Stevenson et al.[53]

■ - Hicks et al.[55], and Hicks and Gilbert[56]

▲ - Lindner and Osborne[54]

X - Reflection points

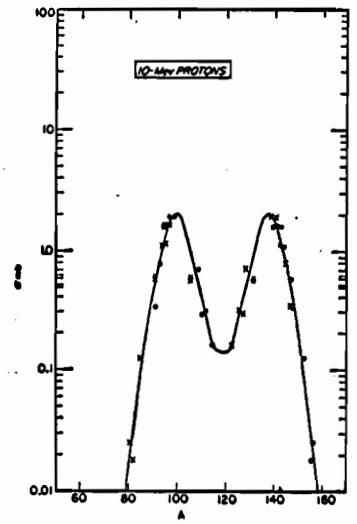
10-Mev PROTONS
A

(a)

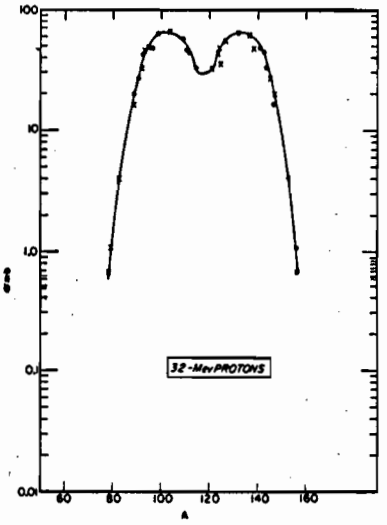
32-Mev PROTONS
A

(b)

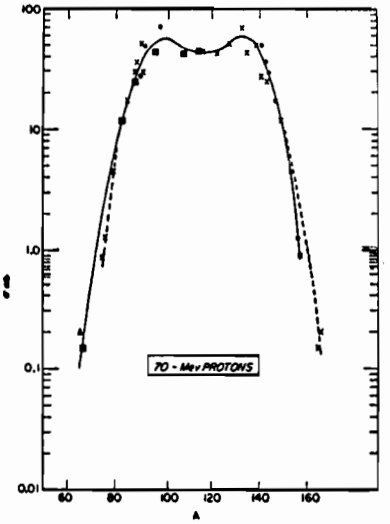
70 - Mev PROTONS
A

(c)

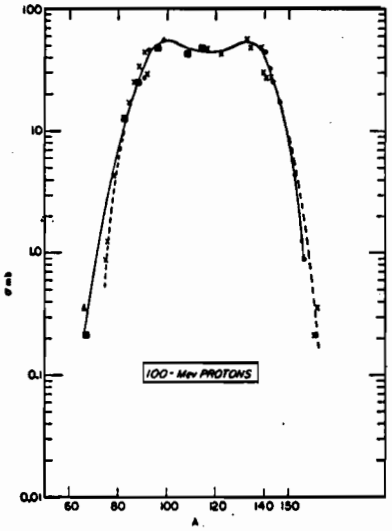
100 - Mev PROTONS
A

(d)

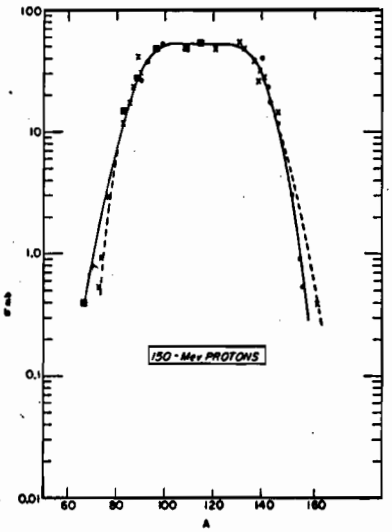
150 - Mev PROTONS
A

(e)

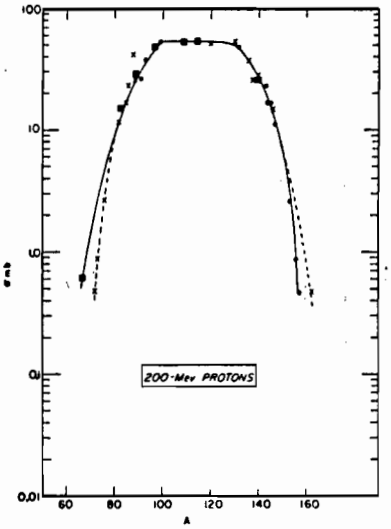
200-Mev PROTONS
A

(f)

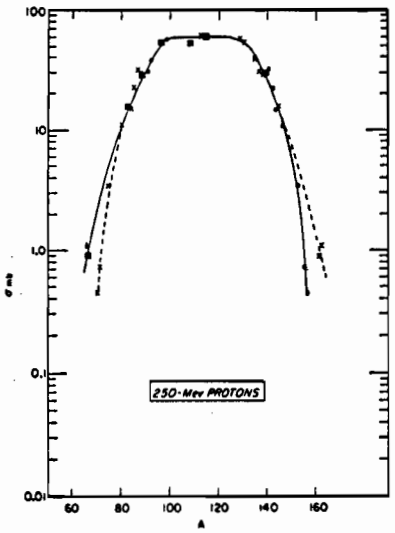
250-Mev PROTONS
A

(g)

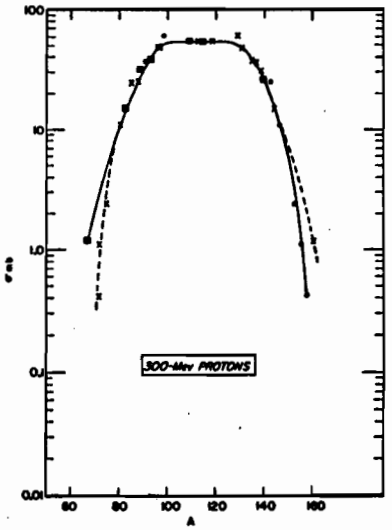
300-Mev PROTONS
A

(h)

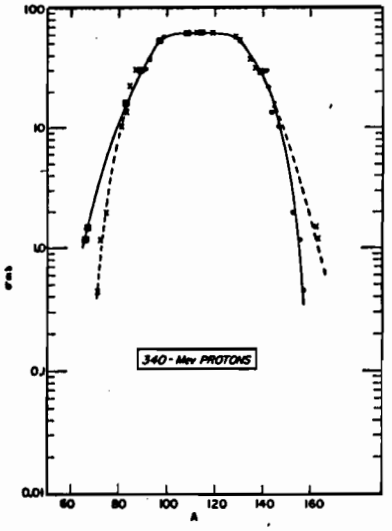
340 - Mev PROTONS
A

(i)

10 MeV and from mass number 55 to mass number 160 at 340 MeV, showing that the probability of formation of fission products with low mass number increases with increasing projectile energy.

(2) Charge Distribution

Measurements of nuclear charge distribution in fission have furnished important information about the nature of the fission process. A distinction should be made between charge dispersion and charge distribution, though these two terms are frequently used interchangeably. Charge dispersion implies the independent fission yield distribution among the isobars at a given mass number, and charge distribution is better explained as the manner in which the nuclear charge divides itself between the two fragments in the fission act[57]. In order to obtain the charge distribution from charge dispersion data, it is essential to know the atomic number of the fissioning nucleus.

(a) Postulates:

Three charge distribution postulates have been proposed by various workers to describe the distribution of nuclear charge in fission. They are as follows:

(i) Minimum Potential Energy (M.P.E.):

This postulate was suggested by Way and Wigner[58] and was formulated theoretically by Present.[59] It states that the most probable charge distribution in fission is that

in which the two fragments have a minimum potential energy. This hypothesis predicts smaller chain length in the light than in the heavy mass region.

(ii) Unchanged Charge Distribution (U.C.D.):

Sugarman and Turkevich[60] put forward this hypothesis and it was first used successfully by Goeckermann and Perlman[61] to account for the results of their study of 190 MeV deuteron-induced fission of bismuth. According to this hypothesis the fission products will have the same charge-to-mass ratio as the fissioning nucleus. It can be represented by the following equation:

$$\frac{Z_p(A)}{A} = \frac{Z_c}{A_c - \bar{\nu}} \qquad \text{(I-11)}$$

where A = mass number of a particular mass chain under investigation.

$Z_p(A)$ = the most probable charge of mass chain A.

A_c and Z_c = mass number and atomic number of the compound nucleus respectively.

$\bar{\nu}$ = the average number of prompt neutrons evaporated from the compound nucleus as fission takes place.

This hypothesis predicts larger chain length in the light than in the heavy mass region.

(iii) Equal Charge Displacement (E.C.D.):

This hypothesis was first proposed by Glendenin et al.[62] and later modified by Pappas[63]. It states that when

fission occurs, the most probable charge, Z_p (not necessarily integral), for the light and heavy fragments will be equally displaced from stability. This can be given by the following equation:

$$(Z_A - Z_p)_L = (Z_A - Z_p)_H \qquad \text{(I-12)}$$

where Z_A and Z_p are the most stable charge and the most probable charge respectively for a given mass chain A. L and H designate light and heavy fragments respectively.

Coryell et al.[64] have given a prescription for the inter-comparison of data of the most probable charge for a given mass chain A, $Z_p(A)$, from various types of fission differing in the compound nucleus formed and in excitation energy. This prescription is formulated with the assumption that the shape of the charge distribution curve is the same for all fissioning nuclei as that along any isobaric chain for thermal neutron fission of ^{235}U, only its position varies with the compound nucleus and the excitation energy.

(b) Measurements:

Nuclear charge distribution can be determined by physical and radiochemical methods. There are two physical methods available for determining the average charge of primary products as a function of mass number.[65] One method uses a gas-filled mass spectrometer to separate the fission products, and the rate of beta-disintegration per fission is determined for each interval of mass.[66] In another method, the

simultaneous measurements of masses and characteristic K X-ray energies associated with the primary fission fragments are made.[67,68] The masses of the fragments are established from their kinetic energy measurements, and the X-ray energies give the atomic numbers.

The radiochemical techniques described under mass distribution (P.16) are also used to determine independent yields in charge distribution. The measurements of the independent yields of the primary products resulting from the splitting of the fissile nuclei are severely limited due to the very short half-lives of the fission products which are far away from the beta-stability line. Hence, studies have been confined to the shielded and semi-shielded nuclei and those that can be chemically separated in a time comparable to the half-life of their parent. In the latter case, since both members of a parent-daughter pair are produced independently, corrections for growth of daughter from parent during and after an irradition must be made. This can be accomplished either (1) from two separate irradiations with appropriately chosen periods of irradiation and fixed time intervals between the chemical separation of the daughter and the end of the bombardment, or (2) from a single irradiation followed by two successive separations of the daughter product. In the former case, the daughter activity from each irradiation will lead to an equation of the form of equation B-15 (derived in Appendix B) and these equations are then solved simultaneously for the

cumulative formation cross-section of the parent nuclide and the independent formation cross-section of the daughter nuclide. In the case of a single irradiation, the cumulative formation cross-section of the parent nuclide is calculated in standard fashion from the daughter activity obtained in the second extraction. The independent formation cross-section of the daughter nuclide is then calculated by means of equation B-15 (given in Appendix B) from the daughter activity obtained in the first extraction.

The following is a brief survey of some of the major works in the field. Glendenin et al.[62] were the first to consider nuclear charge distribution in thermal neutron fission of ^{235}U and came up with the Equal Charge Displacement postulate. Pappas[63] studied the fission yields in the shell perturbation region and modified the E.C.D. postulate to account for shell effects.

Wahl[69] investigated the fission of ^{235}U bombarded by 14 MeV neutrons and obtained the fractional chain yields of several iodine and tellurium isotopes. The results were correlated with the E.C.D. postulate.

Hicks and Gilbert[56] have studied ^{238}U fission induced by 70 MeV to 340 MeV protons, 19 MeV to 190 MeV deuterons, and 50 MeV to 380 MeV alpha particles. They obtained the yield data for several fission products and correlated their results with the U.C.D. postulate.

Kennett and Thode[70] mass spectrometrically determined the independent yields of iodine isotopes produced

in fission of ^{233}U, ^{235}U, and ^{239}Pu by thermal neutrons, and bromine isotopes produced in thermal neutron fission of ^{233}U and ^{235}U, and in fast neutron fission of ^{239}Pu. They found their data could not be fitted according to the E.C.D. hypothesis. Hence, they postulated that the fission act occurs in such a manner as to maximize the energy release in fission. They also suggested on the basis of their iodine data that, in the mass region below mass number 130, the most probable charge, Z_p, stays close to and just above 50. Alexander and Coryell[71] found that the calculations of the most probable charge based on the postulate of Maximum Energy Release, applying to all mass regions, gave worse scatter of data than the original E.C.D. postulate.

Gibson[72] studied the action of 20 MeV deuterons on ^{239}Pu, 23 MeV deuterons on ^{233}U, 31 MeV deuterons on ^{237}Np, and 46 MeV alpha particles on ^{237}Np. He found that the observed charge distributions lie between the E.C.D. and the U.C.D. hypotheses.

Lavrukhina and Krasavina[39] investigated the fission of ^{238}U, ^{232}Th, and ^{209}Bi induced by 480 MeV protons. They obtained charge distribution curves which were asymmetric in nature with the yields falling steeply on the neutron-excess side.

Porile and Sugarman[73] studied the 450-MeV proton-induced fission of bismuth and tantalum. They found that the results could be explained in terms of the E.C.D. for bismuth and the U.C.D. for tantalum.

Wahl[74] has reported the independent yields of krypton and xenon isotopes with very short half-lives from thermal neutron fission of ^{235}U, using the emanating power of stearates. He constructed an empirical curve of the most probable primary charge, Z_p, vs. mass number. The results were in correlation with the E.C.D. postulate.

Pate et al.[38] bombarded ^{232}Th with 8 MeV to 80 MeV protons and measured the independent and the cumulative yields of various iodine and tellurium isotopes. They constructed charge distribution curves at different proton energies and found that, as the bombarding energy is increased, the curves become broader and the most probable charge, Z_p, moves closer to the beta stability line. Pate[37] performed calculations based on the prompt nuclear cascade and nuclear evaporation processes and found that the data were not inconsistent with the E.C.D. hypothesis.

Chu[75] obtained fission yield data by mass-spectrometric studies. He bombarded ^{238}U and ^{235}U with alpha particles of various energies, ^{238}U with 730 MeV protons and 100 MeV carbon ions. His results fitted an intermediate recipe between E.C.D. and U.C.D. Moreover, he found ffom the charge distribution curve constructed from proton data that, although the curve was asymmetric, the yields were falling steeply on the neutron-deficient side, which is quite opposite to the observations made by Lavrukhina and Krasavina.[39]

Friedlander and Yaffe[76] measured the formation cross-sections of several isotopes in the mass range $38 \leq A \leq 48$

produced in the bombardment of Pb and U with 3.0 BeV protons. They found that the maximum of the isobaric yield distribution for the nuclides from lead bombardment occurs at the stability line, while that from uranium is somewhat on the neutron-excess side. The data were shown to be consistent with a cascade-fission-evaporation mechanism.

Rüdstam and Pappas[77] found in 170 MeV proton-induced fission of uranium that the results lie half-way between the U.C.D. and E.C.D. postulates.

Colby and Cobble[78] obtained the primary yields of various fission products formed in fission of uranium isotopes induced by 20 MeV to 40 MeV alpha particles and correlated the data with the U.C.D. hypothesis. They also noted that the data for nuclides away from the closed neutron shell gave a smooth correlation and that data for nuclides of 83 neutrons also showed a smooth correlation but narrower distribution curve.

Kjelberg et al.[79] measured the fractional chain yields of several fission products formed in 13 MeV to 82 MeV proton-induced fission of ^{232}Th and found their results agreed qualitatively with the data of Pate et al.[38]

Wahl et al.[80] have collected data on independent and cumulative yields of a number of fission products in thermal neutron fission of ^{233}U, ^{235}U, and ^{239}Pu, and spontaneous fission of ^{252}Cf, which were very useful for an analysis of the E.C.D. hypothesis. By an empirical approach, they constructed a charge distribution curve from their data of

six different mass chains and showed that the curve could be described with the help of two parameters, the most probable charge Z_p for a particular mass chain A, $Z_p(A)$, and the constant C, which defines the full-width at half maximum of the distribution, and this is assumed to have a Gaussian shape.

$$p(Z) = (C\pi)^{-\frac{1}{2}} \exp[-(Z - Z_p)^2/C] \qquad (I\text{-}13)$$

where $p(Z)$ is the fractional independent yield of the fission product with atomic number Z. They used the value of constant $C = 0.9$, the best fitting value for their experimental data.

It was assumed that this charge distribution curve would be applicable to other chains for which the fractional yield of only a single member was known. The most probable charge values interpolated from the curve were plotted against the respective mass number and a smooth, continuous curve was drawn to fit the values as well as possible. The comparison of their charge distribution curve with those obtained by other workers[62,63] is shown in Fig. 3. It can be seen that the general behaviour of the curves is similar but the one determined by Wahl et al. is narrower and rises to a higher maximum than the other two.

The results of the studies, as reviewed above, have been used mostly to substantiate the postulates of the U.C.D., the E.C.D., or the intermediate path between the two. In applying these postulates, nuclear charge distribution is usually determined by the variation of the fractional chain yields of a given mass chain as a function of $Z - Z_p$ or $Z - Z_A$,

FIGURE 3

NUCLEAR CHARGE DISTRIBUTION

———— - Glendenin et al.[62]

• - Pappas[63]

- - - - - Wahl et al.[80]

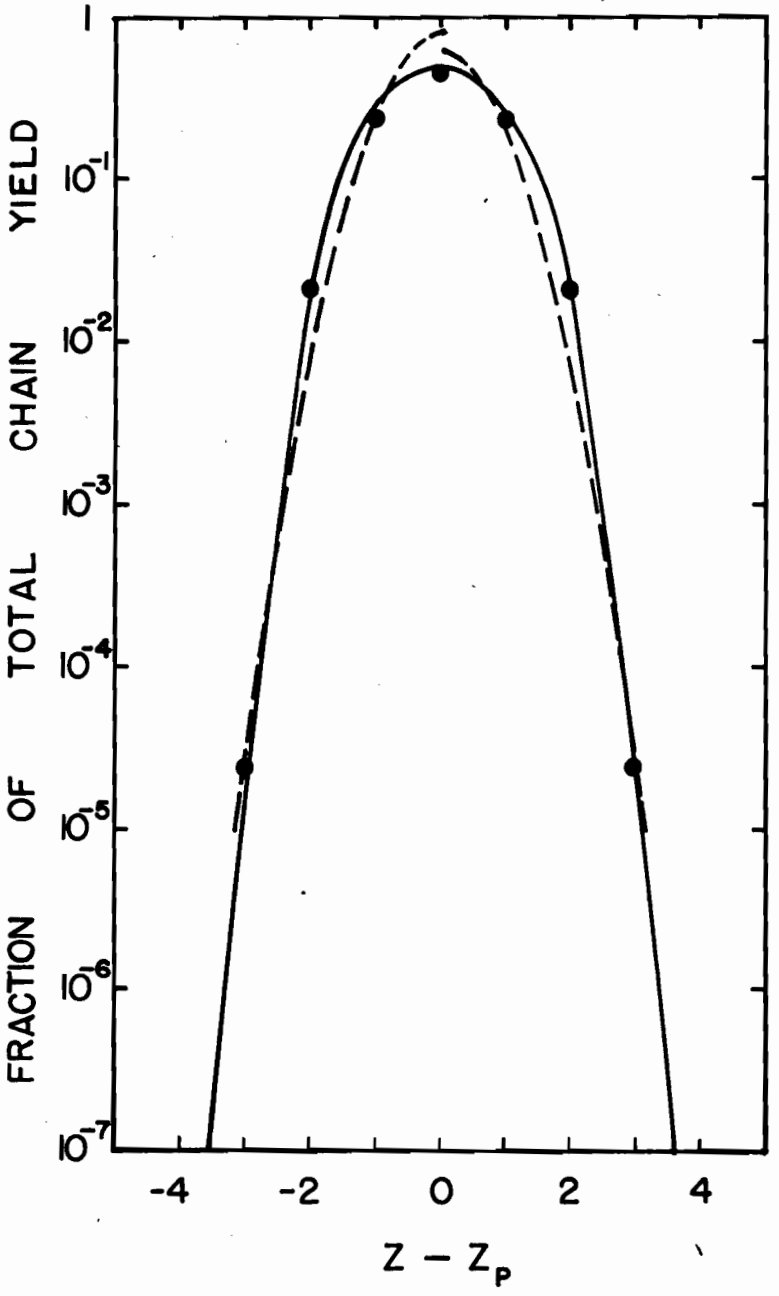
FRACTION OF TOTAL CHAIN YIELD
1
10^{-1}
10^{-2}
10^{-3}
10^{-4}
10^{-5}
10^{-6}
10^{-7}
-4
-2
0
2
4
$Z - Z_P$

where Z is the atomic number of the fission product nuclide under investigation, and Z_A and Z_p are the most stable charge and the most probable charge respectively of a mass chain A. However, various workers have proposed that the discontinuities in Z_A and Z_p at nuclear shell edges be taken into account[63,70,84]. Friedlander et al.[82] have shown that the neutron-to-proton ratio, N/Z, of the product nuclide is a more useful parameter in determining nuclear charge distribution since it avoids the difficulties inherent in determining Z_A and Z_p.

Kaufman[83] has also found that the ratio of neutrons-to-protons in the nucleus gives a smoother curve than $Z - Z_A$ as abscissa. He obtained charge distribution curves by measuring the formation cross-sections of a number of nuclides in the mass range $65 \leqslant A \leqslant 74$ in the bombardment of In, Au, and U with 2.9 GeV protons. The curves were found asymmetric about the peak, with uranium having the most asymmetry and the yields falling more steeply on the neutron-deficient side. The peak position was found to shift towards a larger neutron-to-proton ratio as the target mass was increased.

Friedlander et al.[82] have studied extensively the fission of natural uranium by protons ranging in energy from 0.1 GeV to 6.2 GeV. They reported cross-sections for the independent formation of cesium isotopes in the mass range $127 \leqslant A \leqslant 136$, $^{84,86}Rb$ and ^{131}Ba. They constructed charge dispersion curves at various proton energies by plotting the independent yield of a product against the neutron-to-proton

ratio of that particular fission product. They found that the curves broaden with increasing energy and that the peak position moves closer to the beta stability line. They also constructed an empirical curve relating the energy at which the excitation functions reach their maxima to the ratio of neutrons-to-protons of the fission product. It was found that the maxima of the excitation functions move to higher energies with decreasing neutron-to-proton ratio. The results were semi-quantitatively accounted for by assuming fission with the U.C.D. followed by nucleon evaporation.

The work of Davies and Yaffe[84] extended the empirical curve of Friedlander et al.[82] by another decade of energy to include cesium isotopes in the mass region $130 \leqslant A \leqslant 138$ produced in the fission of natural uranium by 20 MeV to 85 MeV protons. They constructed charge dispersion curves from the data at different proton energies, using the neutron-to-proton ratio of the fission product as abscissa. The general features of the curves were similar to those observed by other workers.[38,82]

Wahl and Nethaway[85] obtained the independent yield of ^{121}Sn to study the nuclear charge distribution in symmetric fission of ^{235}U induced by thermal neutrons. The small independent yield of ^{121}Sn led them to conclude that the most probable charge, Z_p, for fission products with mass number $A = 121$ must be less than 50. Troutner et al.[86] determined an independent yield of ^{127}Sb produced in thermal neutron fission of ^{235}U. They found that the calculated value of the

most probable charge was 49.5 for mass chain 127. Hence they concluded that there is no pronounced effect of the 50-proton-shell on the Z_p function.

Benjamin et al.[87] investigated 20-80 MeV proton-induced fission of ^{232}Th by measuring several cesium isotopes and constructed charge dispersion curves at various proton energies. The results were correlated with the intermediate recipe between the U.C.D. and the E.C.D. postulates.

I-C. FISSION THEORIES

The complexity of the fission process is evident from the lack of a unique theory which can explain all of its various characteristics. Several theories have been proposed, each having its own merits and demerits. Outlines of the principal concepts are given below.

(1) Liquid Drop Theory

Bohr and Wheeler[88] related the compound nucleus to a spherical drop of fluid, a liquid drop, made up of incompressible, densely packed nuclear matter in which the nucleons of the nucleus are held together by the strong, short-range nuclear forces analogous to the surface tension forces in a liquid drop. The liquid drop will break up if deformation is caused by external disturbances. By similar analogy, the excitation energy supplied from external sources tends to set up oscillations within the compound nucleus. As a result it gets distorted, but the surface tension forces will tend to restore the distorted compound nucleus to its original shape.

However, the effect of surface tension forces decreases with the increase in distortion caused by the excitation energy. Eventually the compound nucleus gets sufficiently distorted and reaches a critical deformation, the point from which it cannot regain its original spherical shape. Then the Coulomb repulsive forces divide it into two or more fragments and a large amount of energy is set free. A semi-empirical mass equation was formulated[88,89] to calculate the energy released and hence the relative probability of neutron and proton distributions between the two fragments could be calculated. Calculations indicated that the maximum energy is released in symmetric fission.[88,89] It was also predicted that with the increase in projectile energy, thereby increasing the excitation energy of the compound nucleus, the more probable mode of fission will be asymmetric. However, experimentally the opposite is well established except at very high energies.

(2) Shell or Independent-Particle Theory

M. Mayer[90] from her investigations concluded that nuclei containing certain combinations of neutrons and protons have exceptional stability. These combinations are called 'magic' numbers and they are 2, 8, 20, 50, 82, or 126 for neutrons and similarly for protons. The nucleus is considered as having distinct nuclear shells and, when a shell contains a magic number of nucleons, it is considered as a 'closed shell'. The neutron and the proton shells are thought to be independent of each other. Each nucleon moves in its own closed orbit

within the nucleus, analogous to the electron movement in outer atomic orbits. Each particle is considered as an independent particle, and the interaction between particles is a small perturbation on the interaction between a particle and the potential field. The potential due to nuclear attractions has a form between the square-well potential ($V = -V_o$) and the oscillator potential ($V = -V_o + ar^2$, where a is a constant and r is the distance between the particle and the centre of force). The nuclear shells, just like atomic shells, are also governed by the Pauli exclusion principle which prohibits two protons from occupying the same quantum state and two neutrons from having the same quantum numbers. The effects of 'strong spin-orbit coupling' (the energy difference of a particle according to whether its spin angular momentum is parallel or anti-parallel to its orbital angular momentum) should also be considered.[91,92]

This theory is quite successful in explaining several phenomena, particularly for low-lying excited states of nuclei.

(3) Modern Approach

Many proposals were made to account for asymmetry in fission. Swiatecki[93] suggested that asymmetry may be connected with nuclear polarization and compressibility which will affect the symmetric saddle point and so the final division will be asymmetric. Maris[94] considered the effect of non-uniform charge distribution in the nucleus to explain the observed asymmetry. Fong[95] studied the effect of fission

fragment deformations during the fission act and also possible Coulomb barrier effects. He suggested that the asymmetric fission mode is associated with the emission of a large number of prompt neutrons, and again, the heavy fragment emits more neutrons than the light one. He gave a mathematical formulation to calculate the relative fission probabilities and found that the calculated mass distribution of ^{235}U induced by thermal neutrons agreed with the experimental curve. In further development of the theory, Whetstone[96] reported that the average number of prompt neutrons emitted, $\bar{\nu}$, is nearly the same for various modes of mass division and $\bar{\nu}_L \cong \bar{\nu}_H$ for light and heavy fragments. Fong[97] introduced this into his theory. He suggested that the existence of some constraint in the process of approaching equilibrium controls the partition of the excitation energy between the two fragments. With this assumption, Fong calculated the mass yield curves of spontaneous fission of ^{252}Cf and thermal neutron fission of ^{235}U. He found the calculated curves in agreement with the observed curves.

Leachman[98] adopted an empirical approach and summarized the observed fission data into the following six principal characteristics.

(i) Asymmetric mode of fission is prominent in low energy induced fission of heavy elements. The heavy mass peak of the mass-yield curve remains almost stationary and the light mass peak shifts towards low mass numbers with increasing excitation energy.

(ii) Fragment excitation increases above closed shells. This is observed in the valley of the mass-yield curve, where symmetric fission is predominant.

(iii) For symmetric fission, the repulsive kinetic energy of the fragments decreases which compensates for (ii) above.

(iv) The nuclear charge distribution in the fission process results in the proton-rich products being in the lighter of the heavy fission fragment groups and proton-deficient products in the heavier of the heavy fission fragment groups. For the light fragment group, a similar complementary trend is observed.

(v) Coulomb energies of the fission fragments are dependent upon the nuclear size, which is determined from nuclear charge and mass.

(vi) The yields of the symmetric fission mode increase with increasing excitation energy and exceed the asymmetric fission yields.

From the above considerations, Leachman proposed that the light fragment will have a shell configuration of 50 neutrons and the heavy fragment a shell configuration of 50 protons. This shows a light fragment core at mass number 82 and a heavy fragment core at mass number 126. These two cores are joined by a thin neck consisting of about 28 nucleons, out of which about ten are protons and the remainder are neutrons.

Swiatecki and his collaborators[99-103] from their

work on the liquid drop theory have shown that the comprehensive fission theory may be emerging at least for nuclides having the fissionability parameter, x , less or equal to 0.67, i.e. below about radium. The fissionability parameter, x , is defined as $(Z^2/A)/(Z^2/A)_o$, where $(Z^2/A)_o = 50.13$ is the critical value at which a spherical nucleus is unstable against any deformation. However, it is understood that to have a complete treatment, it will be necessary to consider the effects of single particles (shell effects) in the final analysis. Also, it may be necessary to consider the influence of the density of states in the final fragments.[95]

Cohen and Swiatecki[99] from their work on the potential energy of a deformed uniformly-charged liquid drop obtained the shapes of the saddle point as a function of the fissionability parameter, x . The saddle point shape is the critical shape in the deformation process leading to fission beyond which it is impossible to return to the initial shape. They found that below $x \cong 0.67$ the shape of the saddle point is like that of two spheroids connected by a thin neck and that a little more deformation will result in scission. This shows that the fission event is decided at the saddle point. Nix and Swiatecki[102] further developed this concept and formulated a theory in which the fissioning nucleus is further idealized as two overlapping or separated spheroids. Calculations of the potential energy (the sum of the Coulomb and surface energies) showed that the overlapping of spheroids begins at about $x \cong 0.80$. Hence their theory is applicable for

fissioning nuclei below about radium, i.e. below $x \leqslant 0.67$.

Calculations were performed for the distributions in fragment mass and total translational kinetic energy for nuclei lighter than radium. The calculated results were in fair agreement with experimental values. Further, calculations of the dependence of the distributions upon nuclear temperature and dependence of the most probable kinetic energy upon the fissionability parameter were found to agree with experimental results.

I-D. PURPOSE OF PRESENT WORK

The present work is to determine by radiochemical methods the isobaric yield dispersion in the fission of natural uranium by protons of energies 20 MeV to 85 MeV.

Since Davies and Yaffe[84] extended an empirical curve of Friedlander et al.[82] by studying mainly cesium isotopes, it was thought fruitful to undertake the investigation of nuclides other than cesium which were expected to have the maxima of their excitation functions within the energy range 20 - 85 MeV. On the basis of their work[82,84], these nuclides should have neutron-to-proton ratios in the range of 1.45 to 1.52. Accordingly, isotopes of Ba, La, and Ce in the mass range $139 \leqslant A \leqslant 143$ were selected.

In addition, these nuclides would give information on nuclear charge dispersion when both neutron number and proton number are varying, in contrast to the studies of cesium isotopes[84] where only the neutron number is changing.

II. EXPERIMENTAL PROCEDURE

II-A. PREPARATION OF TARGETS

The target consisted of uranium foil of natural isotopic composition, ranging in thickness from 0.001 inch for the studies of mass numbers 139 and 141 to 0.003 inch for the studies of mass number 143. Before each irradiation the uranium foil was cleaned with dilute nitric acid to remove the thick outer oxide layer. It was then washed with distilled water and acetone, and dried before use. The superficial density of the uranium foil was determined after each acid treatment.

The monitor foils were copper and aluminum with superficial densities 10.53 mg/cm^2 and 5.29 mg/cm^2 respectively. The $^{65}Cu(p,pn)^{64}Cu$ reaction was used to monitor irradiations at 20 MeV to 50 MeV proton energy. From 60 MeV to 85 MeV, $^{27}Al(p,3pn)^{24}Na$ was the monitor reaction.

The cleaned target foil was sandwiched between two similar guard foils to compensate for any recoil losses during an irradiation. For the same reason the monitor foil was similarly sandwiched. One edge of the foil stack was fastened to a target holder by means of screws, as shown in Fig. 4. The protruding edges of the foils were carefully sheared with a pair of scissors to align both target and monitor foils. This was done to ensure equal exposure of incident protons to all foils. The edges were pressed close together so that they were flush with one another. The whole assembly was then

FIGURE 4

ASSEMBLY OF TARGET AND TARGET HOLDER

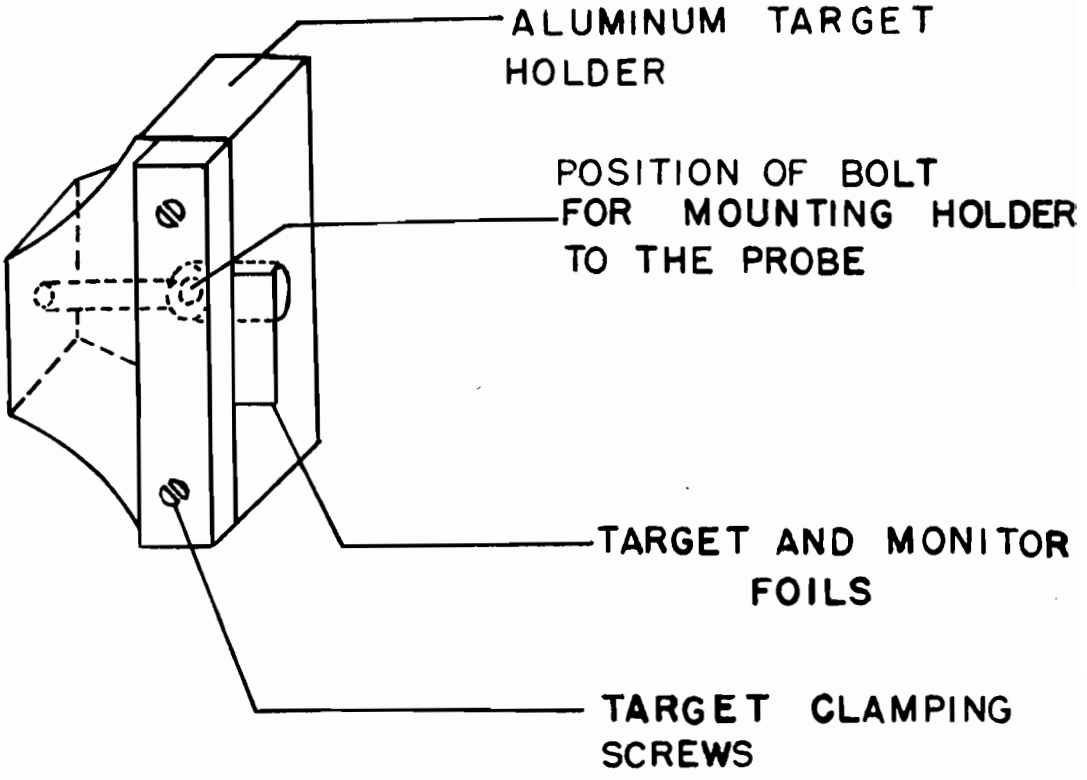
ALUMINUM TARGET HOLDER
POSITION OF BOLT FOR MOUNTING HOLDER TO THE PROBE
TARGET AND MONITOR FOILS
TARGET CLAMPING SCREWS

fixed to the end of the water-cooled probe of the cyclotron, which was set at a fixed radial distance corresponding to the desired projectile energy.

II-B. IRRADIATIONS

The internal proton beam of the McGill Synchro-cyclotron was used for all irradiations. The duration of an irradiation was determined by the half-lives of the nuclides under investigation and usually lasted from three minutes to thirteen minutes, except for ^{139}Ce studies. For this nuclide the duration of bombardment was one hour. The energy of the incident protons was obtained from an energy-radius relation with an uncertainty of $\pm$2 MeV, established by the McGill cyclotron group. Bombardments were carried out in the energy range 20 MeV to 80 MeV at 10 MeV intervals, and one more was taken at 85 MeV. All the targets were irradiated downstream from the monitor foils, that is to say, the incident proton beam would first strike the monitor foil and then the target foil. At the end of the irradiations, the foils were held together with a pair of tweezers and the first few millimeters from the free edge, where most of the activity would be expected, were cut off with a pair of scissors. The target and the monitor foils were separated from the guard foils and the target foil was dissolved immediately when a quick chemical separation was required. Otherwise the irradiated target was stored and treated later after a calculated period of time had elapsed. The monitor foils were treated at later convenience,

usually after 15 hours from the end of bombardment.

II-C. CHEMICAL SEPARATIONS

Chemical separations were performed to obtain the nuclide of interest in a pure radiochemical form free from contaminating activities. To do this, inactive carriers of the radioactive element in its natural isotopic form were added to the target solution before doing the specific separations. In addition, 'hold-back' carriers and scavengers for the suspected contaminants were added. The exchange between carrier atoms and active atoms resulted either from mixing or from performing a series of oxidation-reduction cycles.

Standard procedures for chemical separations were used throughout the study with minor modifications whenever necessary to give the most suitable form of a nuclide for activity measurements and chemical yield determinations.

(1) Barium

The procedure adopted for barium separation was based on that reported by Minkkinen[104] with a few modifications as desired. The barium carrier solution was standardized by volumetric[105] and gravimetric[104] methods.

The irradiated uranium target was dissolved in a small quantity of 12 N hydrochloric acid with a drop of concentrated nitric acid. Barium carrier solution (10 mg) and cesium hold-back carrier solution (10 mg) were added immediately, the combined volume being less than 5 ml. The

solution was cooled to about 5°C in an ice bath and barium chloride was precipitated by adding 20 ml of a cold mixture of hydrochloric acid and anhydrous ether (ratio of 4:1 by volume). The time at the end of this precipitation was taken as the separation time of barium from cesium. The precipitate was dissolved in water and barium chloride was re-precipitated by adding the cold hydrochloric acid-anhydrous ether mixture. Two such quick steps were performed. Further purification was achieved by scavenging with iron and lanthanum to remove rare-earth impurities. The lanthanum scavenging was done after about one hundred minutes from the end of irradiation to allow most of the barium-141 and barium-142 to decay to their lanthanum daughters. After the scavenging step, the supernate was neutralized with 6 M hydrochloric acid, and the resulting solution was buffered by adding 2.5 ml of 6 M acetic acid and 5 ml of 6 M ammonium acetate. This mixture was heated to boiling and 2 ml of 1.5 M sodium chromate solution was added dropwise to obtain barium chromate precipitate. The chromate was dissolved in 6 M hydrochloric acid and converted to nitrate by adding 30 ml of fuming nitric acid. The time at the end of this precipitation was taken as the zero time for the growth of lanthanum-140 from barium-140. Finally, the barium nitrate precipitate was dissolved in distilled water and made up to a known volume. Sources for β^- activity measurements were made by mounting an aliquot of the nitrate solution on gold-coated VYNS (a copolymer of polyvinyl chloride and polyvinyl acetate) films.[106]

For cumulative yield measurements of barium-141, barium chloride was separated, as discussed above, then left aside for at least 40 hours so that the barium-141 activity would be converted into cerium-141. The barium precipitate was then dissolved in distilled water and made up to volume. An aliquot of this solution was saved for the barium chemical yield determination and the rest of the solution was used for cerium separation in the form of cerium hydroxide.

(2) Cerium

Cerium was separated from other fission products using the procedure described by Boldridge and Hume.[107] The irradiated uranium target was dissolved in a lusteroid tube by adding a minimum quantity of concentrated nitric acid. Carriers for cerium (20 mg), lanthanum (20 mg), and zirconium (20 mg) were added immediately. The resulting mixture of solution was made 2 M in nitric acid and the fluorides precipitated by adding 2 ml of concentrated hydrofluoric acid. The fluorides in saturated borate solution were oxidized by sodium bromate in nitric acid and ceric iodate precipitated with 20 ml of 0.35 M iodic acid. The time at the end of the iodate precipitation was considered as the separation time of cerium from lanthanum. Repeated cycles of these operations were performed to separate completely cerium from other rare earths. Further purification was achieved by removing interfering zirconium activities in the form of zirconium iodate, and the supernate cerium solution was transferred in

a glass centrifuge tube. From this solution cerium was precipitated as its hydroxide by adding an excess amount of 12 M sodium hydroxide solution. The hydroxide precipitate was then dissolved in a small quantity of 6 M hydrochloric acid and diluted with distilled water to 10 ml volume. Sulphur dioxide gas was passed into the solution until the decolourization indicated complete reduction of any iodate, which had been carried over from the previous step, into iodide. Cerium hydroxide was then precipitated with a slight excess of concentrated ammonium hydroxide. This hydroxide precipitate was dissolved in a minimum quantity of dilute hydrochloric acid and made up to volume for gamma-activity measurements.

(3) Copper

In order to facilitate the ^{64}Cu activity measurements, it was essential to separate copper isotopes from other interfering activities of zinc, cobalt and nickel. Since the irradiated copper foil itself would act as a carrier for copper activity, no additional carrier was necessary. Before the chemical treatment of the foil, it was weighed accurately for the purpose of chemical yield determination.

The procedure adopted for copper separation was that described by Kraus and Moore.(108) The irradiated copper foil was dissolved in concentrated hydrochloric acid plus a few drops of 30% hydrogen peroxide. The solution was evaporated to dryness under an infra-red lamp and the residue was dissolved in 2 ml of concentrated hydrochloric acid. Then the solution

was passed through a Dowex-1 anion exchange column which was preconditioned by treating with 20 ml of 4.5 N hydrochloric acid. The column, containing resin of 100-200 mesh, was 12 cm long and 1 cm in diameter. For elution, 4.5 N hydrochloric acid was first passed through the column until the yellow-green coloured band of copper reached the end of the column. Then the eulant was changed to 1.5 N hydrochloric acid to remove copper. The initial and final portions of the eluate were discarded. The middle fraction was collected and made up to volume for activity measurements which were carried out about 30 hours after the end of an irradiation.

(4) Aluminum

No chemical separation for sodium-24 activity was necessary because of its relatively long half-life compared to all other interfering activities likely to be produced in the bombardment of aluminum. The whole irradiated aluminum foil was dissolved in dilute hydrochloric acid and made up to volume. Sodium-24 activity measurements were carried out about 24 hours after the end of an irradiation.

II-D. CHEMICAL YIELD DETERMINATION

(1) Barium

The chemical yields of barium were determined by titration with the disodium salt of ethylenediamine tetra-acetic acid in a 50% alcoholic solution, using phthalein complexone as an indicator.[105] The yields obtained were on the average about 50%.

(2) Copper

The chemical yields of copper were measured by bitration with the disodium salt of ethylenediamine tetra-acetic acid using mureoxide as an indicator.[105] The yields determined were of the order of 60-85%.

(3) Cerium

The chemical yields of cerium were determined spectrophotometrically on a Beckman DU spectrophotometer. The method employed is given by Sandell[109] where sodium alizarine sulphonate is used as a complexing agent. The standard absorbance curve obtained is shown in Fig. 5. The yields measured were on the average about 40%.

II-E. ACTIVITY MEASUREMENTS

(1) Preparation of Sources

The techniques of Pate and Yaffe[106] have been used for preparing thin films for measurements of beta-disintegration rates. Films were prepared from VYNS resin and a thin layer of gold was deposited to render them conducting. The superficial density of the films was between 10-15 μgm per cm^2 while that of gold coating was between 5-10 μgm per cm^2. These films were treated with insulin before using to make them hydrophilic. An aliquot of the fission product (barium) activity was pipetted on to the films and dried under an infra-red lamp. The fidms were rotated intermittently by hand to ensure uniform sources as far as possible.

FIGURE 5

STANDARD ABSORBANCE CURVE FOR CERIUM

(Sodium Alizarin Sulphonate Method)

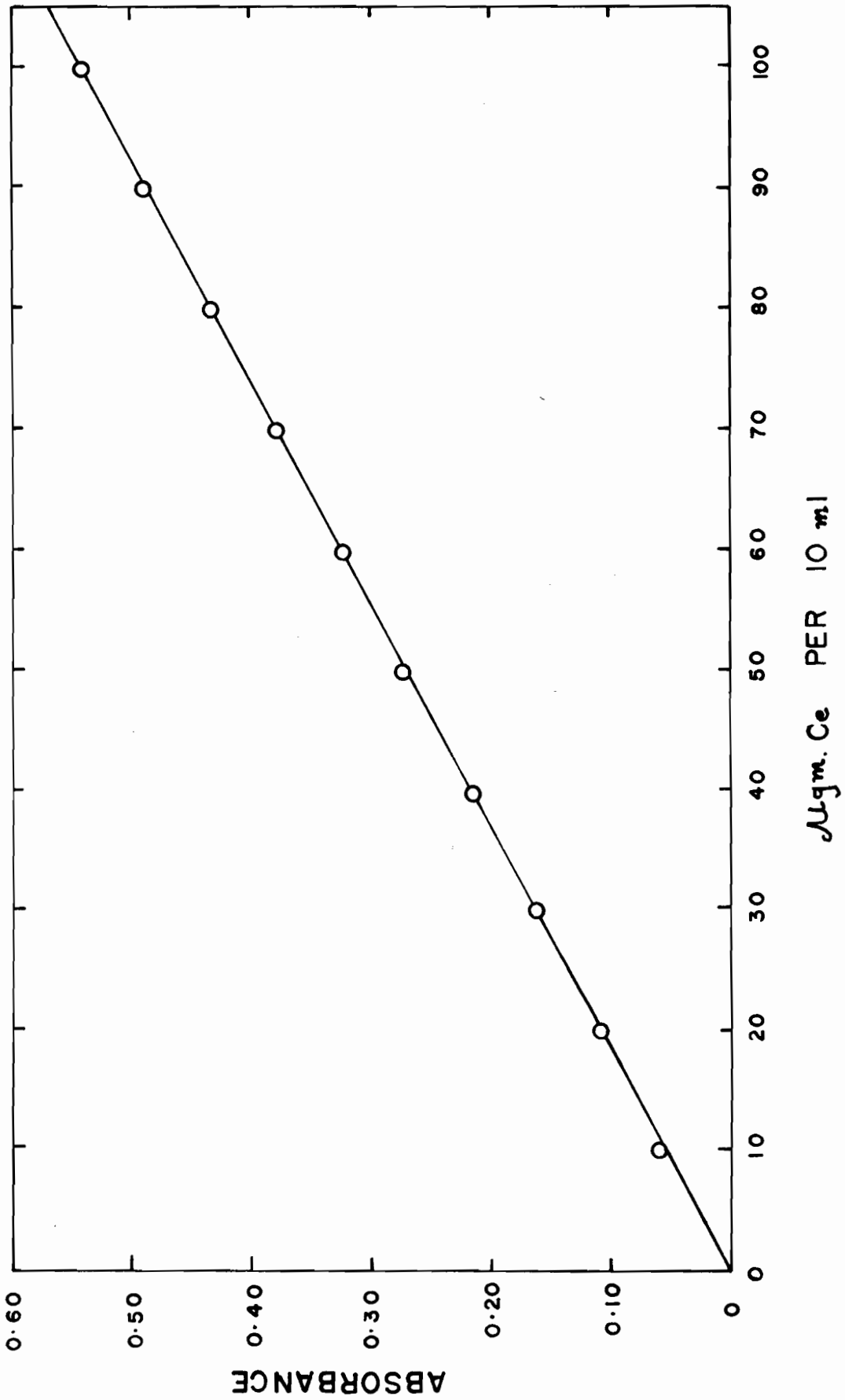
ABSORBANCE
0·60
0·50
0·40
0·30
0·20
0·10
0
0
10
20
30
40
50
60
70
80
90
100
Mgm. Ce PER 10 ml

For gamma-disintegration rate measurements, sources were prepared by pipetting 2 ml of active solution into a small screw-capped glass vial which was then sealed.

(2) Count Rate

Throughout this study either a methane-flow 4π β-proportional counter was used for β^- counting or a 3" x 3" NaI(Tl) crystal coupled to a multi-channel pulse height analyser was employed to measure the characteristic gamma-rays of particular nuclides.

(a) 4π β Method:

The techniques for the determination of rate of disintegration and necessary counting corrections to be applied for the 4π method are described by Pate and Yaffe[110-113], and Yaffe and Fishman.[114,115] This method has as its principal advantage a high geometrical efficiency and insensitivity to scattering effects. In addition, the technique of preparing thin films[106], as described above, makes this a relatively simple and very accurate method for β-ray measurements.

(i) Equipment:

The equipment used was similar to that described by Pate and Yaffe.[110] The counting chamber shown in Fig. 6 consisted of two hemispherical brass cathodes, 7 cm in diameter, and two loop-shaped anodes made of 1 mil tungsten wire connected to thicker copper leads. The anodes were insulated from the cathodes by teflon insulators. The two halves of the cathode, which were machined to fit together, allowed the positioning of

FIGURE 6

4π COUNTING CHAMBER

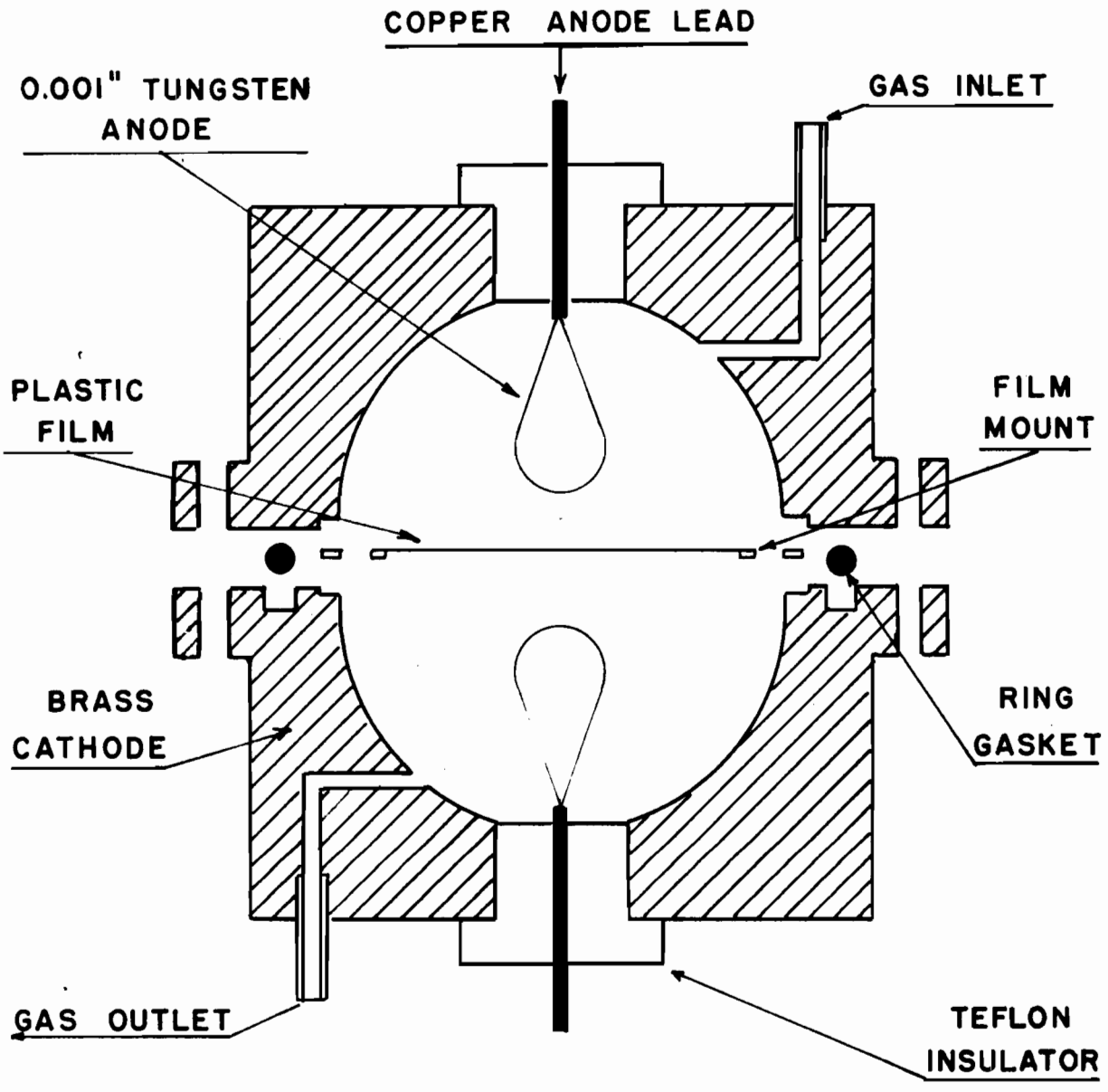
COPPER ANODE LEAD
0.001" TUNGSTEN ANODE
GAS INLET
PLASTIC FILM
FILM MOUNT
BRASS CATHODE
RING GASKET
GAS OUTLET
TEFLON INSULATOR

an aluminum film mount at exactly midway between the two anodes. Two holes were also provided for passing gas in and out of the chamber. A block diagram of the 4π counter and associated electronics is shown in Fig. 7. The cathodes were kept at ground potential, while the anodes received a positive high potential supplied by a Nichols high voltage supply (AEP 1007B). The two anodes were connected in parallel to a preamplifier (Atomic Instrument 205-B). The output from this was fed into an Atomic Energy of Canada Limited amplifier discriminator (AEP 1448). Counting rates were recorded on a Marconi sealer unit (AEP 908). Line voltage was supplied to the instrument through a Sola constant voltage transformer, and a Lambda regulated power supply (Model 28) delivered the plate and filament voltages to the preamplifier.

(ii) Counter Characteristics:

The counter chamber was operated in the proportional region with C.P. methane as the counting gas. The flow rate of the gas was kept approximately constant during measurements. The counter was flushed for several minutes before measurements started. The high voltage counter characteristics, as shown in Fig. 8, for the particular activity were established before the measurements were begun. Pate and Yaffe[110] have stated that, if an increase of 200 volts in polarization potential or a 10-volts decrease in discriminator bias causes no change in the counting rate observed, then the 4π counter is responding with maximum efficiency. Accordingly, the counter was operated at a polarization potential of 2700 volts and a

FIGURE 7

BLOCK DIAGRAM OF 4π COUNTING EQUIPMENT

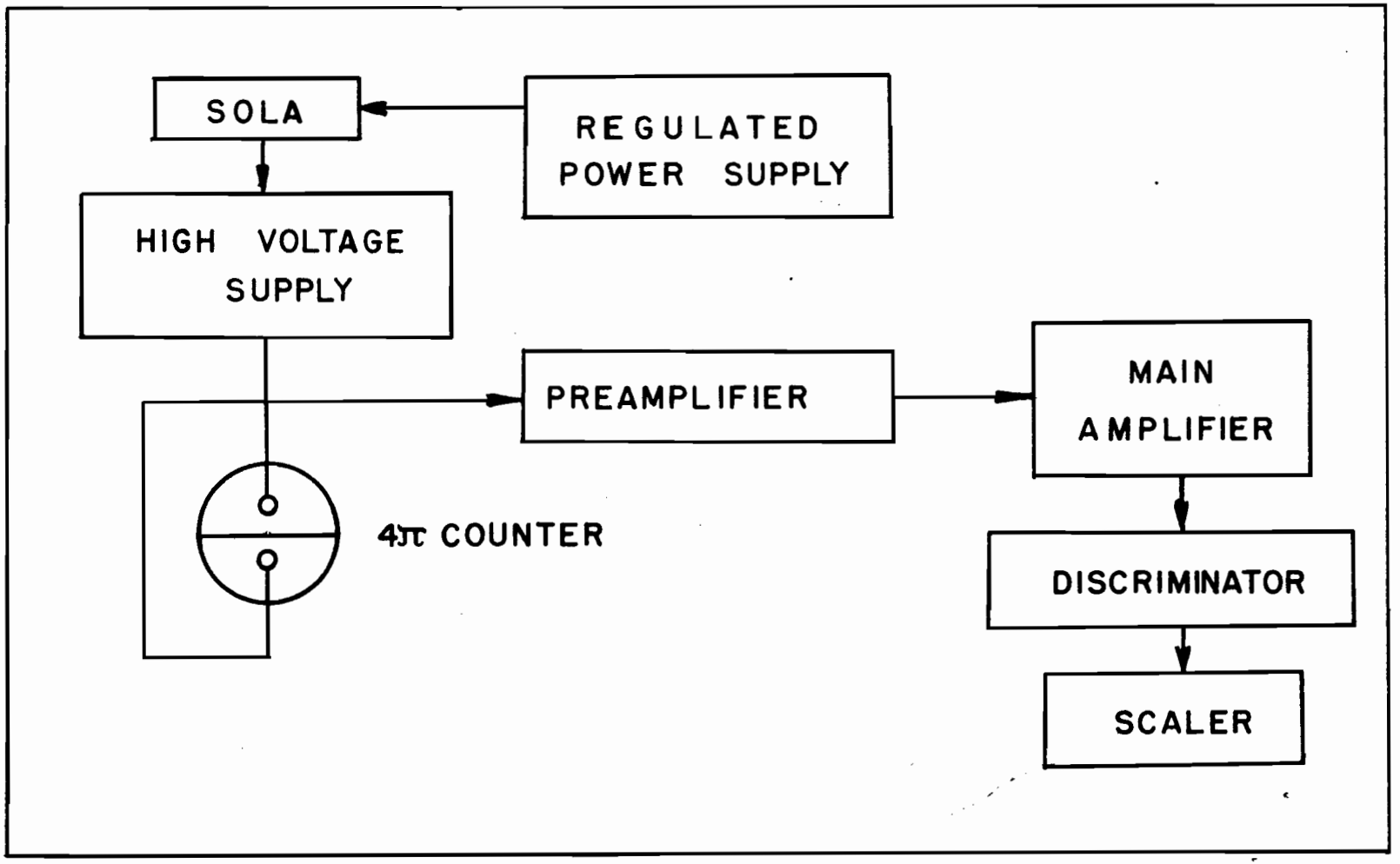
SOLA
REGULATED POWER SUPPLY
HIGH VOLTAGE SUPPLY
PREAMPLIFIER
MAIN AMPLIFIER
4π COUNTER
DISCRIMINATOR
SCALER

FIGURE 8

EFFECT OF VARYING THE BIAS SETTING ON THE HIGH VOLTAGE CHARACTERISTICS OF THE 4π COUNTER

● - 0 volt bias

X - 5 volt bias

□ - 10 volt bias

0 - 15 volt bias

⊗ - 20 volt bias

△ - 25 volt bias

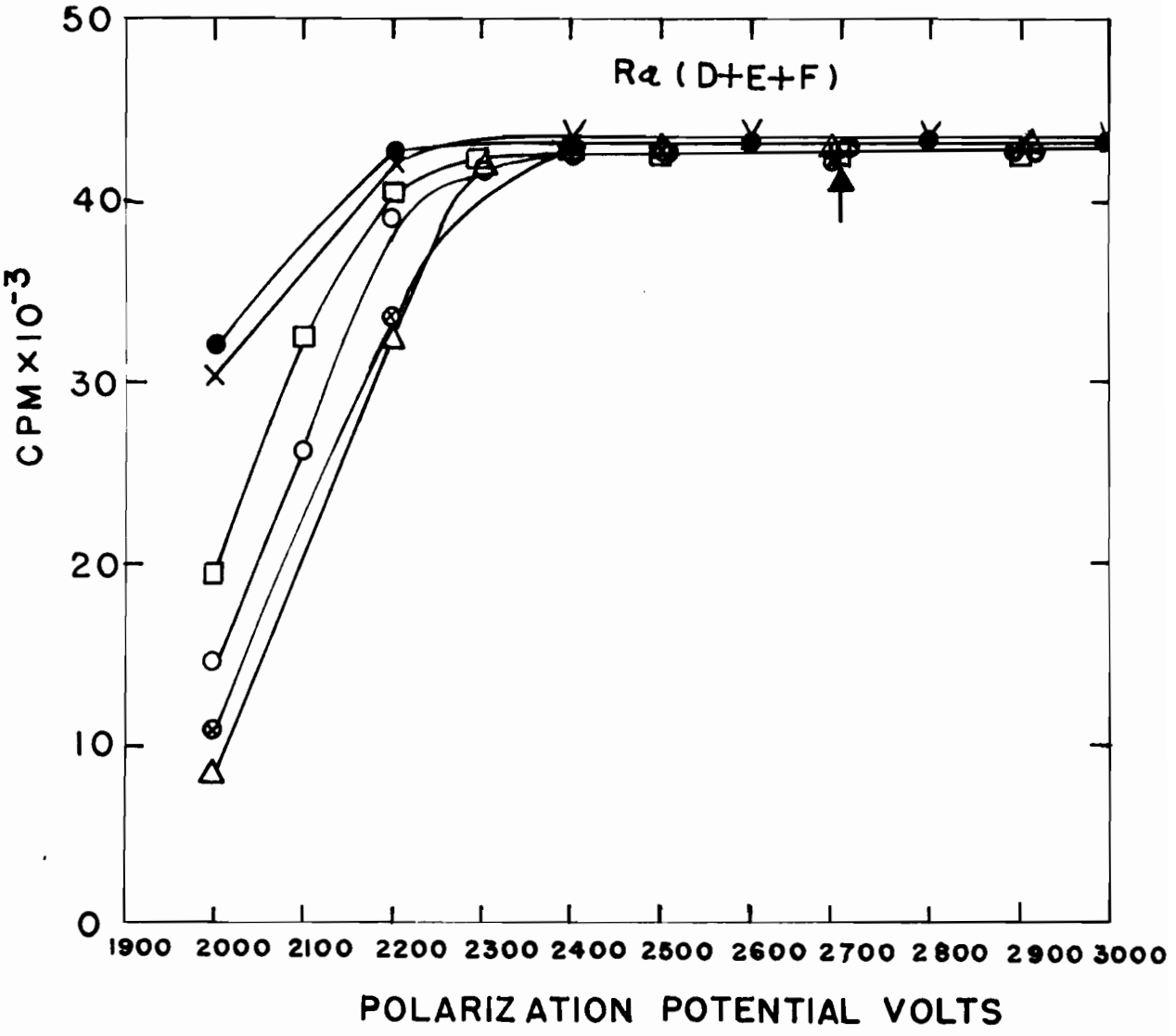
Ra (D+E+F)
CPM X 10-3
50
40
30
20
10
0
1900 2000 2100 2200 2300 2400 2500 2600 2700 2800 2900 3000
POLARIZATION POTENTIAL VOLTS

setting of 15 on the discriminator. Proper operation of the instrument was frequently checked by measuring Ra(D+E+F) standard before any series of measurements.

(b) Scintillation Method:

The gamma-ray detector consisted of a commercially available (Harshaw Chemical Company) 3" x 3" sodium iodide crystal, activated with about 0.1% thallium iodide, optically coupled to a Du Mont type 6364 photomultiplier tube. The crystal was hermetically sealed in an aluminum can and the whole assembly enclosed in a lead cylinder (1½" thick) to reduce the background pulses. The fluorescent radiation from the lead was attenuated by lining the inside of the cylinder with iron and lucite.

The output pulses from the photomultiplier tube were fed through a preamplifier (RIDL Model 31-15) to a variable gain linear amplifier which was connected to the RIDL (Model 34-12B) 400 channel multiscaler. The pulses were accumulated and stored in the memory of the analyser. The stored data were printed out on a Hewlett Packard (H43 562A) print-out system. The analyser counts in the 'live time' mode so no corrections for dead time losses were necessary.

The resolution of one NaI(Tl) crystal was about 12.8 per cent for the 0.662 MeV gamma-ray of ^{137}Cs. All the gamma-ray measurements, except those of ^{139}Ce, were done with this crystal. Cerium-139 gamma activity was measured with another NaI(Tl) crystal which has a resolution of 8 per cent.

The efficiency curves for gamma rays of various energies at different geometry for the first crystal (resolution about 12.8%) are reported by Grant.[116] These values were used in the present work, except for ^{139}Ce. The efficiency for the 0.166 MeV gamma-ray of ^{139}Ce was determined by calibrating the second crystal (resolution 8%) with respect to the first crystal using ^{139}Ce standard at a fixed geometry. The calibration was also checked by employing a known ^{141}Ce (0.145 MeV γ) sample.

III. TREATMENT OF DATA

III-A. ANALYSIS OF GAMMA-RAY SPECTRA

The energies of the photopeaks were determined by using an energy calibration curve (energy versus channel number). This curve was prepared by measuring different gamma rays of several long-lived standard sources (e.g. ^{139}Ce, ^{137}Cs, ^{60}Co, ^{22}Na, etc.).

The area of the photopeak was determined by an approach similar to that adopted by the group that determined the photopeak efficiencies.(116) The backgrounds were hand-drawn after taking into account all phenomena occurring under the peak.

For a simple spectrum, as for ^{64}Cu, the background was estimated as shown by the dotted line in Fig. 9. The area of the 511 KeV photopeak was calculated by summing up the counts in each channel under the peak and subtracting the estimated background from the total.

For ^{24}Na, which emits 1.368 MeV and 2.75 MeV gamma rays in cascade, only the 1.368 MeV gamma ray was followed and its spectrum obtained by selecting an appropriate gain. The 'coincidence summing' effect was minimized by measuring the sources under conditions of low geometrical efficiency. A typical spectrum is shown in Fig.10. The dotted line shows the hand-drawn background, and the area of the 1.368 MeV photopeak was determined by subtracting the estimated background from the

FIGURE 9

TYPICAL GAMMA-RAY SPECTRUM OF COPPER SAMPLE

(Dotted line indicates the estimated background.
0.511 MeV peak is due to ^{64}Cu)

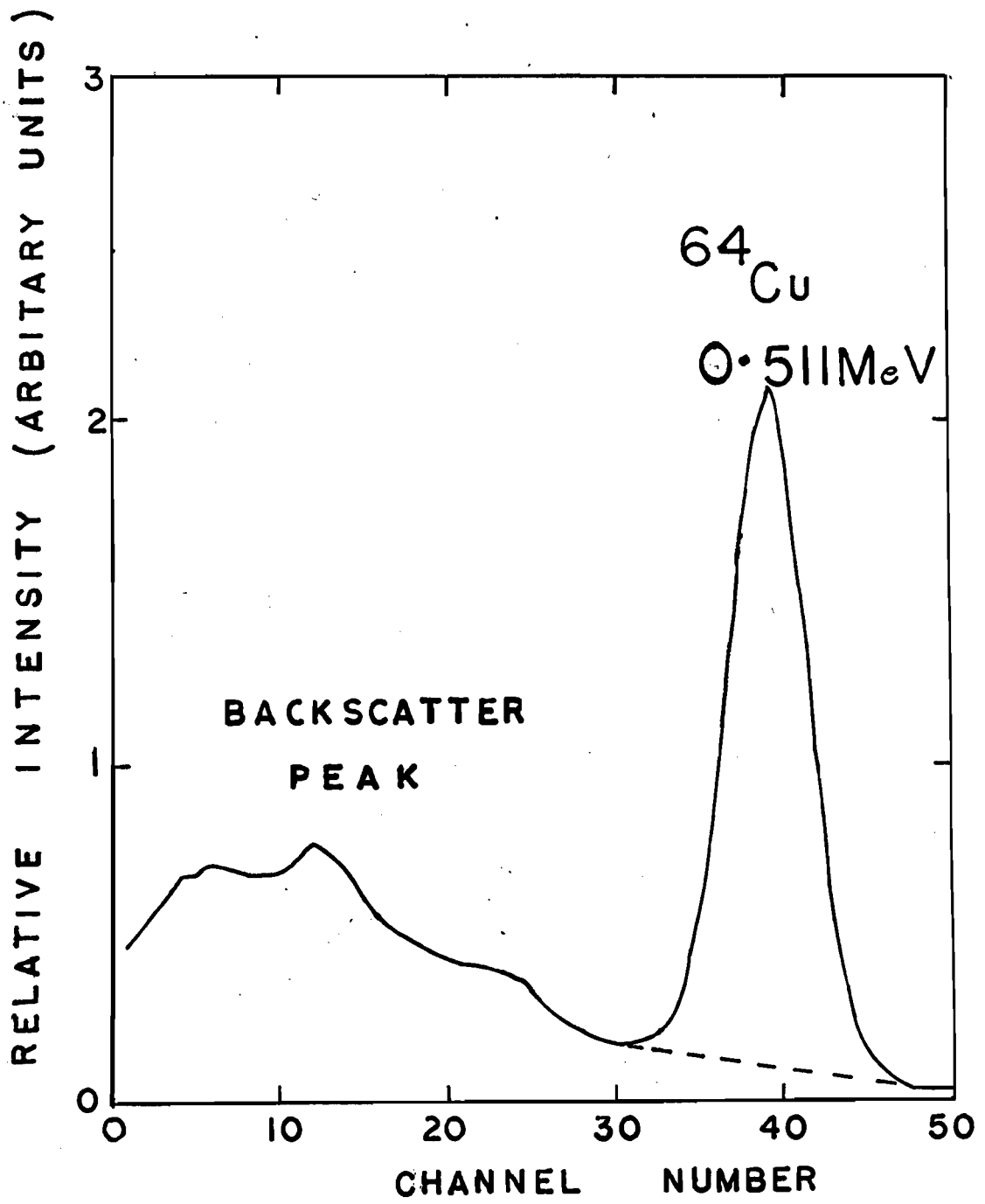
RELATIVE INTENSITY (ARBITARY UNITS)
3
2
1
0
0
10
20
30
40
50
CHANNEL NUMBER
64Cu
0·511MeV
BACKSCATTER
PEAK

FIGURE 10

TYPICAL GAMMA-RAY SPECTRUM OF ALUMINUM SAMPLE

(Dotted line indicates the estimated background.
1.368 MeV peak is due to ^{24}Na)

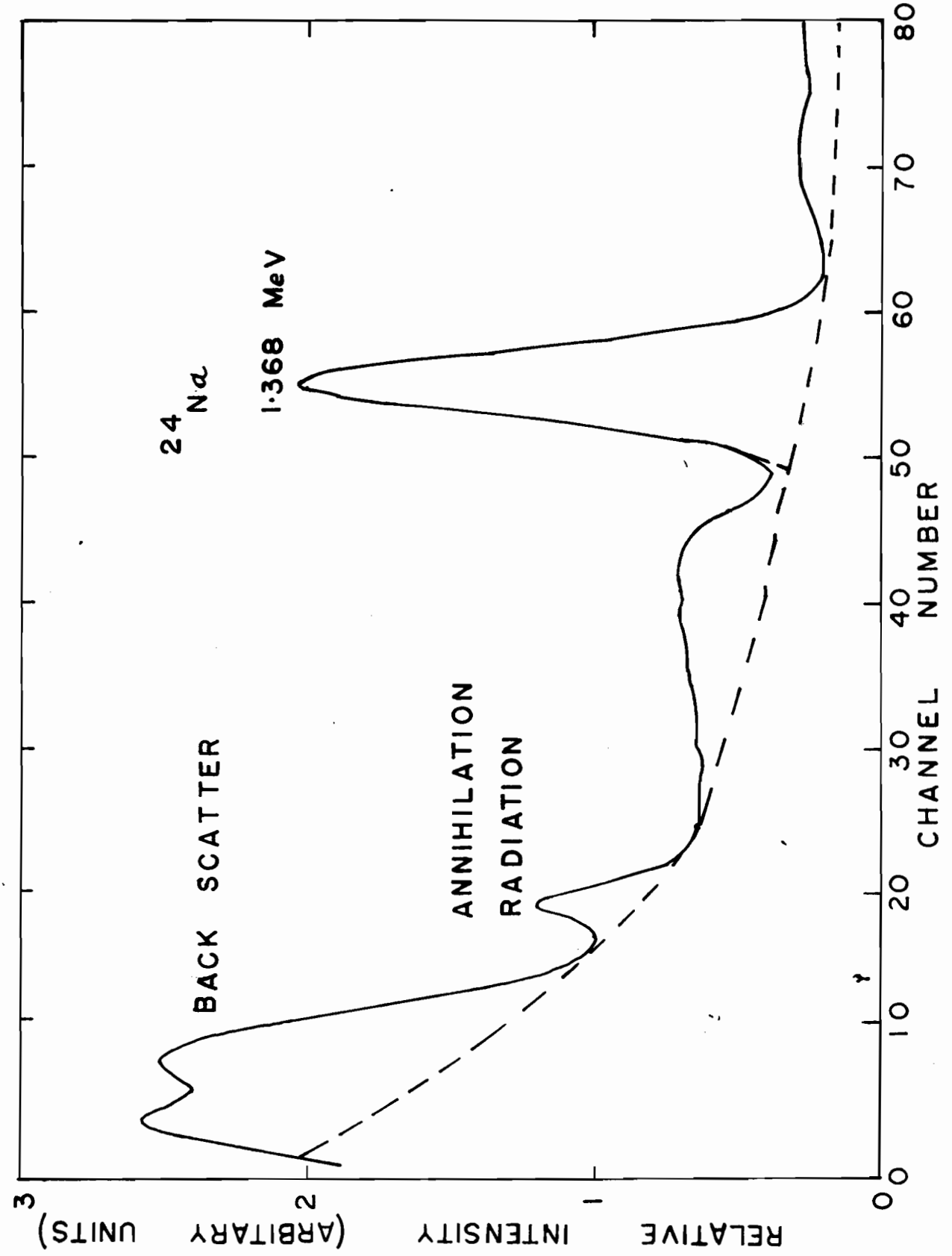
RELATIVE INTENSITY (ARBITARY UNITS)
CHANNEL NUMBER
0
1
2
3
10
20
30
40
50
60
70
80
BACK SCATTER
ANNIHILATION RADIATION
^{24}Na
1·368 MeV

total area of the peak. The contribution from the 1.28 MeV gamma ray of ^{22}Na was found to be less than one per cent. Hence it was considered negligible.

In the case of ^{139}Ce, the irradiated targets were left aside for about one year before processing. This allowed all cerium isotopes, except ^{139}Ce and ^{144}Ce, to decay to their stable daughter products. Cerium-144 decays by beta- and gamma-ray emission, the most abundant gamma ray having an energy of 134 KeV. Cerium-139 decays 100% by electron capture followed by 166 KeV gamma emission. It was possible to resolve the 134 KeV gamma ray from the 166 KeV gamma ray on the NaI(Tl) crystal which had a resolution of 8%. The typical spectrum obtained about one year after bombardment is shown in Fig. 11. The dotted line on the spectrum is the estimated background.

The area of the 166 KeV photopeak of ^{139}Ce, taking the specific example in Fig. 11, was calculated as follows. The peak was taken to be symmetrical about channel 49 and the counts in each channel from 50 to 56 were totalled. This total was then doubled and the counts in channel 49 were added to it. The background counts were similarly determined and were subtracted from the total peak area.

The activity of ^{141}Ce was measured about 15 days after bombardment. This yielded a ^{141}Ce spectrum undistorted by ^{143}Ce. A typical spectrum is shown in Fig. 12. The dotted line indicates the estimated background. The spectrum shows clearly an escape peak, and hence the area of the 0.145 MeV photopeak was determined in the same way as that described above in the case of ^{139}Ce. In addition, that method of

FIGURE 11

TYPICAL GAMMA-RAY SPECTRUM OF CERIUM SAMPLE

TAKEN ABOUT ONE YEAR AFTER BOMBARDMENT

(Dotted line indicates the estimated background. Prominent 0.134 MeV peak is due to 284 d. ^{144}Ce and 0.166 MeV peak is due to 140 d. ^{139}Ce)

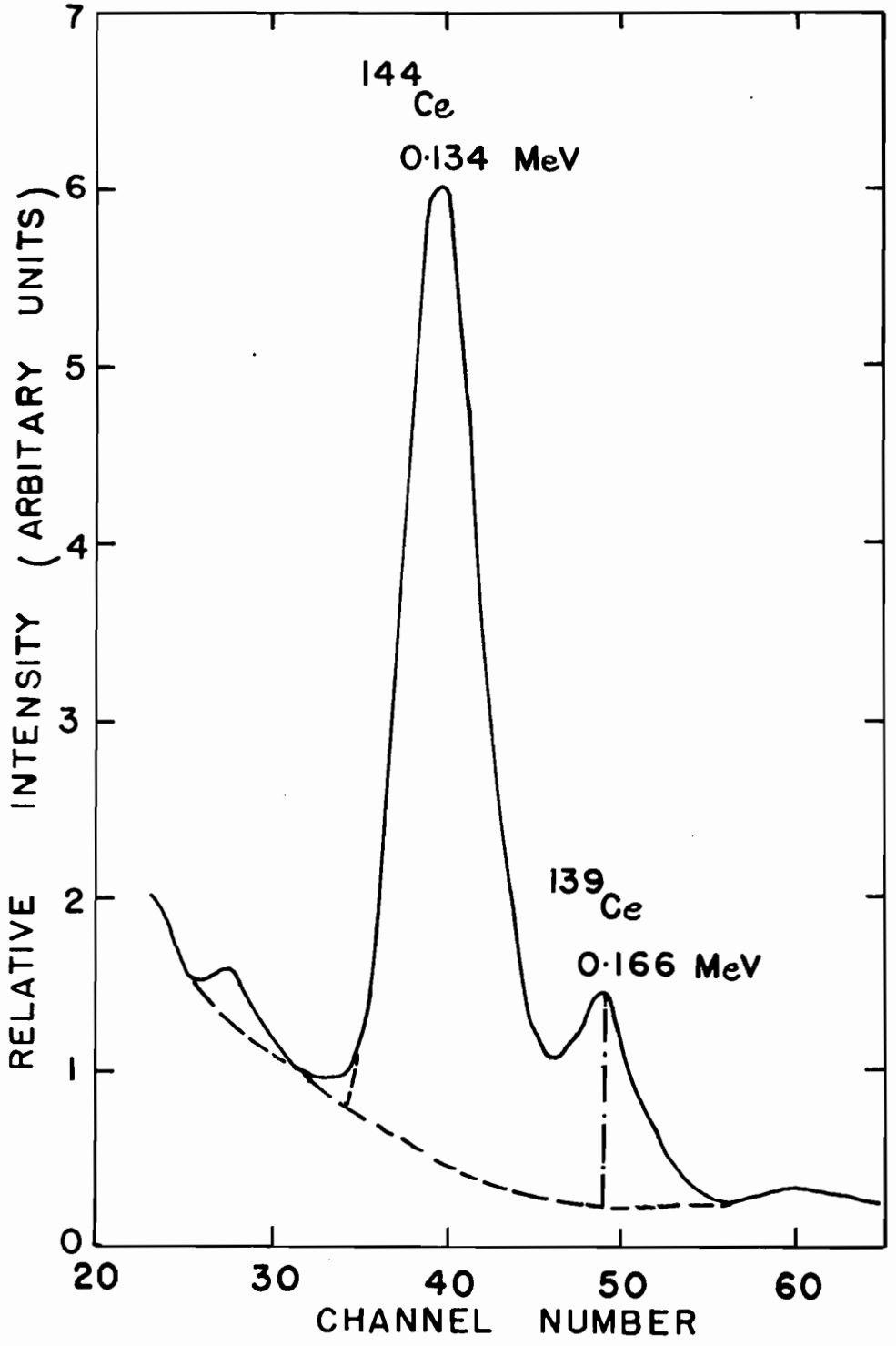
144 Ce
0·134 MeV
139 Ce
0·166 MeV
RELATIVE INTENSITY (ARBITARY UNITS)
CHANNEL NUMBER
0
1
2
3
4
5
6
7
20
30
40
50
60

FIGURE 12

TYPICAL GAMMA-RAY SPECTRUM OF CERIUM SAMPLE

TAKEN FIFTEEN DAYS AFTER BOMBARDMENT

(Dotted line indicates the estimated background.
0.145 MeV peak is due to ^{141}Ce)

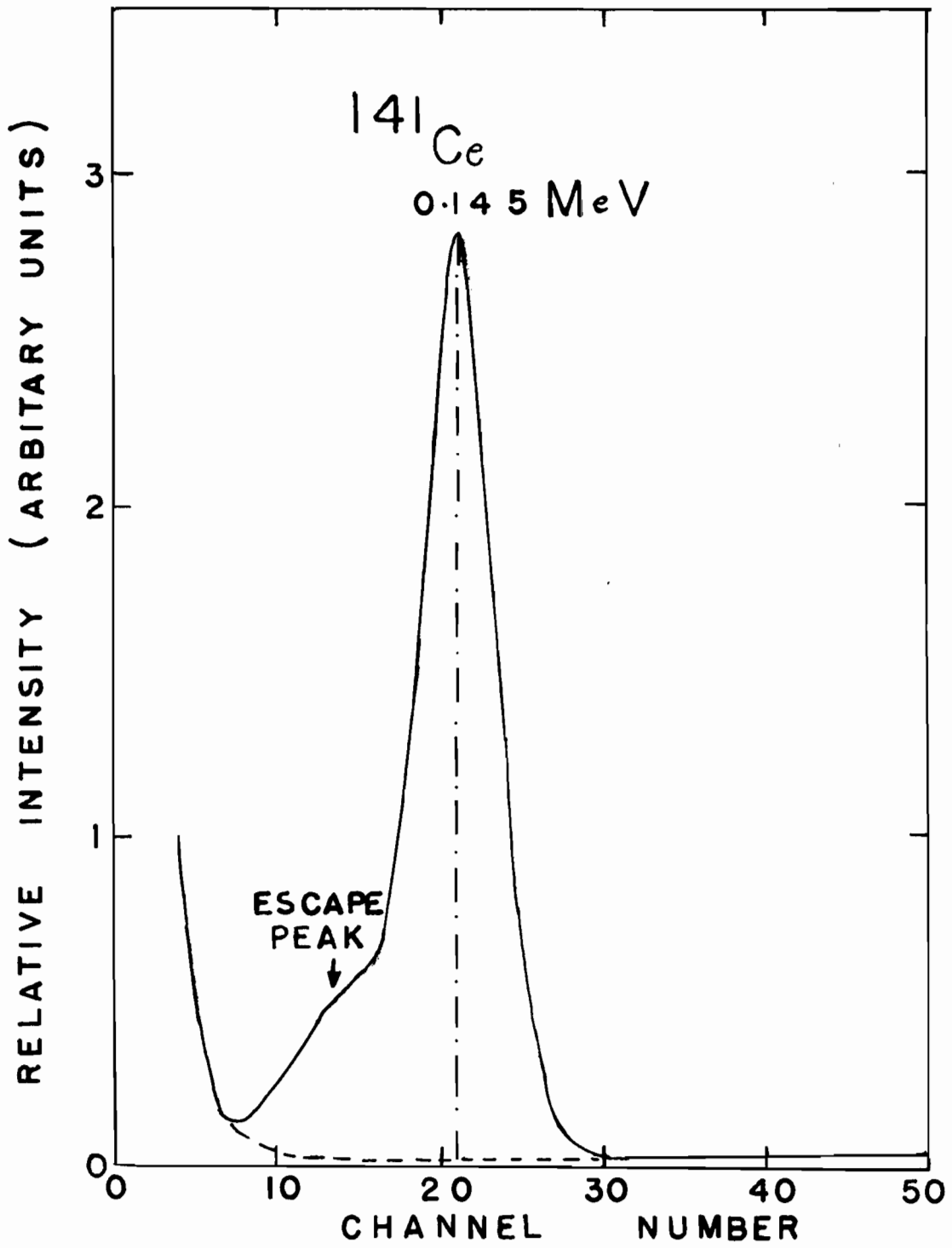
141 Ce
0·145 MeV
ESCAPE PEAK
RELATIVE INTENSITY (ARBITARY UNITS)
0
1
2
3
0
10
20
30
40
50
CHANNEL NUMBER

determining the peak area for the 0.145 MeV photopeak avoids the contribution (if any for the short period of irradiation) from the 0.134 MeV gamma ray of ^{144}Ce. The contribution from the 0.166 MeV gamma ray of ^{139}Ce is negligible due to the fact that ^{139}Ce production was generally very small because ^{139}Ce is a neutron-deficient nuclide. Furthermore, both ^{144}Ce ($t_{\frac{1}{2}}$ = 284 d.) and ^{139}Ce ($t_{\frac{1}{2}}$ = 140 d.) have a long half-life compared to that of ^{141}Ce ($t_{\frac{1}{2}}$ = 32.5 d.) and so the resulting counting rate for these nuclides will be quite low compared to that for ^{141}Ce.

In irradiations where the activity of ^{141}Ce resulted only from the decay of ^{141}Ba, the counting rate of ^{141}Ce, as measured above, was used to calculate the ^{141}Ba counting rate.

In the case of ^{143}Ce, it was not possible to resolve its 293 KeV and 351 KeV gamma rays, hence a composite peak was followed and the background was estimated as shown by the dotted line in Fig. 13. The area of the composite photopeak was found by summing the counts in each channel under the peak and subtracting the estimated background from the total.

The area of the desired photopeak was then converted into a photon emission rate, N_γ, from the following expression:

$$N_\gamma = \frac{A_p}{E_p \times \Delta t} \qquad \text{(III-1)}$$

where A_p = the area under the photopeak,

E_p = overall photopeak efficiency for the particular photon energy and source position, and

Δt = duration of measurement.

FIGURE 13

TYPICAL GAMMA-RAY SPECTRUM OF CERIUM SAMPLE

(Dotted line indicates the estimated background.
A composite peak of 0.293 MeV + 0.351 MeV
gamma rays is due to ^{143}Ce)

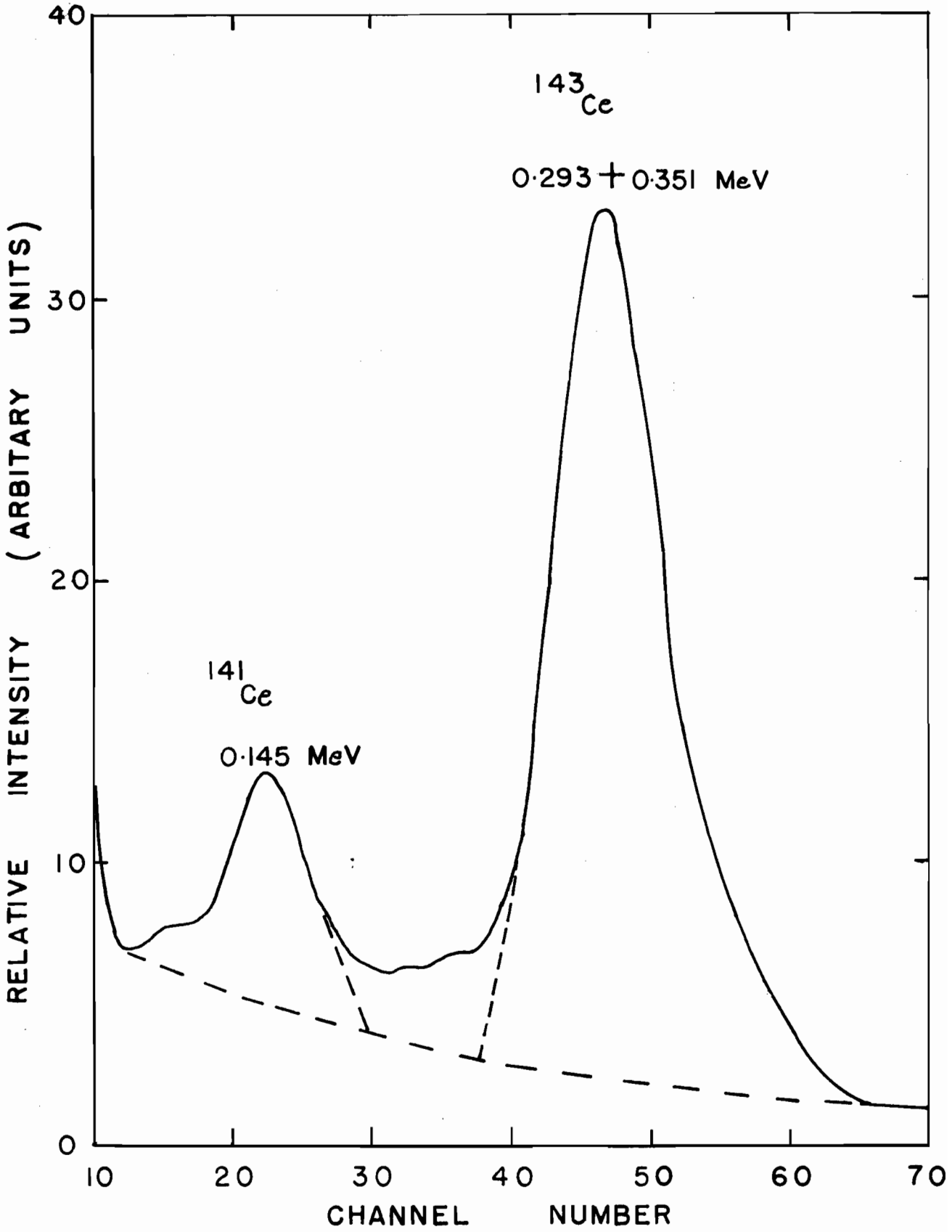
40
30
20
10
0
RELATIVE INTENSITY (ARBITARY UNITS)
143 Ce
0·293 + 0·351 MeV
141 Ce
0·145 MeV
10
20
30
40
50
60
70
CHANNEL NUMBER

III-B. DECAY CURVE ANALYSIS

All decay curves, with the exception of those from the barium samples, yielded a straight line corresponding to the half-life of a single radioactive nuclide.

The decay curves for the barium samples were multicomponent. It was found that the curved line (Fig. 14) tails off into a straight line with a slope corresponding to a half-life of 12.8 d. This was identified as ^{140}Ba and, since it decays to 40.2-hrs ^{140}La, there will be a transient equilibrium ($\lambda_{^{140}Ba} < \lambda_{^{140}La}$). The contribution due to ^{140}Ba and ^{140}La which grows in from its separation time was calculated by applying appropriate equations. The details of these equations are given in Appendix C. The ^{139}Ba activity was then found after subtracting ^{140}Ba - ^{140}La contribution from the observed gross counts.

Typical decay curves obtained for the particular nuclides are shown in Figs. 14-18 inclusive. The activity measurements were made frequently in the beginning and later at longer intervals for a period of two to four half-lives. For ^{139}Ba, measurements were made until it had decayed completely, then the ^{140}Ba - ^{140}La background activity was followed for correction purposes. The half-lives obtained were 84.0 $\pm$ 0.4 min. for ^{139}Ba, 32.5 $\pm$ 0.7 d. for ^{141}Ce, 33.0 $\pm$ 0.5 hr. for ^{143}Ce, 15.0 $\pm$ 0.2 hr. for ^{24}Na, and 12.8 $\pm$ 0.2 hr. for ^{64}Cu.

III-C. DETERMINATION OF DISINTEGRATION RATES

The counting rates, C.R.^{o} or C.R.^{s}, were obtained by

FIGURE 14

DECAY CURVE FOR 84.0-MINUTE ^{139}Ba

O - Experimental points

- - - - Calculated ^{140}Ba + ^{140}La

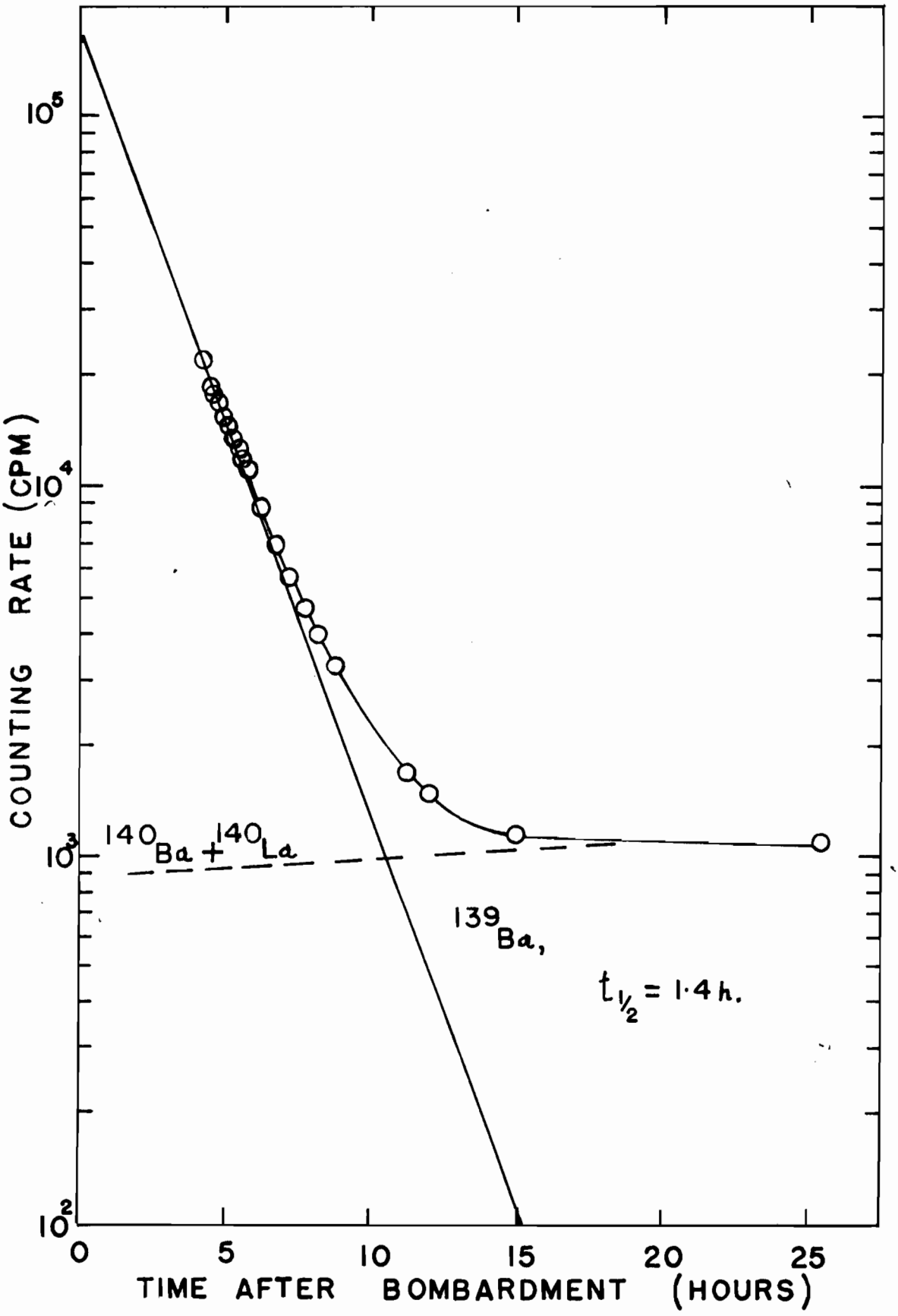
COUNTING RATE (CPM)
10^5
10^4
10^3
10^2
$^{140}Ba + ^{140}La$
^{139}Ba,
$t_{1/2} = 1.4$ h.
0
5
10
15
20
25
TIME AFTER BOMBARDMENT (HOURS)

FIGURE 15

DECAY CURVE FOR 32.5-DAY ^{141}Ce

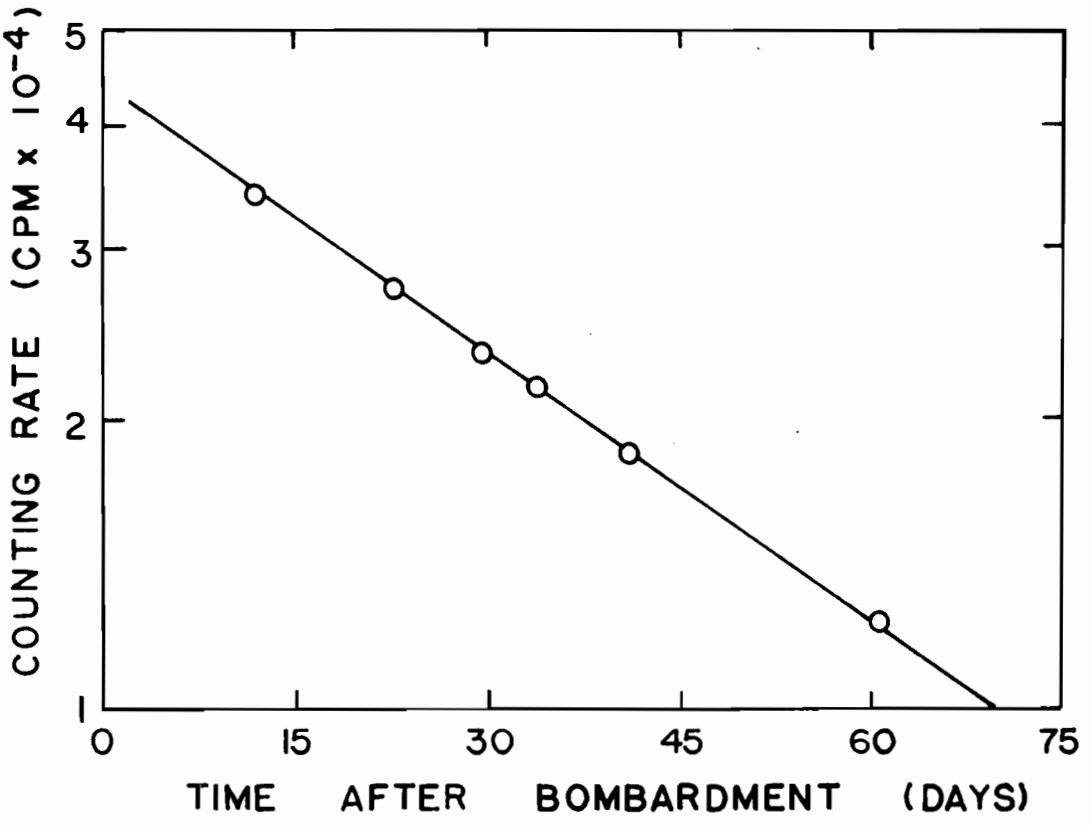
COUNTING RATE (CPM x 10⁻⁴)
5
4
3
2
1
0
15
30
45
60
75
TIME AFTER BOMBARDMENT (DAYS)

FIGURE 16

DECAY CURVE FOR 33.0-HOUR ^{143}Ce

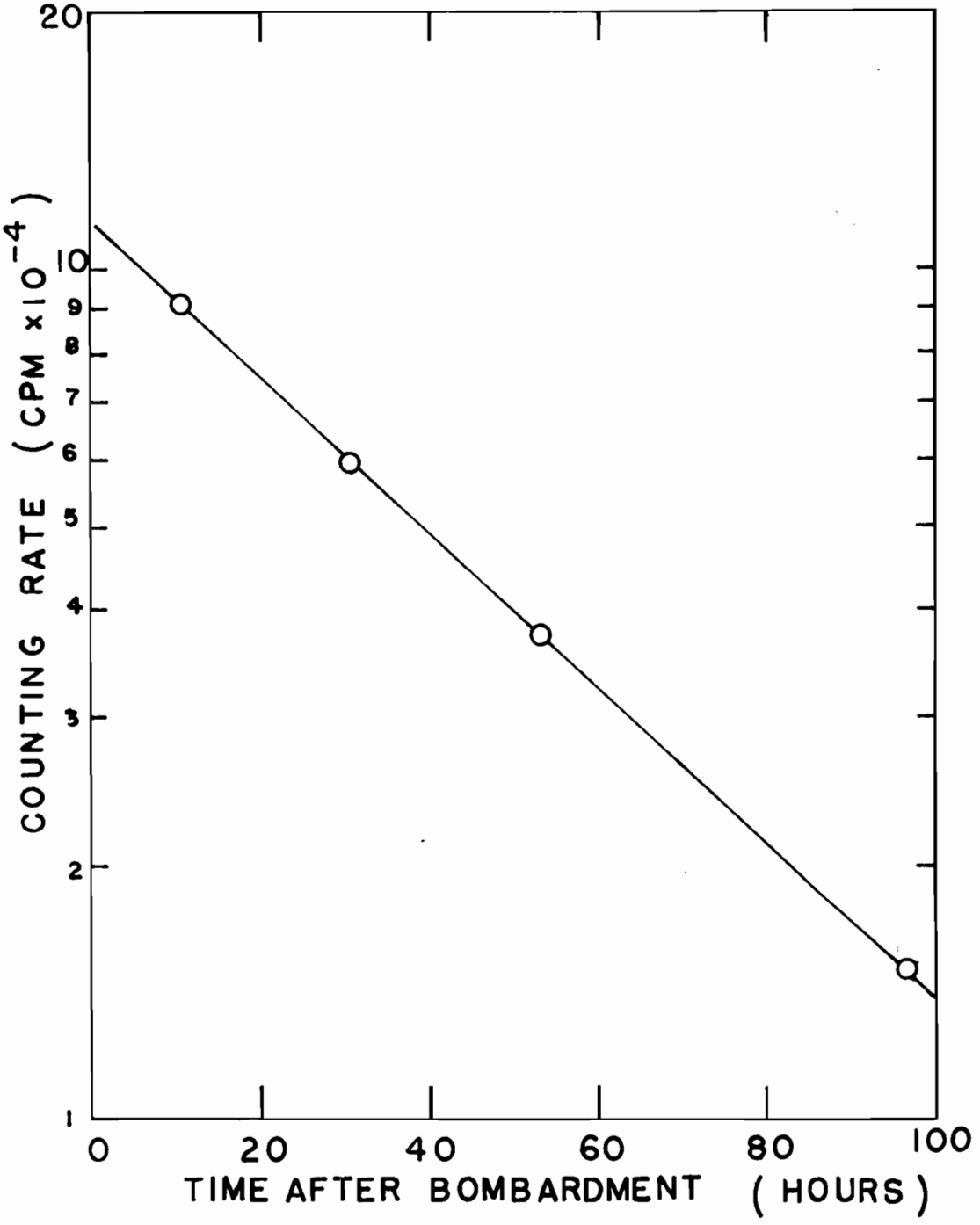
20
10
9
8
7
6
5
4
3
2
1
COUNTING RATE (CPM x10^{-4})
0
20
40
60
80
100
TIME AFTER BOMBARDMENT (HOURS)

FIGURE 17

DECAY CURVE FOR 15.0-HOUR ^{24}Na

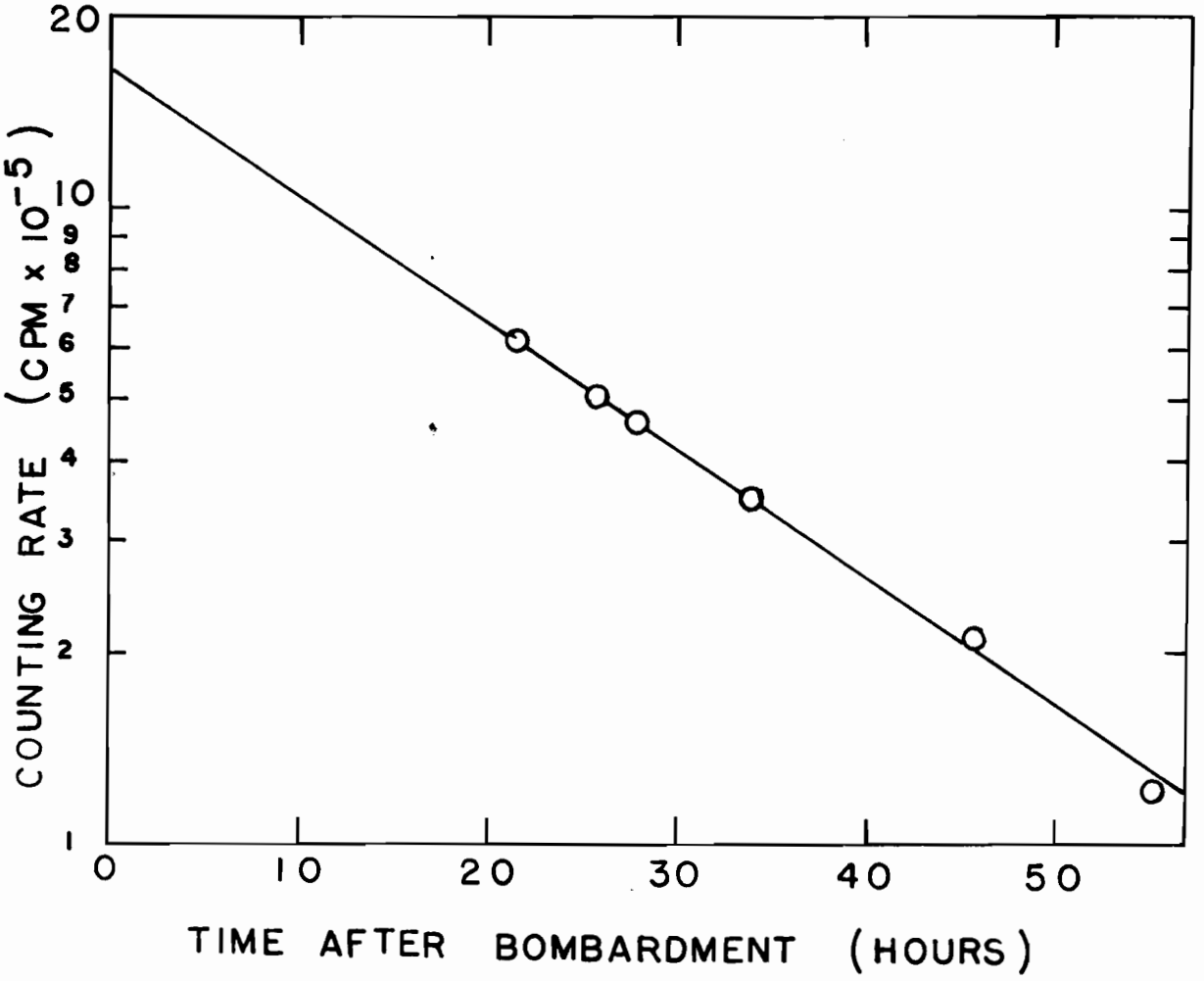
20
10
9
8
7
6
5
4
3
2
1
COUNTING RATE (CPM x 10^{-5})
0
10
20
30
40
50
TIME AFTER BOMBARDMENT (HOURS)

FIGURE 18

DECAY CURVE FOR 12.8-HOUR ^{64}Cu

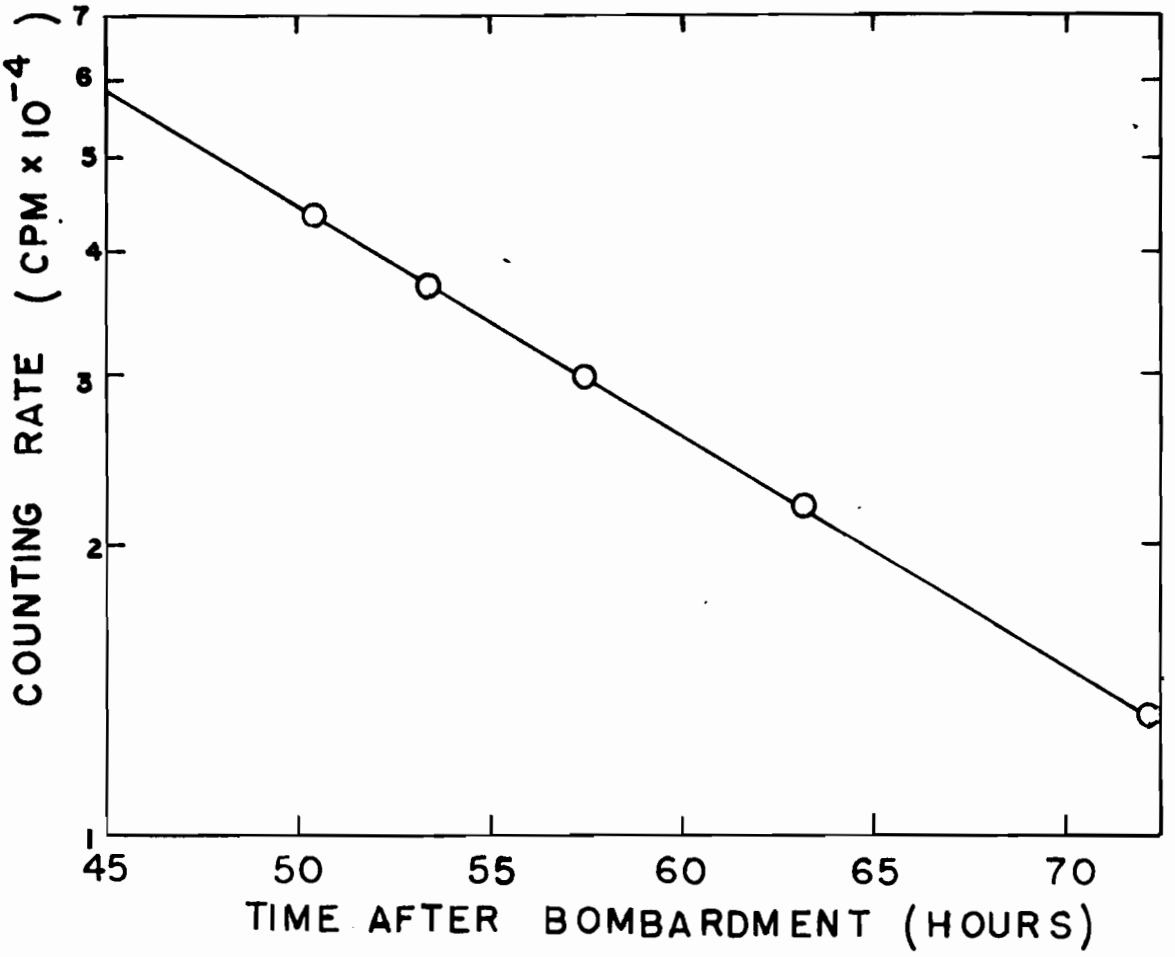
COUNTING RATE (CPM x 10⁻⁴)
7
6
5
4
3
2
1
45
50
55
60
65
70
TIME AFTER BOMBARDMENT (HOURS)

extrapolating the decay curves back to the end of bombardment, t^o, or to the separation time, t^s, respectively. These counting rates were corrected for chemical yield and dilution to determine the total emission rates, N^o or N^s at t^o or t^s.

(1) Conversion of Beta-Particle Counting Rates to Disintegration Rates

The total counting rate, N_β^s, at the time of separation was converted into the disintegration rate, D^s, at t^s from the following expression:

$$D^s = \frac{N_\beta^s}{(B.R.)_\beta} \qquad \text{(III-2)}$$

where $(B.R.)_\beta$ is the branching ratio for the beta emission.

For ^{139}Ba, since it has very energetic beta rays, corrections for source-mount absorption and self-absorption were negligible. Corrections for resolution losses were avoided by keeping counting rates less than 10^5 counts per minute. At least 10,000 counts were registered during a counting period for good statistics. Sources were prepared in triplicate and those that deviated by more than one per cent were discarded. The background counting rate of the instrument used varied between 45 c.p.m. to 55 c.p.m.

(2) Conversion of Gamma Counting Rates to Disintegration Rates

From a knowledge of branching ratios and internal conversion coefficients, the total photon emission rates, N_γ^o

or N_γ^s, were converted into the disintegration rates, D^o or D^s, by the following equation:

$$D^o = N_\gamma^o \times \frac{1 + \alpha_T}{(B.R.)_\gamma} \quad \text{or} \quad D^s = N_\gamma^s \times \frac{1 + \alpha_T}{(B.R.)_\gamma} \qquad \text{(III-3)}$$

where α_T = internal conversion coefficient, and

$(B.R.)_\gamma$ = fraction of the gamma transitions that this gamma represents (branching ratio).

The branching ratios and internal conversion coefficients were obtained from Nuclear Data Sheets[117] and from more recent literature.

(3) Calculations of Disintegration Rates for ^{139}Ce and ^{141}Ba

For ^{139}Ce, the total emission rate, N_γ^t at a time t, after the end of an irradiation (about one year later) was converted into the disintegration rate, D^o, from the following expression:

$$D^o = N_\gamma^t \times \frac{1 + \alpha_T}{(B.R.)_\gamma} \times \frac{1}{e^{-\lambda t}} \qquad \text{(III-4)}$$

where λ = decay constant for ^{139}Ce, and

t = time interval between the end of bombardment and the time of actual measurement of activity.

In the case of ^{141}Ba, which was allowed to decay completely to ^{141}Ce, the total emission rate, N_γ^s, for ^{141}Ce at

$t_s(^{141}Ba)$, the time of separation of ^{141}Ba as barium chloride, was converted into $D^s(^{141}Ce)$ at $t_s(^{141}Ba)$. The disintegration rate for ^{141}Ba, $D^o(^{141}Ba)$, was then calculated in the following way:

$$D^o(^{141}Ba) = D^s(^{141}Ce) \times \frac{\lambda(^{141}Ba)}{\lambda(^{141}Ce)} \times \frac{1}{C.Y.(^{141}Ba)} \times \frac{1}{e^{-\lambda(^{141}Ba)t}} \quad \text{(III-5)}$$

where t = elapsed time from the end of bombardment to the time of separation of ^{141}Ba,

$C.Y.$ = chemical yield of ^{141}Ba, and

$$\frac{\lambda(^{141}Ba)}{\lambda(^{141}Ce)} = 2.6 \times 10^3.$$

III-D. CALCULATIONS OF CROSS-SECTIONS

In the present study, natural uranium is considered as monoisotopic (^{238}U). Aluminum is monoisotopic whereas copper has two stable isotopes, ^{63}Cu (69.1% abundance) and ^{65}Cu (30.9% abundance) and the natural abundance was taken into account for cross-section calculations.

The cumulative formation cross-sections of ^{139}Ce and ^{141}Ba were calculated from equation (A-8) derived in Appendix A,

$$\sigma_A = D_A^{\infty} \times F \quad \text{(A-8)}.$$

For parent-daughter pairs, $^{139}Cs \rightarrow {}^{139}Ba$, $^{141}La \rightarrow {}^{141}Ce$, and $^{143}La \rightarrow {}^{143}Ce$, two separate targets were irradiated at each bombarding energy with chosen periods of

irradiation and fixed time intervals between separation and the end of bombardment, each leading to an equation of the form of equation (B-15) derived in Appendix B,

$$D_B^s = \frac{\lambda_B}{F} (K_1 \sigma_A + K_2 \sigma_B) . \qquad (B\text{-}15)$$

The cumulative formation cross-section, σ_A, of the parent nuclide and the independent formation cross-section, σ_B, of the daughter nuclide were calculated by solving these equations simultaneously.

For the mass chain,

$$\rightarrow {}^{141}\text{Ba} \rightarrow {}^{141}\text{La} \rightarrow {}^{141}\text{Ce} \rightarrow$$

the cumulative formation cross-section of ^{141}La was obtained, as mentioned above, and the cumulative formation cross-section of ^{141}Ba was determined separately as stated before. It was therefore possible to calculate the independent formation cross-section of ^{141}La.

III-E. MONITOR CROSS-SECTIONS

The monitor cross-section values used at each energy are given in Table I (p. 76). The values for copper are taken from corrected excitation functions of Meghir[118] and those for ^{24}Na from the analysis of Cumming.[119]

III-F. ERRORS

No errors have been assigned to branching ratios and internal conversion coefficient values were taken from Nuclear

TABLE I

MONITOR CROSS-SECTION VALUES (mb)

E_p	$^{65}Cu(p,pn)^{64}Cu$*	$^{27}Al(p,3pn)^{24}Na$**
20	240	-
30	388	-
40	264	-
50	212	-
60	-	8.65
70	-	9.60
80	-	10.05
85	-	10.20

*Meghir[118]

**J.B. Cumming[119]

Data Sheets[117] and more recent literature.

An uncertainty of $\pm$ 10% in the values of the ^{64}Cu cross-sections[118] and $\pm$ 6.5% for the ^{24}Na cross-sections[119] has been adopted. No allowance was made for uncertainties in the monitor cross-section values due to the uncertainty in the bombarding energy ($\sim$ 2 MeV).

An error limit of $\pm$ 5% in the efficiency values for the gamma counting[116] was adopted, whereas the small uncertainty in the efficiency of the 4π β-proportional counter has been neglected.

Since the half-lives reported in the present work are in good agreement with the literature values, the decay constants were obtained from the experimental half-lives, except for ^{139}Ce and ^{141}Ba. For these nuclides, the published values, ^{139}Ce - $t_{\frac{1}{2}}$ = 140 d. and ^{141}Ba - $t_{\frac{1}{2}}$ = 18.0 min, were used. No errors have been assigned to the decay constants.

Random errors arise from the determinations of disintegration rates, chemical yields, dilution factors, superficial densities of the target and monitor foils, etc. An estimated error for each of these factors is given below.

The main source of the error in cross-section values comes from the disintegration rate determinations. In the case where beta measurements were made, no complicated calculations were involved in determining the counting rate, and it was simple to construct the decay curves. However, an error of $\pm$ 3% was assigned to the counting rate obtained from the decay curve analysis.

For gamma measurements, the chief source of error lies in the determination of the photopeak area. This error was estimated to be $\pm$ 5%, except for ^{139}Ce where an error of $\pm$ 7% was assumed because of its low yield. An additional error of $\pm$ 5% was included for the decay curve analysis.

The chemical yields were determined at least in duplicate. Those of the copper monitor agreed within $\pm$ 2%, while the chemical yields of other elements were good to $\pm$ 5%.

The errors due to diluting and pipetting were minimized by using calibrated volumetric glass-ware and

micro-pipettes. A very sensitive microbalance was used for weighings. The estimated error due to these factors was assumed to be $\pm$ 2%.

The errors introduced in timing are believed to be small. The duration of an irradiation was known within a few seconds. All other timings, such as separation time, counting period, decay time for short-lived activities, etc., were taken on accurate stop-watches. An error of $\pm$ 1% was assumed for timing.

The probable error was computed from the square root of the sum of the squares of the individual errors cited above. The value varied from $\pm$ 10% to $\pm$ 15% for various fission products, and it is shown by the vertical bar at the points on the experimental excitation functions.

IV. RESULTS

The pertinent decay data and the detection instrument used for activity measurements of radioactive nuclides are summarized in Table II.

TABLE II

PERTINENT DATA AND DETECTION METHODS OF RADIOACTIVE NUCLIDES MEASURED

Nuclide	Half-life	Radiation Followed	Branch Abundance %	Internal Conversion Coefficient $(1 + \alpha_T)$	Detection Technique
^{139}Ba	84.0 min.	β^- 2.17 MeV + 2.34 MeV	100	-	4π*
^{139}Ce	140.0 d.	γ 0.166 MeV	100	1.25	PHA*
^{141}Ce	32.5 d.	γ 0.145 MeV	70	1.43	PHA
^{143}Ce	33.0 hrs.	γ 0.293 MeV + 0.351 MeV	40	1.03	PHA
^{24}Na	15.0 hrs.	γ 1.368 MeV	100	1.0	PHA
^{64}Cu	12.8 hrs.	β^+	19**	1.0	PHA

* 4π = 4π β-proportional counter.

PHA = Multichannel Pulse Height Analyser.

** For all calculation purposes, branching abundance for the 0.511 MeV γ-ray of ^{64}Cu is taken as 38%[116], i.e. 2 x 19%, since these gamma rays result from annhilation of the positrons.

The fission products studied occur in the following three mass chains:

(1) $\xrightarrow{\text{short}} {}^{139}\text{Cs} \xrightarrow{9.5\text{ m.}} {}^{139}\text{Ba} \xrightarrow{84.0\text{ m.}} {}^{139}\text{La}$ (stable) $\xleftarrow{140\text{ d.}} {}^{139}\text{Ce} \xleftarrow{\text{short}}$

(2) $\xrightarrow{\text{short}} {}^{141}\text{Ba} \xrightarrow{18.0\text{ m.}} {}^{141}\text{La} \xrightarrow{3.85\text{ h.}} {}^{141}\text{Ce} \xrightarrow{32.5\text{ d.}} {}^{141}\text{Pr}$ (stable)

(3) $\xrightarrow{\text{short}} {}^{143}\text{La} \xrightarrow{14.0\text{ m.}} {}^{143}\text{Ce} \xrightarrow{33.0\text{ h.}} {}^{143}\text{Pr} \xrightarrow{13.8\text{ d.}} {}^{143}\text{Nd}$ (stable)

The cross-section values, together with other experimental data determined for various nuclides, are summarized in Tables III to XII. The symbols used in these tables have the same meanings as those defined in Section III and in the Appendices. The probable errors associated with the values of cross-sections are those calculated from the estimated errors described in Section III-F.

For different parent-daughter pairs, two sets of data, determined at each energy for the calculations of the independent formation cross-section of daughter nuclide, σ_B, and the cumulative formation cross-section of parent nuclide, σ_A, are given in Tables III to VIII inclusive. Each of the two sets of data, shown in two successive rows at the same energy, leads to an equation of the form of equation (B-15) given in Appendix B.

The precursors of ^{139}Ce are very neutron-deficient nuclides which are not expected to be formed in the energy region investigated, and experimentally determined cumulative yield values (Table IX) of ^{139}Ce are considered as independent formation cross-sections. For proton bombarding energies

less than 70 MeV, ^{139}Ce was not formed in detectable quantity.

The data for the cumulative formation cross-sections of ^{141}Ba are summarized in Tables X and XI, whereas the extent of the independent formation of ^{141}La at each bombarding energy is given in Table XII.

The independent formation cross-section values of ^{143}Pr at 20 MeV to 85 MeV proton energies are interpolated from the charge dispersion curves constructed from the present data. (These curves are shown in Section V.) These values are given in Table XIII. No errors have been assigned to the ^{143}Pr cross-sections.

Excitation functions for the various fission products investigated are shown in Figs. 19 to 27 inclusive. At proton energies from 100 MeV to 1 GeV, the cross-section values are interpolated from the charge dispersion curves of Friedlander et al.[82] These are included to determine the energies at which the excitation functions reach their maxima. No error bars are shown for these interpolated values.

EXPLANATION OF SYMBOLS USED IN TABLES III TO XI

E_p = proton bombarding energy.

t_o = duration of bombardment.

t = time interval between the end of bombardment, t^o, and time of separation, t^s, of the nuclide in question, otherwise it is defined in the table.

N_γ = photon emission rate, equation III-1.

C.R.^{o} or C.R.^{s} = extrapolated counting rate at t^o or t^s respectively.

A.F. = aliquot factor, which is 100% unless given in the table.

C.Y. = chemical yield.

N^o or N^s = total emission rate at t^o or t^s respectively.

D^o or D^s = disintegration rate at t^o or t^s respectively, calculated from equation III-3, except for ^{139}Ba (equation III-2), ^{139}Ce (equation III-4), and ^{141}Ba (equation III-5).

$(S.D.)_T$ = superficial density of natural uranium foil (target). Note: $(S.D.)_{Cu} = 10.53$ mg/cm^2 and $(S.D.)_{Al} = 5.29$ mg/cm^2, as stated in Section II-A.

D^∞ and F - as defined in equation A-8 (Appendix A).

K_1 and K_2 - as defined in equation B-10 and B-11 respectively (Appendix B).

Note: In tables III to VIII the subscripts B and M refer respectively to daughter and monitor nuclides in question.

TABLE III

DISINTEGRATION RATE DATA FOR ^{139}Cs - ^{139}Ba PAIR

E_p MeV	t_o Min.	t Min.	$C.R._B^s$ c.p.m. x 10^{-5}	$(A.F.)_B$	$(C.Y.)_B$ %	$N_B^s=D_B^s$ c.p.m. x 10^{-7}	$C.R._M^o$ c.p.m. x 10^{-6}	$(C.Y.)_M$ %	N_M^o c.p.m. x 10^{-6}	D_M^o d.p.m. x 10^{-6}	$(1-e^{-\lambda_M t_o})$ x 10^{-3}	D_M^∞ d.p.m. x 10^{-8}
20	5.0	9.0	1.00	100	62.2	1.61	1.38	80.6	1.71	4.49	4.50	9.99
	7.0	12.0	1.49	100	62.3	2.39	1.41	58.1	2.42	6.37	6.28	10.14
30	5.0	11.0	1.78	100	62.9	2.83	1.79	46.4	3.86	10.16	4.50	22.58
	7.0	8.0	2.75	100	62.6	4.39	2.41	36.3	6.64	17.49	6.28	27.85
40	5.0	18.0	1.31	100	76.8	1.70	0.24	14.5	1.62	4.26	4.50	9.48
	7.0	13.0	4.07	50	51.8	3.93	0.64	16.9	3.78	9.94	6.28	15.83
50	6.0	12.0	1.62	50	40.3	2.01	0.93	52.4	1.77	4.65	5.39	8.62
	5.0	18.0	2.85	50	47.9	2.97	1.24	47.4	2.61	6.87	4.50	15.26
60	5.0	16.0	0.44	100	18.5	2.37	1.32	100	1.32	1.32	3.85	3.43
	4.0	11.0	0.12	200	12.5	1.92	1.10	100	1.10	1.10	3.08	3.57
70	6.0	12.0	3.11	50	43.1	3.61	1.64	100	1.64	1.64	4.60	3.56
	4.0	16.5	1.85	100	83.4	2.22	0.98	100	0.98	0.98	3.08	3.18
80	5.0	11.5	1.94	50	50.9	1.90	1.09	100	1.09	1.09	3.85	2.83
	7.0	17.0	2.51	50	48.8	2.57	1.48	100	1.48	1.48	5.39	2.74
85	6.0	11.0	0.22	50	43.5	0.25	0.16	100	0.16	0.16	4.60	0.34
	7.0	12.0	1.16	50	52.5	1.10	0.69	100	0.69	0.69	5.39	1.28

TABLE IV

FORMATION CROSS-SECTIONS OF ^{139}Ba (INDEPENDENT) AND ^{139}Cs (CUMULATIVE)

E_p	D_B^s	D_M^∞	$(S.D.)_T$	$\frac{\lambda_B}{F} \times 10^{32}$	K_1	K_2	σ mb	
							^{139}Ba	^{139}Cs
MeV	d.p.m. x 10^{-7}	d.p.m. x 10^{-8}	mg/cm^2					
20	1.61	9.99	47.61	1.35	2.68	4.55	11.0 ± 1.4	25.5 ± 3.2
	2.39	10.14	46.09	1.33	4.37	6.17		
30	2.83	22.58	48.07	1.91	2.93	4.48	16.4 ± 2.0	25.4 ± 3.2
	4.39	27.85	44.89	2.20	3.73	6.37		
40	1.70	9.48	50.00	1.23	3.50	4.23	19.1 ± 2.4	16.6 ± 2.1
	3.93	15.83	50.00	2.05	4.50	6.12		
50	2.01	8.62	46.34	1.29	3.70	5.31	20.2 ± 2.5	13.1 ± 1.6
	2.97	15.26	45.86	2.26	3.50	4.23		
60	2.37	3.43	46.10*	1.80	3.37	4.30	18.9 ± 1.9	14.9 ± 1.5
	1.92	3.57	46.10*	1.88	2.30	3.60		
70	3.61	3.56	44.27	2.87	3.70	5.31	16.6 ± 1.7	10.1 ± 1.0
	2.22	3.18	45.28	2.62	2.70	3.44		
80	1.90	2.83	45.97	2.26	2.98	4.46	13.1 ± 1.3	8.7 ± 0.9
	2.57	2.74	45.04	2.14	4.88	5.92		
85	0.25	0.34	47.23	0.28	3.58	5.35	12.0 ± 1.2	7.5 ± 0.8
	1.10	1.28	47.23	1.03	4.38	6.17		

*$(S.D.)_M$ = 9.36 mg/cm^2 (Al-foil). For all other irradiations $(S.D.)_M$ is as stated in Section II-A, i.e. $(S.D.)_{Al}$ = 5.29 mg/cm^2, and $(S.D.)_{Cu}$ = 10.53 mg/cm^2.

TABLE V

DISINTEGRATION RATE DATA FOR ^{141}La - ^{141}Ce PAIR

E_p MeV	t_o Min.	t Min.	$C.R._B^s$ c.p.m. x 10^{-4}	$(C.Y.)_B$ %	N_B^s c.p.m. x 10^{-4}	D_B^s d.p.m. x 10^{-4}	$C.R._M^o$ c.p.m. x 10^{-6}	$(C.Y.)_M$ %	N_M^o c.p.m. x 10^{-6}	D_M^o d.p.m. x 10^{-6}	$(1-e^{-\lambda_M t_o})$ x 10^{-3}	D_M^∞ d.p.m. x 10^{-8}
20	13	59	2.46	60.5	4.07	8.31	5.93	48.6	12.22	32.15	11.67	27.55
		2880	2.69	13.0	20.68	42.25						
30	13	58	0.66	42.0	1.58	3.23	5.61	68.4	8.19	21.56	11.67	18.48
		2880	3.45	43.2	7.99	16.32						
40	10	64	1.12	76.0	1.48	3.01	0.31	6.1	5.01	13.20	8.98	14.70
		2880	2.51	36.7	6.85	14.00						
50	10	61	0.93	71.6	1.30	2.65	1.16	30.0	3.86	10.15	8.98	11.31
		2880	3.26	55.1	5.92	12.10						
60	10	73	1.13	45.1	2.50	5.10	2.71	100	2.71	2.71	7.67	3.54
		2880	1.24	13.0	9.50	19.39						
70	10	75.5	0.15	6.4	2.41	4.91	2.78	100	2.78	2.78	7.67	3.63
		2880	2.04	25.1	8.11	16.57						
80	10	71	1.55	51.3	3.02	6.16	2.90	100	2.90	2.90	7.67	3.79
		2880	4.31	62.8	6.86	14.00						
85	13	77	1.41	37.3	3.79	7.74	4.14	100	4.14	4.14	9.96	4.16
		2880	2.18	23.0	9.50	19.40						

TABLE VI

FORMATION CROSS-SECTIONS OF ^{141}Ce (INDEPENDENT) AND ^{141}La (CUMULATIVE)

E_p	D_B^s	D_M^∞	$(S.D.)_T$	$\frac{\lambda_B}{F} \times 10^{29}$	K_1	K_2	σ mb	
MeV	d.p.m. x 10^{-4}	d.p.m. x 10^{-8}	mg/cm^2				^{141}Ce	^{141}La
20	8.31 42.25	27.55	44.56	6.35	2.32 12.52	12.99 12.46	0.7 ± 0.1	52.4 ± 7.3
30	3.23 16.32	18.48	46.15	2.73	2.28 12.52	12.99 12.46	0.9 ± 0.1	46.9 ± 6.6
40	3.01 14.00	14.70	44.19	3.06	1.87 9.63	9.99 9.58	1.2 ± 0.2	46.4 ± 6.5
50	2.65 12.10	11.31	44.72	2.96	1.79 9.63	9.99 9.58	1.6 ± 0.2	40.8 ± 5.7
60	5.10 19.39	3.54	42.23	5.48	2.08 9.63	9.99 9.58	2.1 ± 0.3	34.7 ± 4.2
70	4.91 16.57	3.63	40.60	4.87	2.14 9.63	9.99 9.58	3.2 ± 0.4	32.1 ± 3.8
80	6.16 14.00	3.79	41.94	5.01	2.04 9.63	9.99 9.58	8.0 ± 0.9	21.0 ± 2.5
85	7.74 19.40	4.16	41.67	5.39	2.88 12.52	12.98 12.46	6.0 ± 0.7	22.8 ± 2.7

TABLE VII

DISINTEGRATION RATE DATA FOR ^{143}La - ^{143}Ce PAIR

E_p	t_o	t	$C.R._B^s$	$(C.Y.)_B$	N_B^s	D_B^s	$C.R._M^o$	$(C.Y.)_M$	N_M^o	D_M^o	$(1-e^{-\lambda_M t_o})$	D_M^∞
MeV	Min.	Min.	c.p.m. $\times 10^{-5}$	%	c.p.m. $\times 10^{-6}$	d.p.m. $\times 10^{-6}$	c.p.m. $\times 10^{-5}$	%	c.p.m. $\times 10^{-6}$	d.p.m. $\times 10^{-6}$	$\times 10^{-3}$	d.p.m. $\times 10^{-8}$
20	3.0	12.25	3.99	35.4	1.13	2.90	19.15	56.6	3.38	8.90	2.71	32.80
		160.0	5.40	29.5	1.83	4.71						
30	3.0	13.5	5.43	53.2	1.02	2.63	27.17	70.3	3.86	10.17	2.71	37.52
		161.0	3.16	21.2	1.49	3.84						
40	3.0	14.0	3.28	33.6	0.97	2.51	10.40	54.2	1.92	5.05	2.71	18.63
		160.0	7.10	55.5	1.28	3.29						
50	3.0	14.0	1.62	20.1	0.81	2.07	6.45	50.4	1.28	3.37	2.71	12.42
		160.0	5.98	59.2	1.01	2.60						
60	3.0	15.0	1.35	8.8	1.53	3.96	9.60	100	0.96	0.96	2.31	4.15
		160.0	5.80	30.4	1.91	4.92						
70	3.0	13.0	7.13	54.5	1.31	3.36	9.76	100	0.98	0.98	2.31	4.23
		160.0	3.30	20.1	1.64	4.22						
80	3.0	13.0	1.14	10.5	1.09	2.79	13.81	100	1.38	1.38	2.31	5.98
		160.0	7.18	50.4	1.42	3.67						
85	3.0	13.0	8.19	92.4	0.89	2.28	9.70	100	0.97	0.97	2.31	4.20
		160.0	7.47	68.1	1.10	2.82						

TABLE VIII

FORMATION CROSS-SECTIONS OF ^{143}Ce (INDEPENDENT) AND ^{143}La (CUMULATIVE)

E_p	D_B^s	D_M^∞	$(S.D.)_T$	$\frac{\lambda_B}{F} \times 10^{31}$	K_1	K_2'	σ mb	
MeV	d.p.m. x 10^{-6}	d.p.m. x 10^{-8}	mg/cm^2				^{143}Ce	^{143}La
20	2.90 4.71	32.80	144.27	5.79	1.48 2.86	2.99 2.84	5.3 ± 0.7	23.2 ± 3.2
30	2.63 3.84	37.52	152.54	4.33	1.57 2.85	2.99 2.84	8.4 ± 1.1	22.7 ± 3.2
40	2.51 3.29	18.63	156.43	3.24	1.60 2.86	2.98 2.84	14.4 ± 1.9	21.3 ± 3.0
50	2.07 2.60	12.42	149.71	2.57	1.60 2.86	2.98 2.84	17.2 ± 2.2	18.3 ± 2.5
60	3.96 4.92	4.15	149.72	5.38	1.67 2.86	2.98 2.84	15.6 ± 1.7	16.9 ± 2.0
70	3.36 4.22	4.23	153.23	5.06	1.53 2.86	2.99 2.84	14.9 ± 1.6	14.3 ± 1.7
80	2.79 3.67	5.98	145.87	6.51	1.53 2.86	2.99 2.84	8.6 ± 0.9	11.2 ± 1.3
85	2.28 2.82	4.20	151.36	4.67	1.53 2.86	2.99 2.84	11.2 ± 1.2	10.0 ± 1.1

TABLE IX

FORMATION CROSS-SECTIONS OF ^{139}Ce

E_p (MeV)		70	80	85
t_o	(hour)	1	1	1
t^*	(hour)	7002	7002	7144
N_γ	(c.p.m.)	99.6	389.1	653.7
C.Y.(^{139}Ce)	(%)	29.3	78.8	73.7
N_γ^t	(c.p.m.)	339.9	493.6	887.0
$D^o(^{139}Ce)$	(d.p.m.)	1789	2610	4826
$(1-e^{-\lambda_{139Ce} t_o})$		2.0×10^{-4}	2.0×10^{-4}	2.0×10^{-4}
$D^\infty(^{139}Ce)$	(d.p.m.)	8.99×10^6	1.30×10^7	2.41×10^7
C.R.$^o(^{24}Na)$	(c.p.m.)	1.12×10^7	1.04×10^7	1.47×10^7
$D^o(^{24}Na)$	(c.p.m.)	1.12×10^7	1.04×10^7	1.47×10^7
$(1-e^{-\lambda_{24Na} t_o})$		4.50×10^{-2}	4.50×10^{-2}	4.50×10^{-2}
$D^\infty(^{24}Na)$	(d.p.m.)	2.49×10^8	2.31×10^8	3.26×10^8
$(S.D.)_T$	(mg/cm^2)	45.69	42.58	43.67
F		3.94×10^{-35}	4.77×10^{-35}	3.35×10^{-35}
σ (^{139}Ce)	(mb)	0.35 ± 0.05	0.62 ± 0.09	0.81 ± 0.12

*t = time interval between the end of bombardment and the time of actual measurement of ^{139}Ce activity.

TABLE X

DISINTEGRATION RATE DATA FOR ^{141}Ba*

E_p	t_o	t_s** (^{141}Ba)	C.R.^{s} (^{141}Ce at t_s)	A.F.	$(C.Y.)_{^{141}Ce}$	$N^s_{^{141}Ce}$	$D^s_{^{141}Ce}$	$(C.Y.)_{^{141}Ba}$	$D^o_{^{141}Ba}$	$(1-e^{-\lambda_{^{141}Ba} t_o})$	$D^\infty_{^{141}Ba}$
MeV	Min.	Min.	c.p.m.		%	c.p.m. x 10^{-4}	d.p.m. x 10^{-4}	%	d.p.m. x 10^{-8}		d.p.m. x 10^{-8}
20	13	13.0	6367	1.25	10.7	7.44	15.19	88.5	7.36	0.394	18.69
30	13	9.0	11918	1.25	52.9	2.82	5.75	88.2	2.40	0.394	6.08
40	10	9.0	4367	1.25	26.5	2.06	4.21	87.2	1.77	0.319	5.55
50	10	10.5	6837	1.25	73.7	1.16	2.37	84.2	1.09	0.319	3.43
60	10	7.0	7245	1.25	37.2	2.43	4.97	86.8	1.95	0.319	6.09
70	10	6.75	4326	1.25	26.0	2.08	4.25	87.5	1.63	0.319	5.11
80	10	7.0	1518	1.25	15.3	1.24	2.53	86.8	0.99	0.319	3.10
85	13	8.0	2959	1.25	25.3	1.46	2.99	85.2	1.24	0.394	3.14

*Disintegration rate data for monitor are the same as given in Table V.

**t_s = time interval between the end of bombardment and the time of ^{141}Ba separation as barium chloride.

TABLE XI

CUMULATIVE FORMATION CROSS-SECTIONS OF ^{141}Ba

E_p	$D^{\infty}_{^{141}Ba}$	D^{∞}_{M}	$(S.D.)_T$	$F \times 10^{-35}$	σ mb
MeV	d.p.m. x 10^{-8}	d.p.m. x 10^{-8}	mg/cm^2		
20	18.69	27.55	44.56	2.33	43.5 $\pm$ 6.1
30	6.08	18.48	46.15	5.42	33.0 $\pm$ 4.6
40	5.55	14.70	44.19	4.84	26.9 $\pm$ 3.8
50	3.43	11.31	44.72	5.00	17.1 $\pm$ 2.4
60	6.09	3.54	42.23	2.70	16.5 $\pm$ 2.3
70	5.11	3.63	40.60	3.04	15.5 $\pm$ 2.2
80	3.10	3.79	41.94	2.95	9.1 $\pm$ 1.3
85	3.14	4.16	41.67	2.75	8.6 $\pm$ 1.2

TABLE XII

INDEPENDENT FORMATION CROSS-SECTIONS OF ^{141}La

E_p MeV	σ^* mb
20	8.9 ± 1.2
30	13.9 ± 1.9
40	19.5 ± 2.7
50	23.6 ± 3.3
60	18.2 ± 2.2
70	16.6 ± 2.0
80	11.9 ± 1.4
85	14.2 ± 1.7

*$\sigma(^{141}La$ Independent) = $\sigma(^{141}La$ Cumulative, Table VI) –
$\sigma(^{141}Ba$ Cumulative, Table XI)

TABLE XIII

INDEPENDENT FORMATION CROSS-SECTIONS OF ^{143}Pr INTERPOLATED FROM CHARGE DISPERSION CURVES

^{143}Pr: N/Z = 1.424

E_p (MeV)	σ (mb)
20	0.4
30	0.5
40	0.7
50	0.9
60	1.2
70	2.9
80	3.4
85	6

FIGURE 19

EXCITATION FUNCTION FOR THE INDEPENDENT FORMATION CROSS-SECTION OF ^{139}Ba

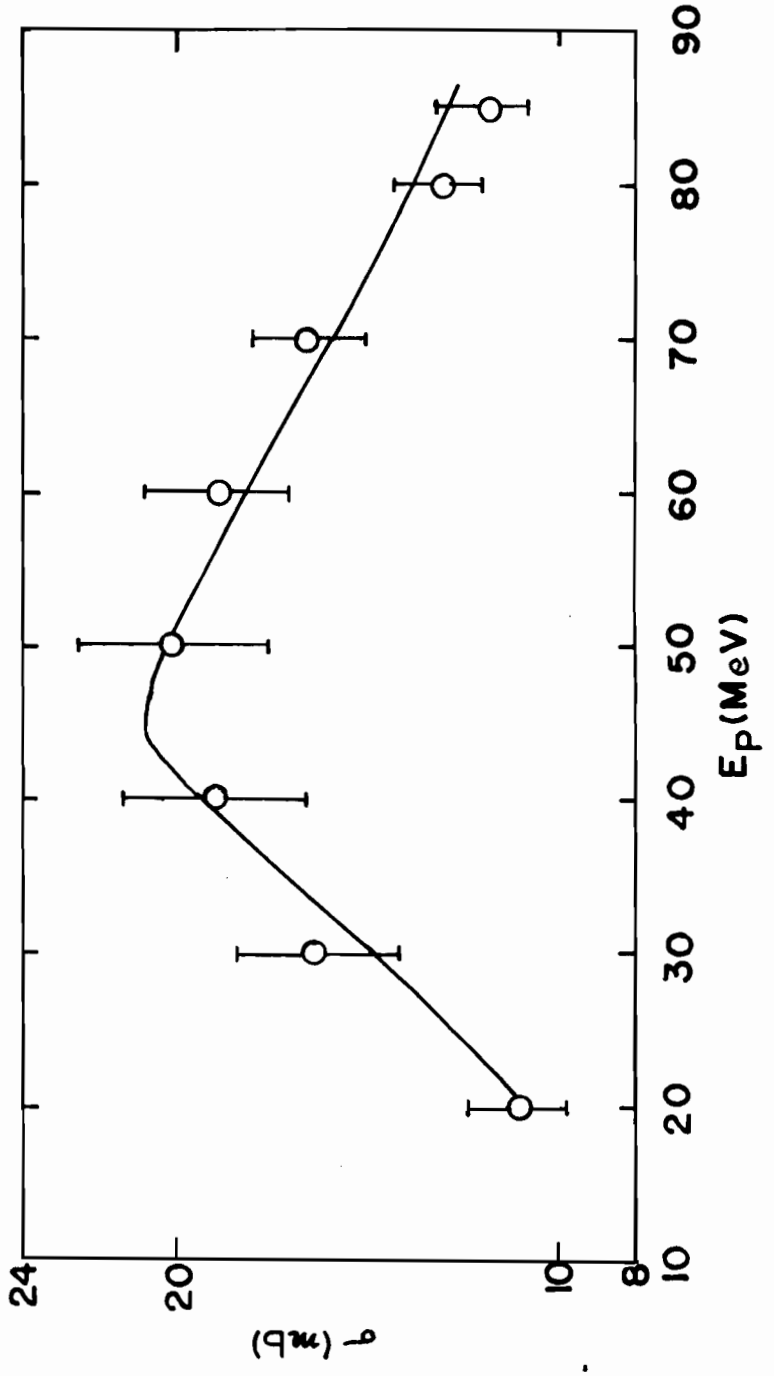
24
20
10
8
10
20
30
40
50
60
70
80
90
σ (mb)
Ep(MeV)

FIGURE 20

EXCITATION FUNCTION FOR THE INDEPENDENT FORMATION CROSS-SECTION OF ^{139}Ce

O - This work

X - Friedlander, Friedman, Gordon, and Yaffe[82]

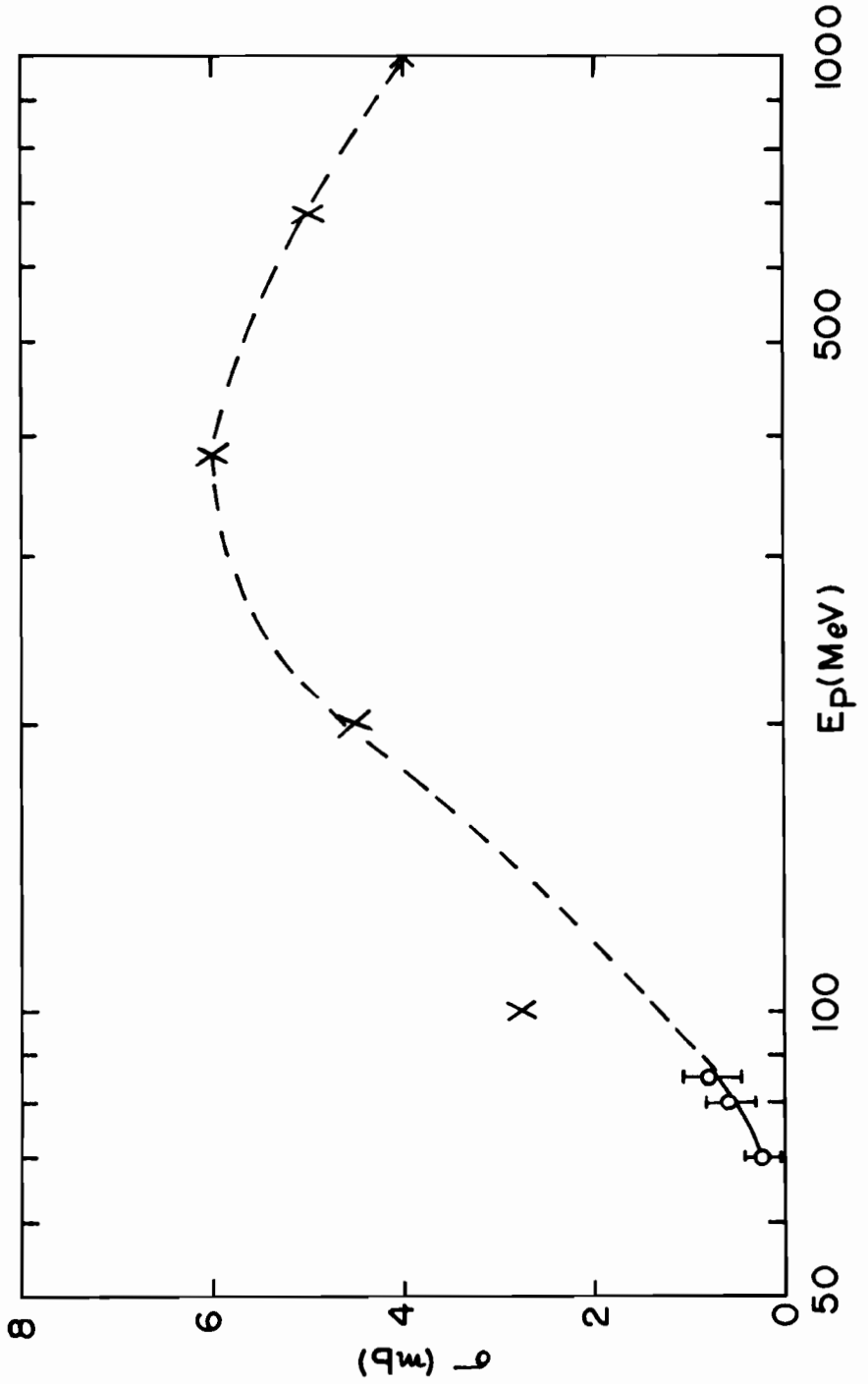
σ (mb)
0
2
4
6
8
50
100
500
1000
Ep(MeV)

FIGURE 21

EXCITATION FUNCTION FOR THE CUMULATIVE FORMATION CROSS-SECTION OF ^{139}Cs

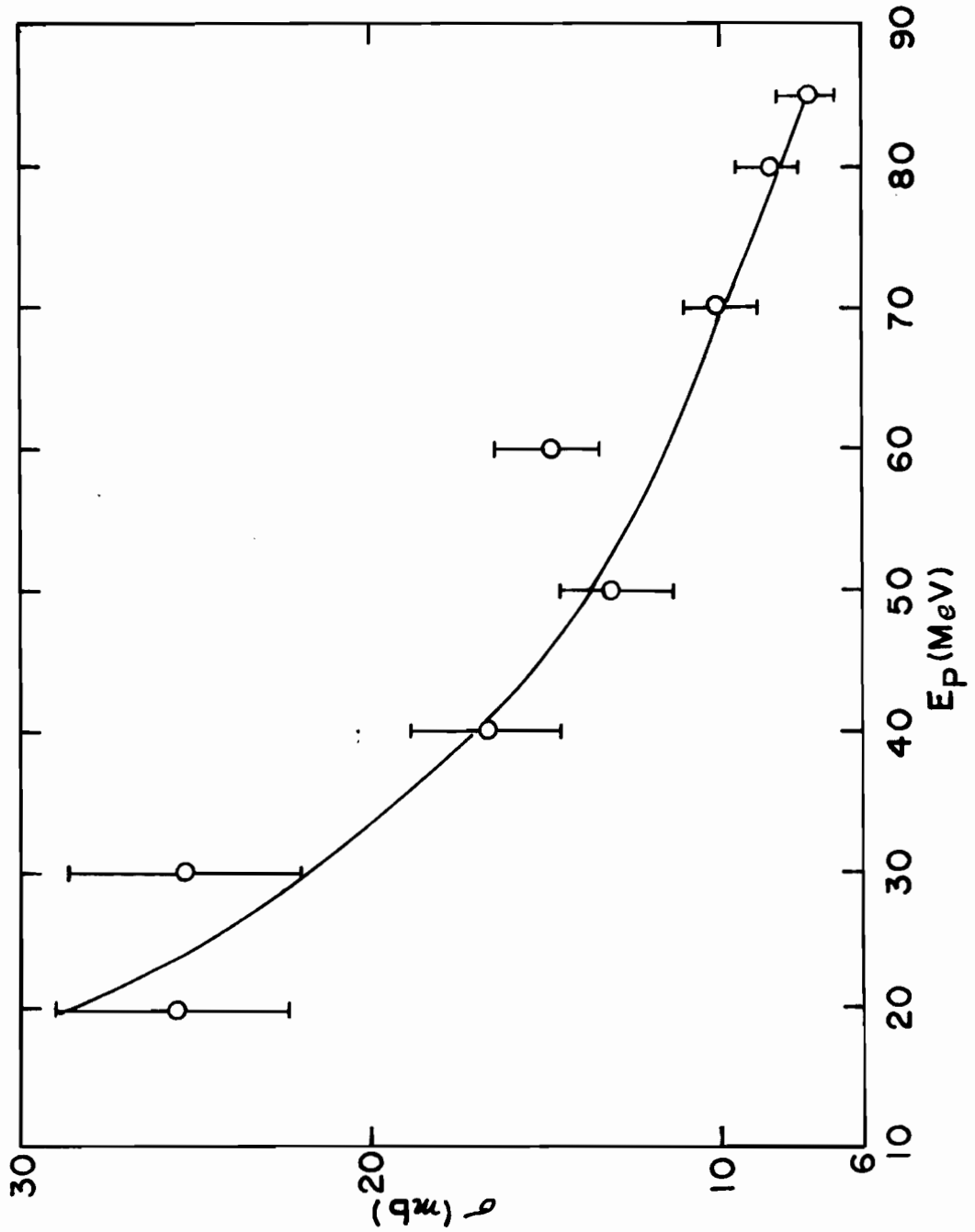
σ (mb)
30
20
10
6
10
20
30
40
50
60
70
80
90
E_p (MeV)

FIGURE 22

EXCITATION FUNCTION FOR THE INDEPENDENT FORMATION CROSS-SECTION OF ^{141}La

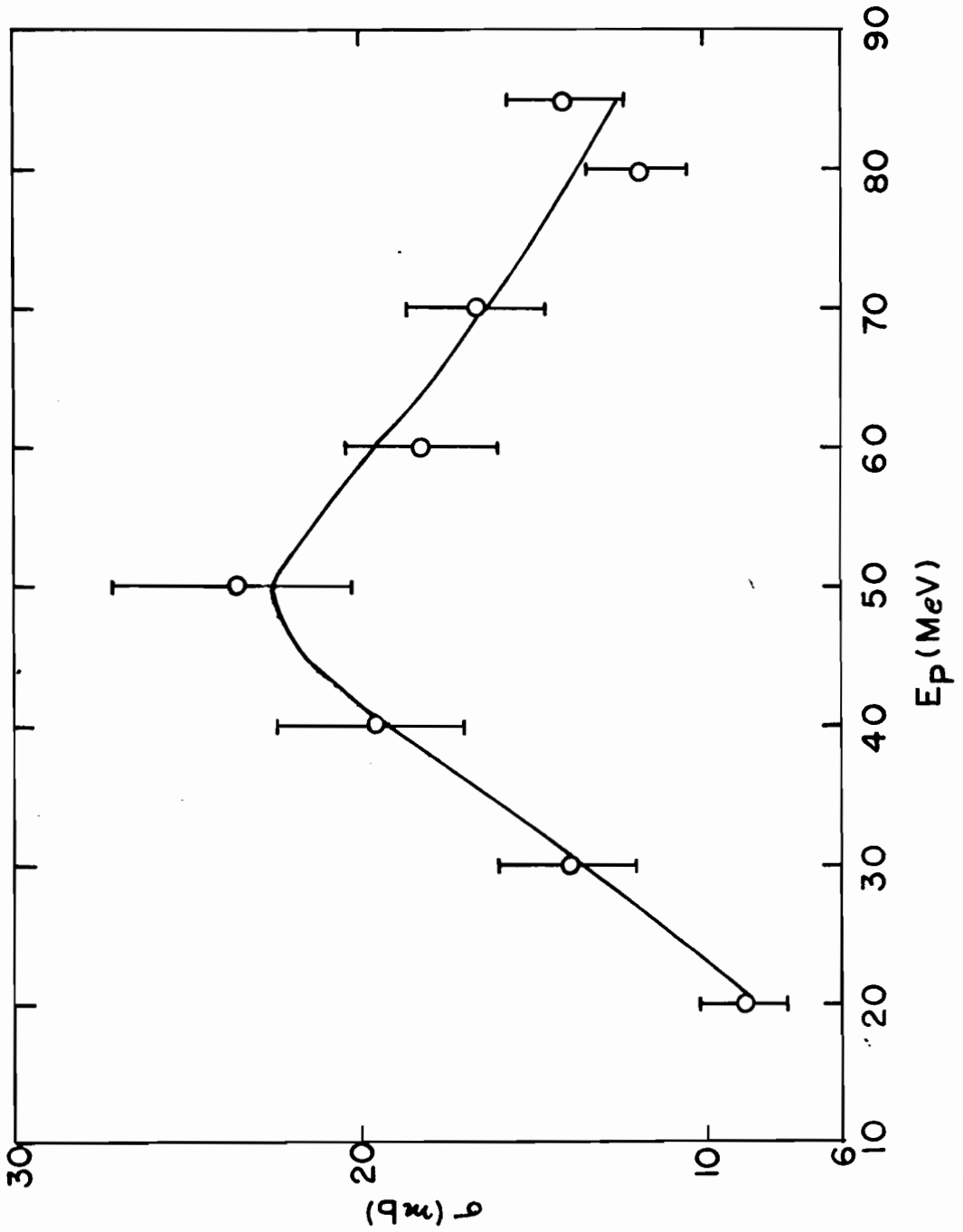
σ (mb)
30
20
10
6
10
20
30
40
50
60
70
80
90
Ep (MeV)

FIGURE 23

EXCITATION FUNCTION FOR THE INDEPENDENT FORMATION CROSS-SECTION OF ^{141}Ce

O - This work

X - Friedlander, Friedman, Gordon, and Yaffe[82]

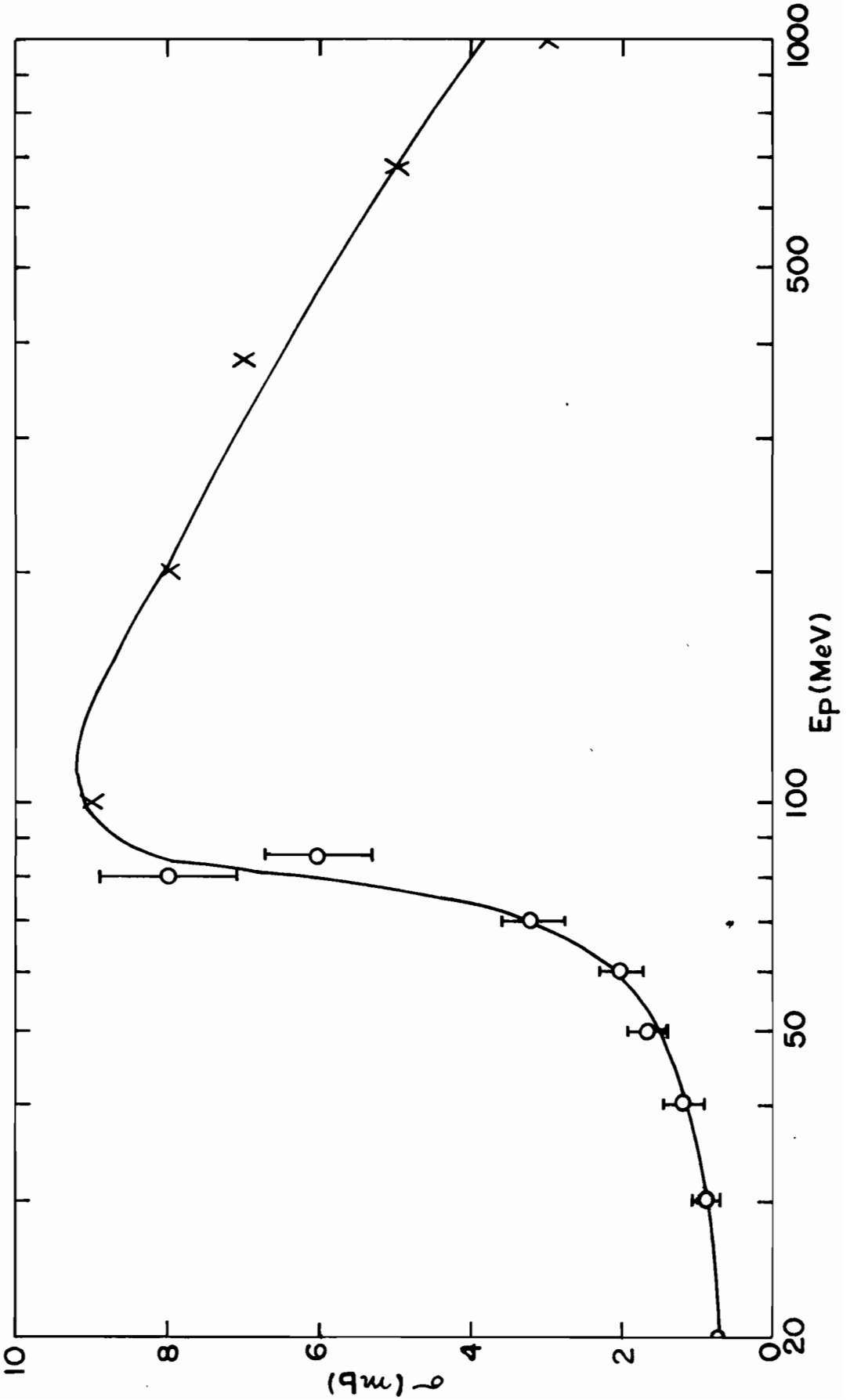
σ (mb)
0
2
4
6
8
10
20
50
100
500
1000
Ep (MeV)

FIGURE 24

EXCITATION FUNCTION FOR THE CUMULATIVE FORMATION CROSS-SECTION OF ^{141}Ba

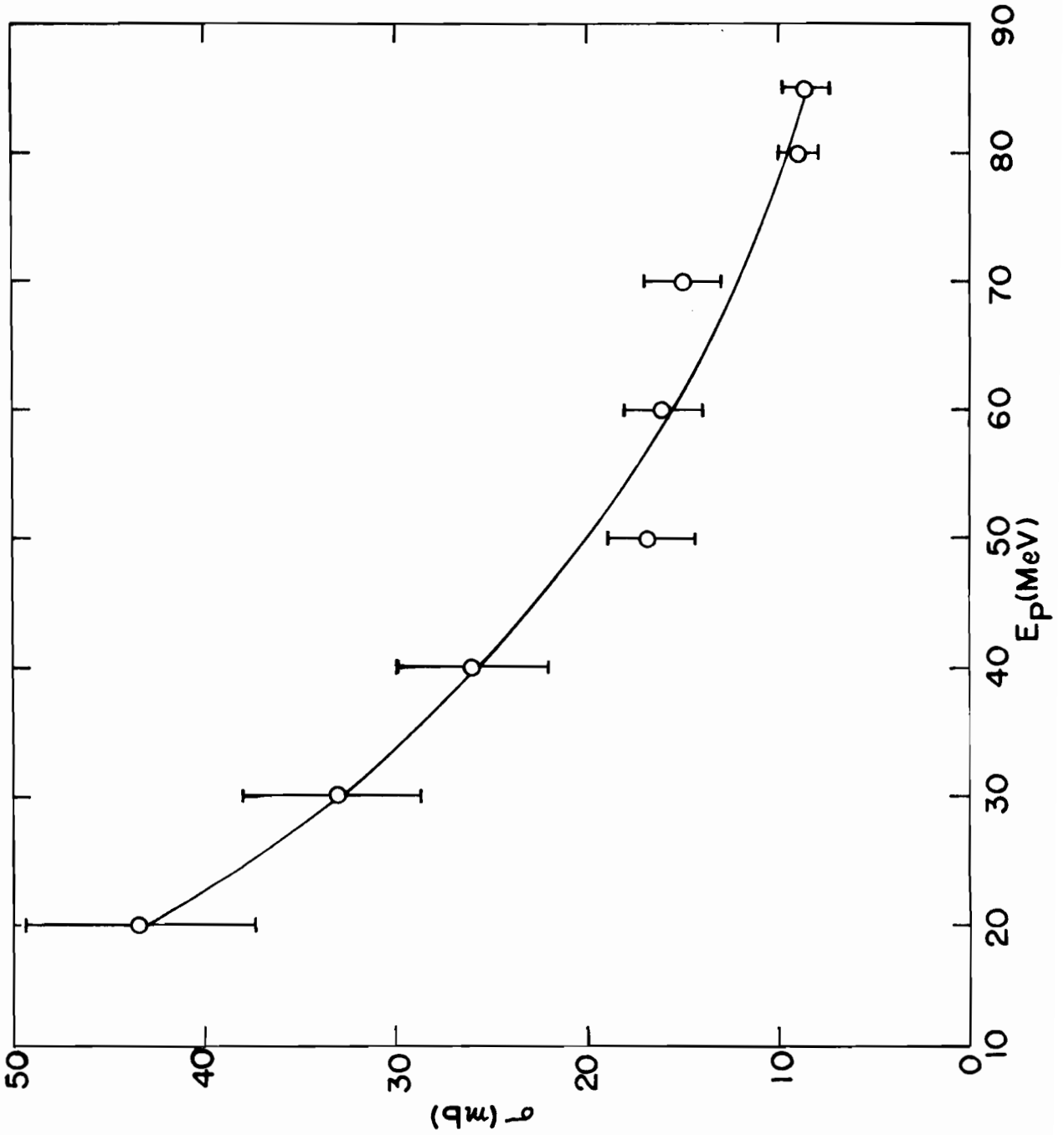
σ (mb)
0
10
20
30
40
50
10
20
30
40
50
60
70
80
90
E_p(MeV)

FIGURE 25

EXCITATION FUNCTION FOR THE INDEPENDENT FORMATION CROSS-SECTION OF ^{143}Ce

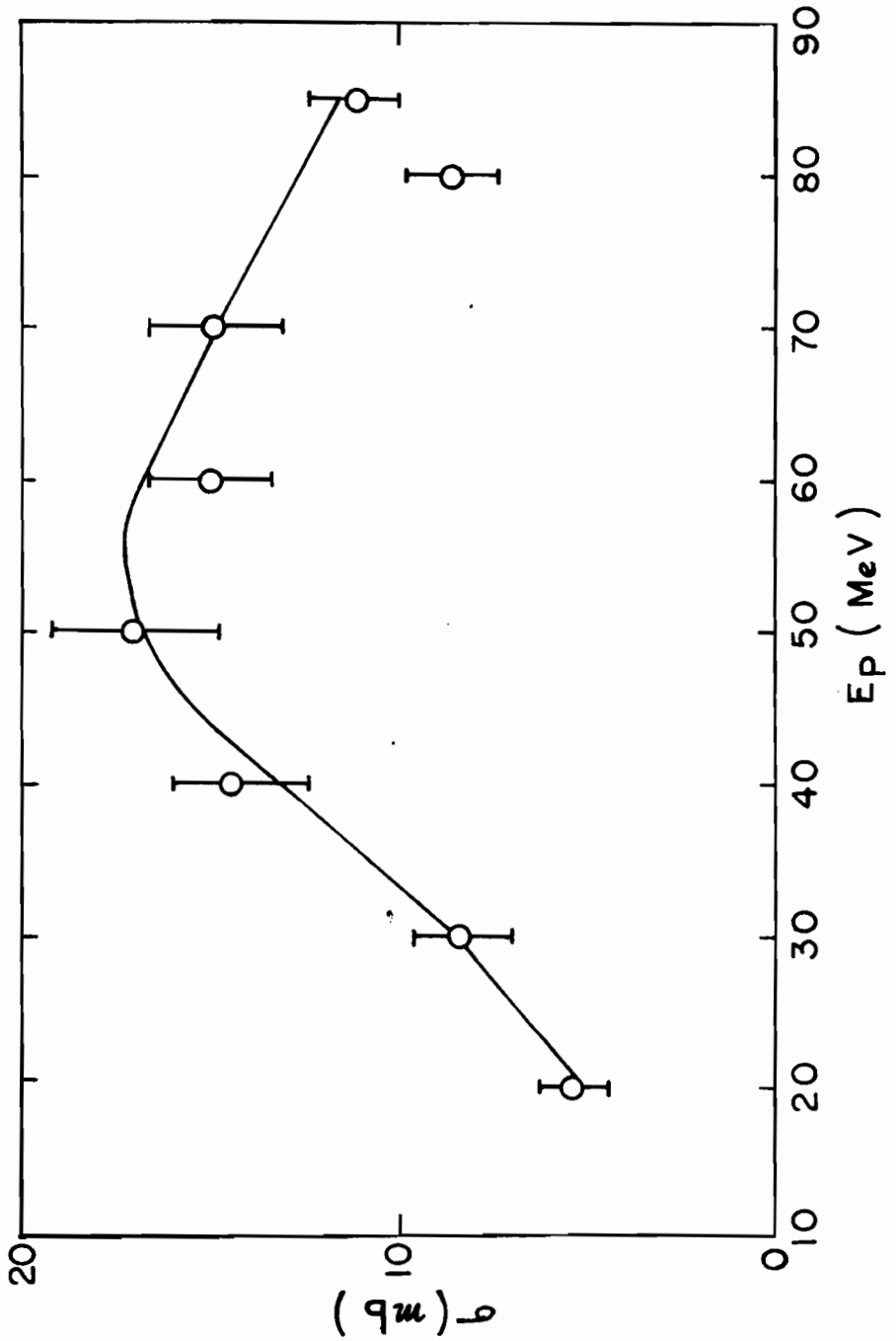
σ (mb)
0
10
20
10
20
30
40
50
60
70
80
90
Ep (MeV)

FIGURE 25

EXCITATION FUNCTION FOR THE CUMULATIVE FORMATION CROSS-SECTION OF ^{143}La

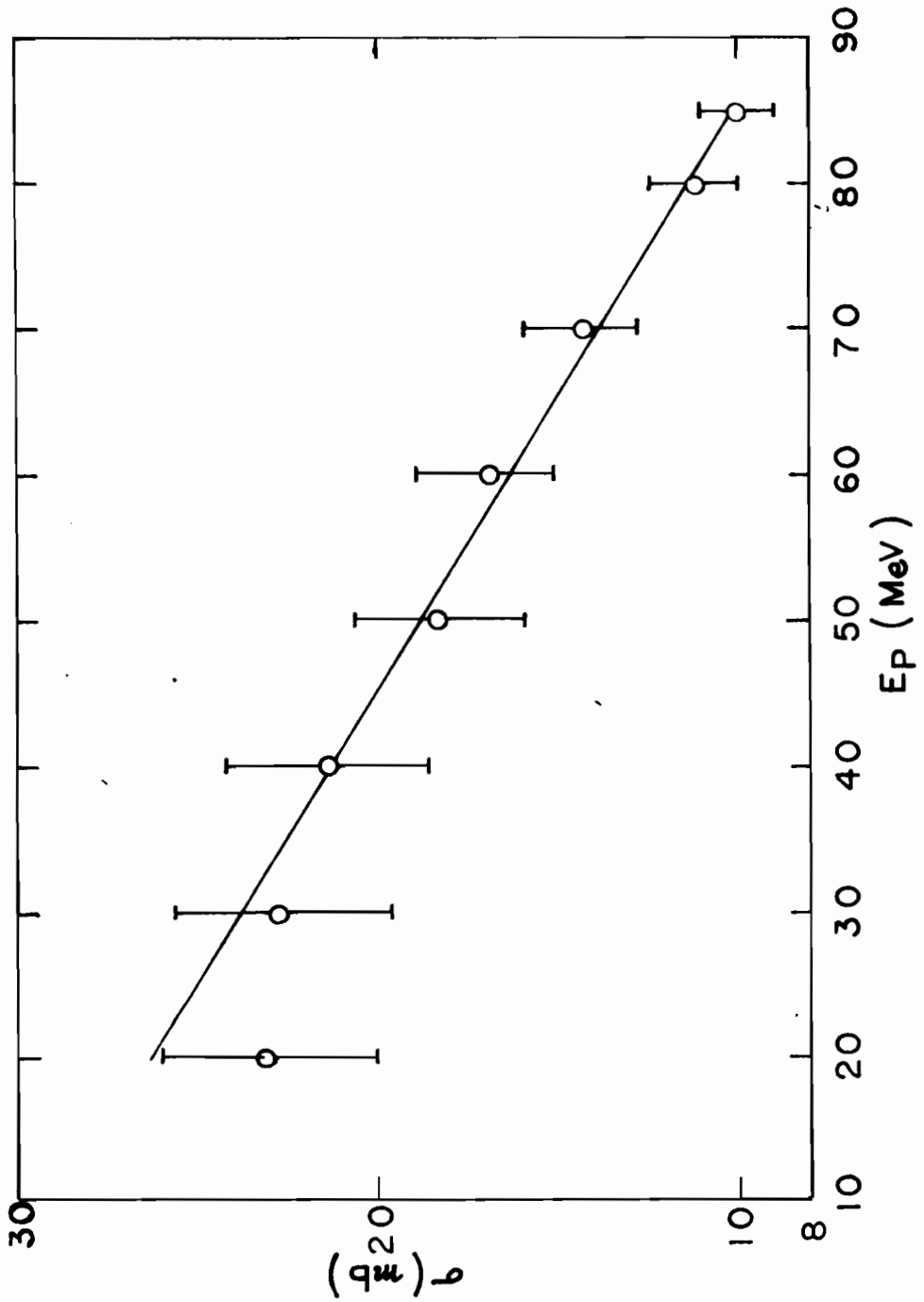
σ (mb)
30
20
10
8
10
20
30
40
50
60
70
80
90
Ep (MeV)

FIGURE 27

EXCITATION FUNCTION FOR THE INDEPENDENT FORMATION CROSS-SECTION OF ^{143}Pr INTERPOLATED FROM CHARGE DISPERSION CURVES

O - This work

X - Friedlander, Friedman, Gordon, and Yaffe[82]

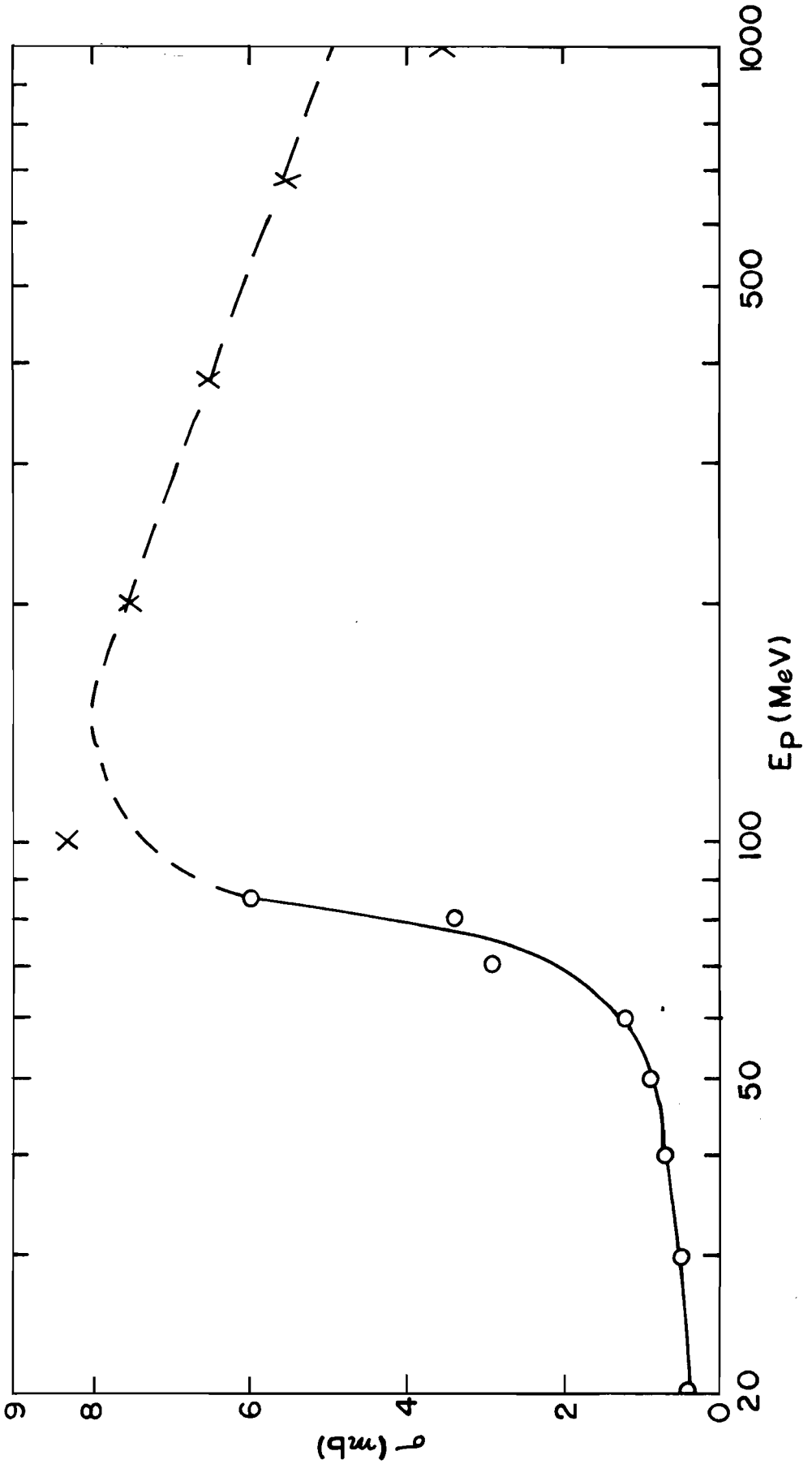
σ (mb)
0
2
4
6
8
9
20
50
100
500
1000
E_p (MeV)

V. DISCUSSION

V-A. GENERAL

The cross-sections for the independent formation of both neutron-excess and neutron-deficient nuclides rise from threshold to a maximum then fall off as the bombarding energy is increased. The peak energies of the excitation functions are given in Table XIV.

TABLE XIV

PEAK ENERGIES OF THE INDEPENDENT FORMATION EXCITATION FUNCTIONS

Nuclide	N/Z	Peak Energy (MeV)
^{139}Ba	1.482	44 ± 6
^{141}La	1.474	50 ± 6
^{143}Ce	1.465_5	55 ± 7
^{141}Ce	1.431	110
^{143}Pr	1.424	145
^{139}Ce	1.396_5	380

As the neutron-to-proton ratio of the fission product decreases, the energy at which the excitation functions peak increases, indicating that nuclides of lower neutron-to-proton,

N/Z, ratios become more prominent as the energy of the bombarding protons becomes larger. This behaviour is also reflected in the cumulative formation cross-sections (Figs. 21, 24,26, Section IV) which are seen to decrease monotonically with increasing energy. These results are in agreement with the findings of Friedlander et al.[82] and Davies and Yaffe[84] among others. Figure 28 is a composite graph of the results from all three studies showing the variation of energies at which the excitation functions peak with neutron-to-proton ratio of the fission product. It can be seen that the present experimental data fit very nicely on the curve, though the nuclides investigated have both the proton number and the neutron number changing. The original curve was constructed mainly from data on cesium isotopes.

The more fundamental role of the neutron-to-proton ratio in determining charge distribution rather than the distance from beta stability is seen from the following. The neutron-excess nuclides, ^{139}Ba and ^{141}Ce, which are both one step away from stability, have widely different independent formation cross-sections and their peak energies vary appreciably. Their neutron-to-proton ratios are 1.482 and 1.431 respectively. On the other hand, ^{143}Pr is also one step away from stability but has a neutron-to-proton ratio of 1.424 close to that of ^{141}Ce (1.431). Its independent formation cross-sections do not vary much from those of ^{141}Ce and the excitation function peaks at approximately the same energy as

FIGURE 28

ENERGIES AT WHICH THE EXCITATION FUNCTIONS REACH THEIR MAXIMA

(Plotted as a function of N/Z)

O - This work

● - Friedlander, Friedman, Gordon, and Yaffe[82]

□ - Davies and Yaffe[84]

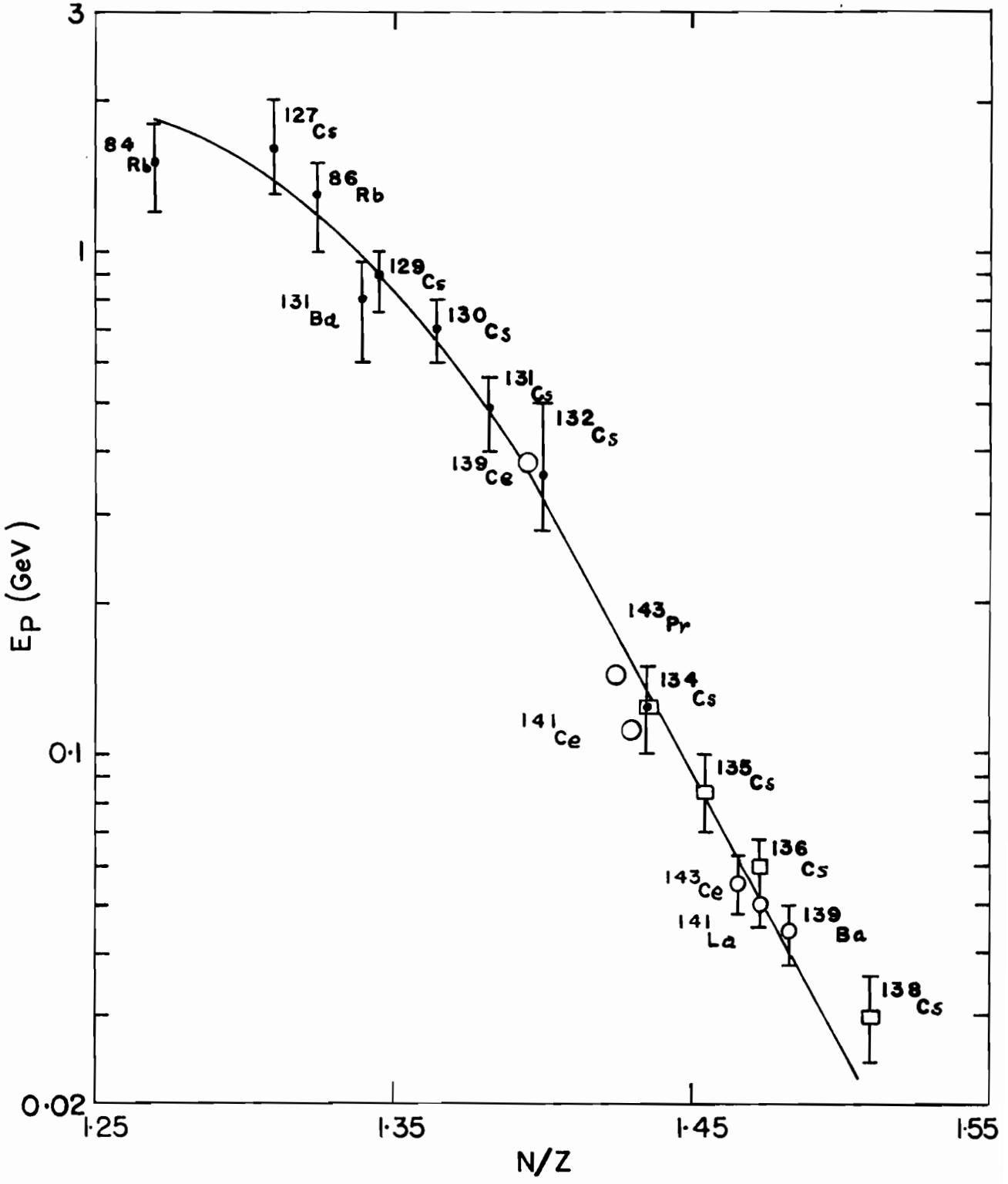
3
1
0·1
0·02
E_P (GeV)
1·25
1·35
1·45
1·55
N/Z
84 Rb
127 Cs
86 Rb
129 Cs
131 Ba
130 Cs
131 Cs
132 Cs
139 Ce
143 Pr
134 Cs
141 Ce
135 Cs
136 Cs
143 Ce
141 La
139 Ba
138 Cs

that of ^{141}Ce. It is also worth noting that ^{139}Ce, a neutron-deficient nuclide with neutron-to-proton ratio of 1.397, is also one step away from stability, but its formation cross-sections are very much smaller than either of the other three nuclides and its excitation function reaches a maximum value in the neighbourhood of 380 MeV. From these it seems to indicate that the neutron-to-proton ratio can be considered as a fundamental parameter and the empirical curve in Fig. 28 may be useful for the correlation of other fission data.

V-B. NUCLEAR CHARGE DISPERSION

Nuclear charge dispersion curves were constructed at each bombarding energy from the cross-section data. These curves are shown in Figs. 29 to 36 inclusive. On these curves the independent formation cross-sections are plotted versus neutron-to-proton ratio rather than $Z - Z_A$ to avoid the difficulties in determining the most stable charge, Z_A, at the 82 neutron shell-edge. The assumptions made in drawing nuclear charge dispersion curves are that the curve for a particular energy applies to all masses in the range $139 \leq A \leq 143$, which implies that the mass distribution curve is essentially flat in this mass region and that the curves are symmetrical. In addition to the constraint of symmetry, the right-hand portion of each curve is drawn so that the cumulative yields determined from the charge dispersion curve agreed as closely as possible with the experimental cumulative yields for the nuclides ^{139}Cs, ^{141}Ba, and ^{143}La. Friedlander et al.[82] have shown that this

FIGURE 29

CHARGE DISPERSION AT 20 MeV

[The right-hand (dashed) portion of the curve has been drawn so that the sums of the isobaric yields read off the curve approximate the experimental cumulative yields]

	σ(mb) Experimental	σ(mb) Curve
^{139}Cs	29	33
^{141}Ba	43	37.5
^{143}La	26	40

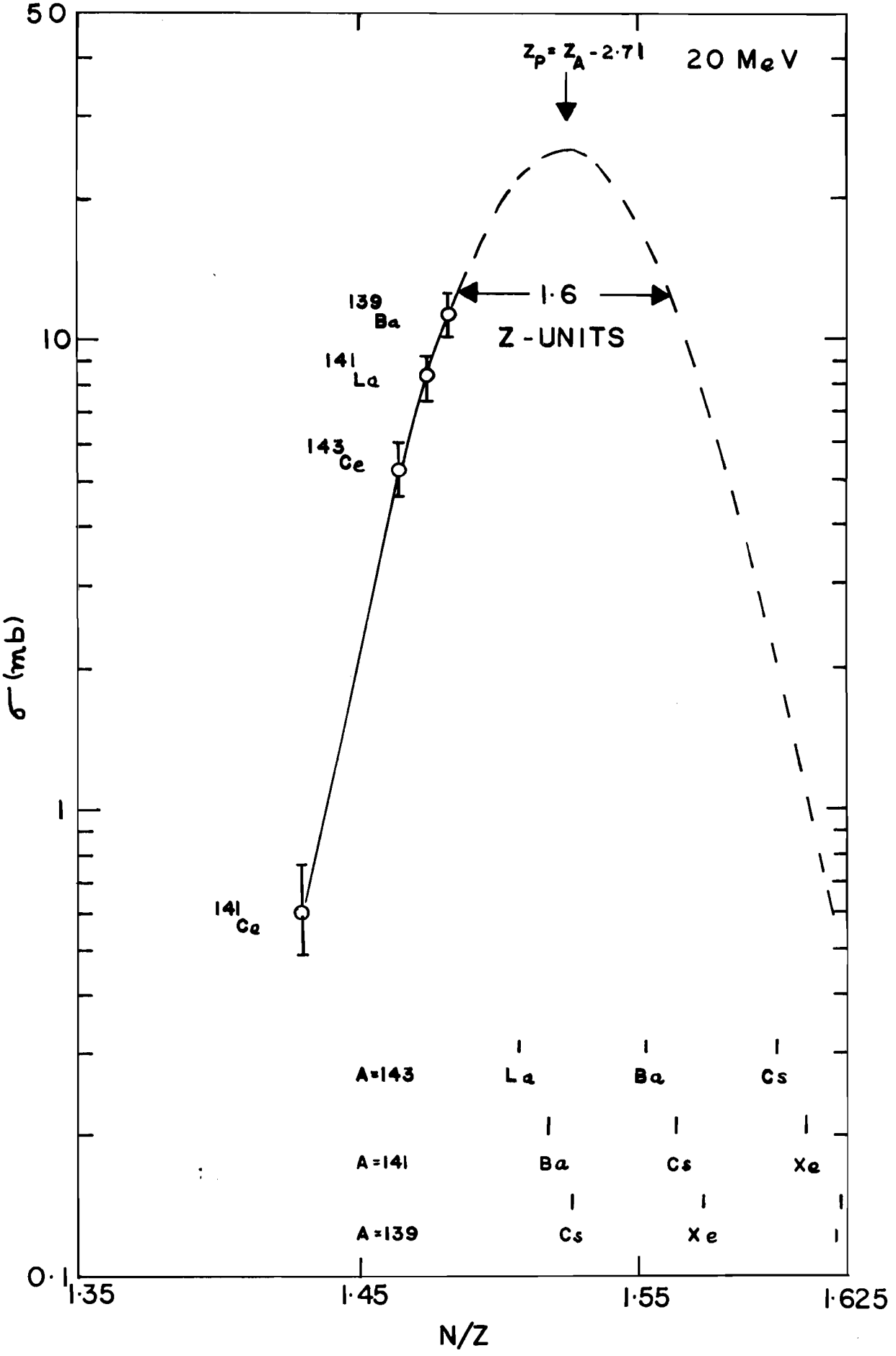
50
10
1
0·1
σ (mb)
$Z_p = Z_A - 2·71$
20 MeV
1·6
Z-UNITS
139 Ba
141 La
143 Ce
141 Ce
A=143
A=141
A=139
La
Ba
Cs
Xe
1·35
1·45
1·55
1·625
N/Z

FIGURE 30

CHARGE DISPERSION AT 30 MeV

[The right-hand (dashed) portion of the curve has been drawn so that the sums of the isobaric yields read off the curve approximate the experimental cumulative yields]

	σ(mb) Experimental	σ(mb) Curve
^{139}Cs	22	23
^{141}Ba	33	28
^{143}La	24	33

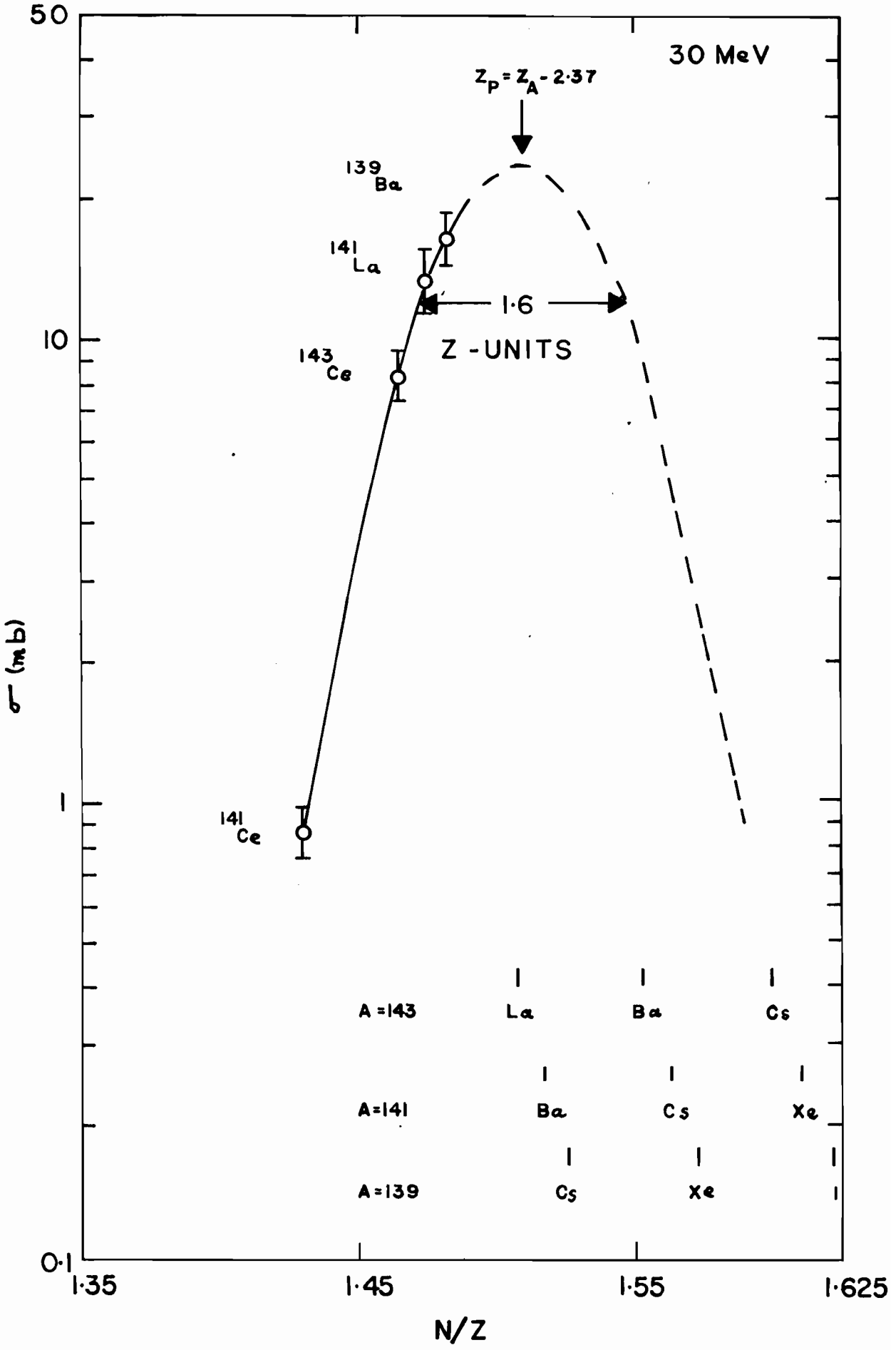
50
10
1
0·1
30 MeV
$Z_P = Z_A - 2{\cdot}37$
139 Ba
141 La
143 Ce
141 Ce
1·6
Z - UNITS
σ (mb)
A=143
La
Ba
Cs
A=141
Ba
Cs
Xe
A=139
Cs
Xe
1·35
1·45
1·55
1·625
N/Z

FIGURE 31

CHARGE DISPERSION AT 40 MeV

[The right-hand (dashed) portion of the curve has been drawn so that the sums of the isobaric yields read off the curve approximate the experimental cumulative yields]

	σ(mb) Experimental	σ(mb) Curve
^{139}Cs	17	16.5
^{141}Ba	26	21
^{143}La	21	25.4

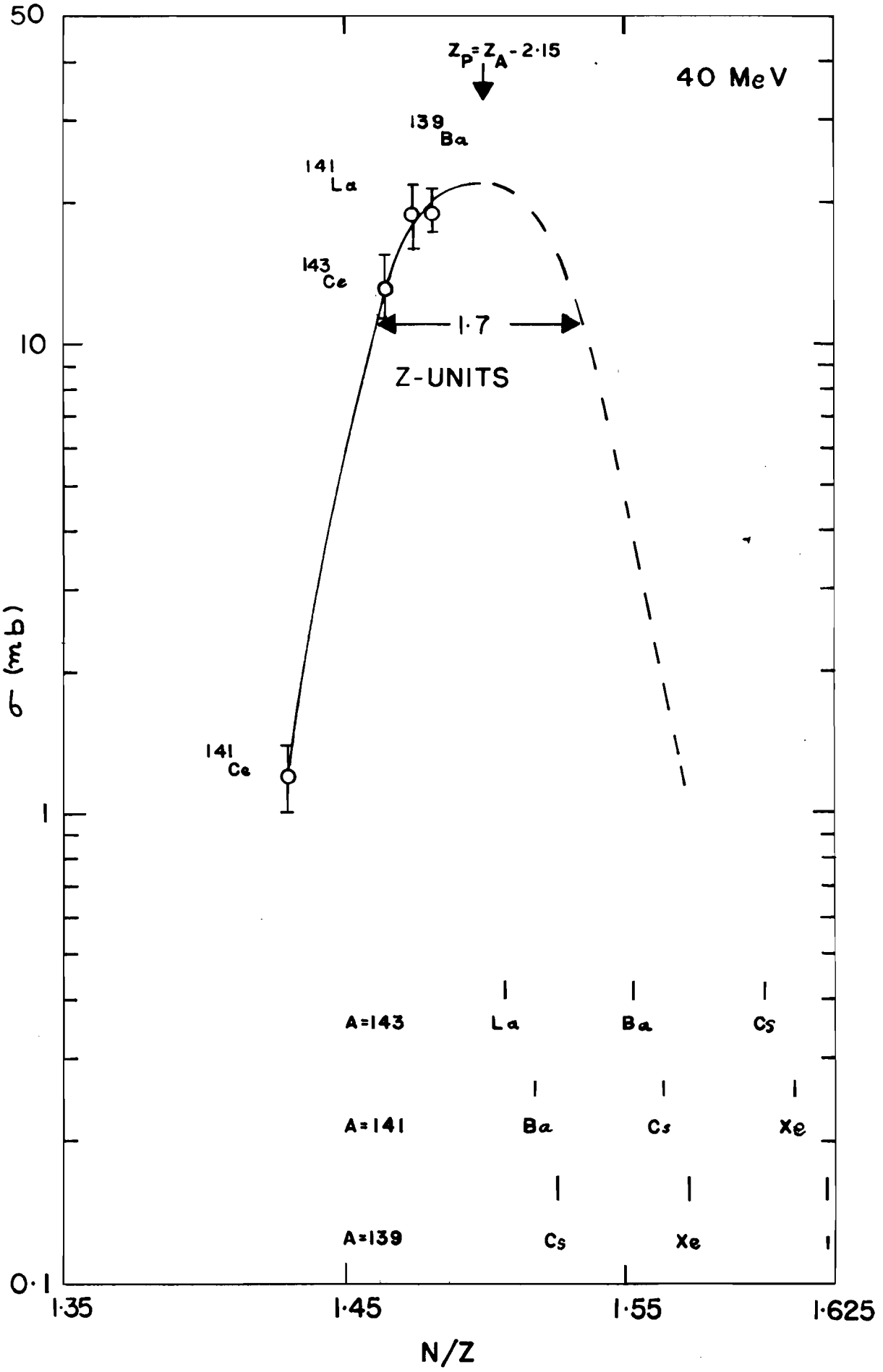
50
10
1
0·1
σ (mb)
$Z_P = Z_A - 2·15$
40 MeV
139 Ba
141 La
143 Ce
141 Ce
1·7
Z-UNITS
A=143
La
Ba
Cs
A=141
Ba
Cs
Xe
A=139
Cs
Xe
I
1·35
1·45
1·55
1·625
N/Z

FIGURE 32

CHARGE DISPERSION AT 50 MeV

[The right-hand (dashed) portion of the curve has been drawn so that the sums of the isobaric yields read off the curve approximate the experimental cumulative yields]

	σ(mb) Experimental	σ(mb) Curve
^{139}Cs	14	15
^{141}Ba	20	20
^{143}La	19	24

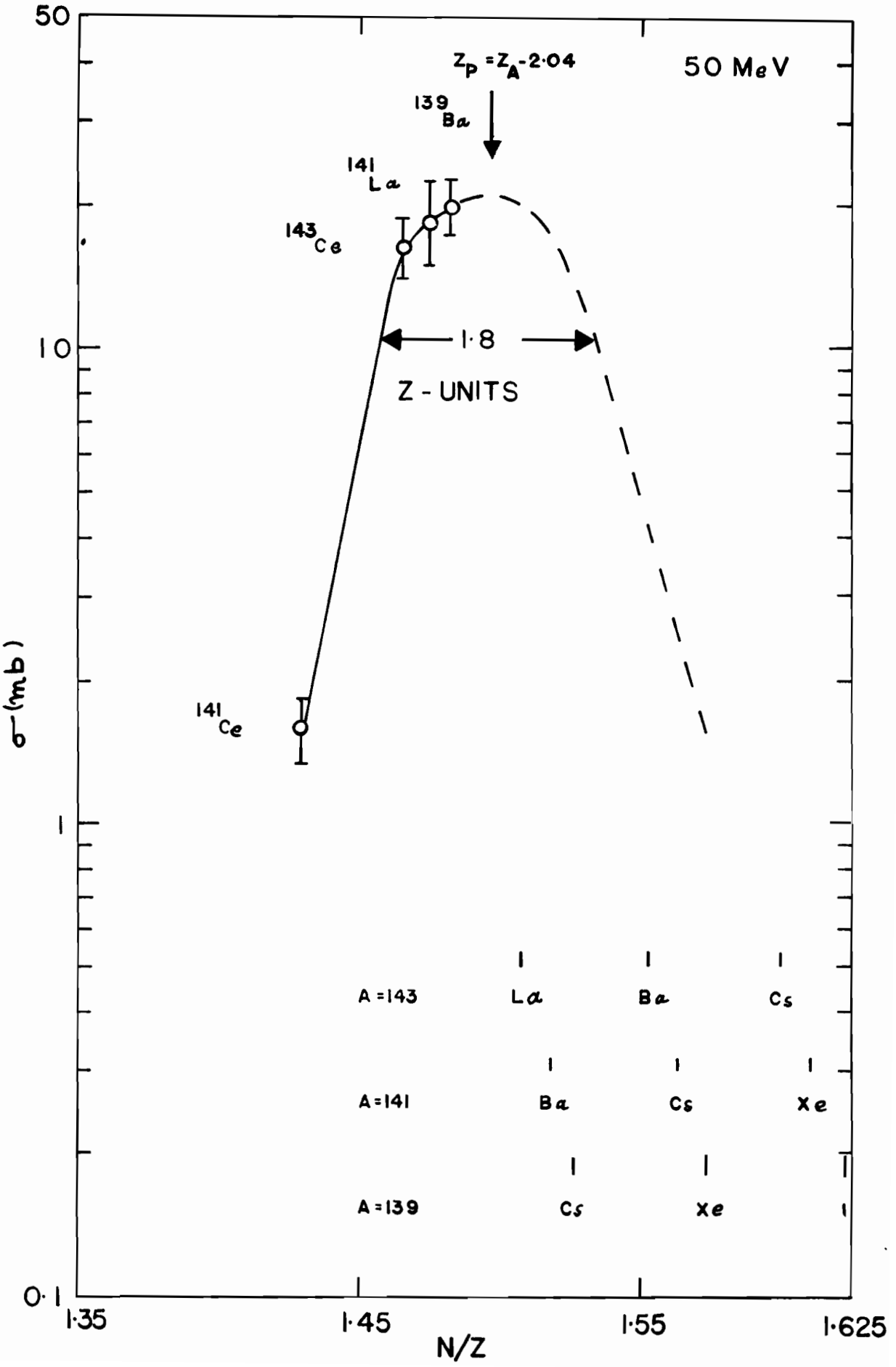
50
10
1
0·1
σ (mb)
$Z_P = Z_A - 2·04$
50 MeV
139 Ba
141 La
143 Ce
141 Ce
1·8
Z - UNITS
A = 143
La
Ba
Cs
A = 141
Ba
Cs
Xe
A = 139
Cs
Xe
1·35
1·45
1·55
1·625
N/Z

FIGURE 33

CHARGE DISPERSION AT 60 MeV

[The right-hand (dashed) portion of the curve has been drawn so that the sums of the isobaric yields read off the curve approximate the experimental cumulative yields]

	σ(mb) Experimental	σ(mb) Curve
^{139}Cs	12	12
^{141}Ba	16	16.5
^{143}La	17	19

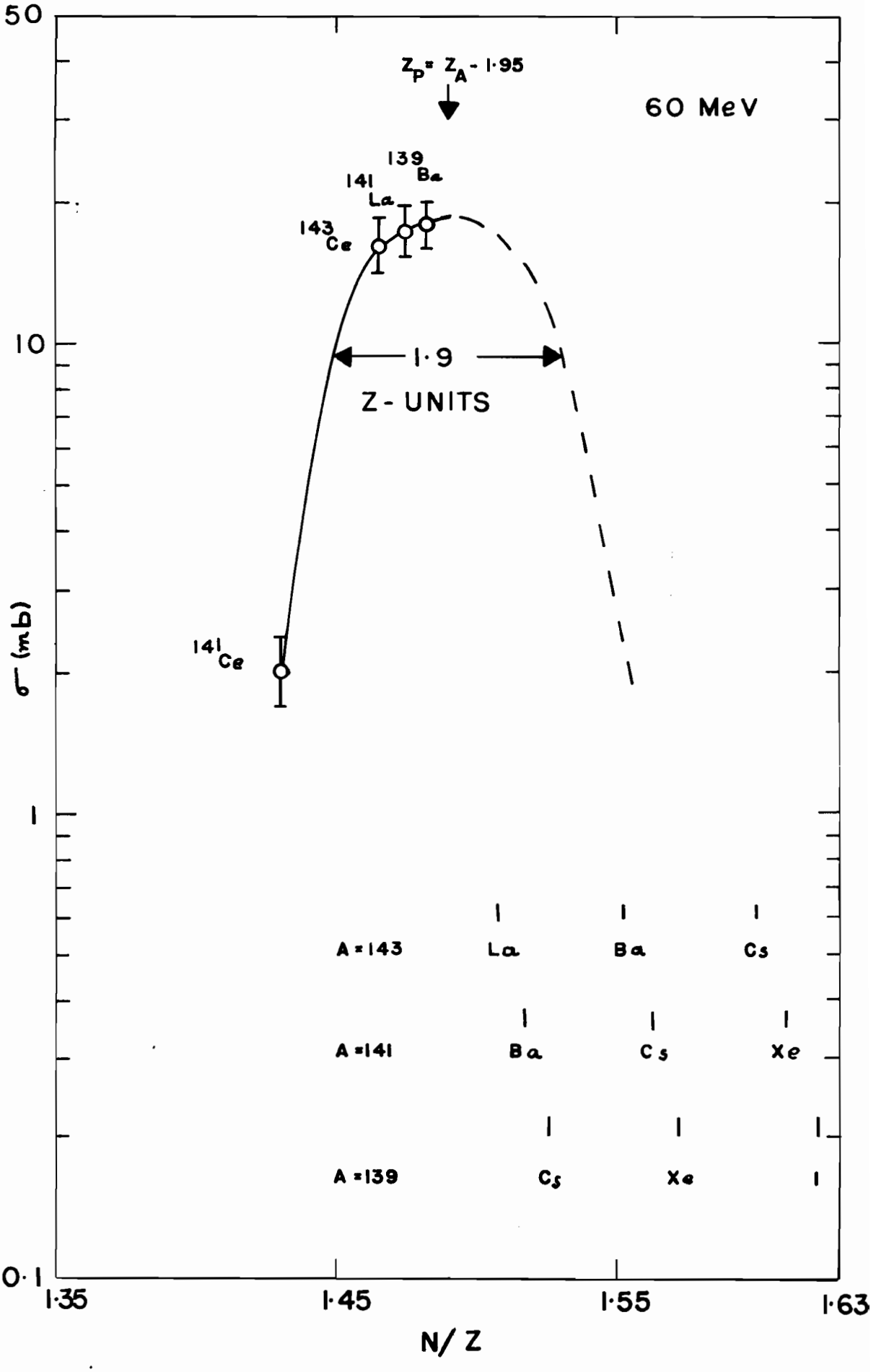
50
10
1
0·1
σ (mb)
$Z_p = Z_A - 1.95$
60 MeV
139 Ba
141 La
143 Ce
141 Ce
1·9
Z - UNITS
A = 143
La
Ba
Cs
A = 141
Ba
Cs
Xe
A = 139
Cs
Xe
I
1·35
1·45
1·55
1·63
N/Z

FIGURE 34

CHARGE DISPERSION AT 70 MeV

[The right-hand (dashed) portion of the curve has been drawn so that the sums of the isobaric yields read off the curve approximate the experimental cumulative yields]

	σ(mb) Experimental	σ(mb) Curve
^{139}Cs	10	10
^{141}Ba	12	13
^{143}La	14	17

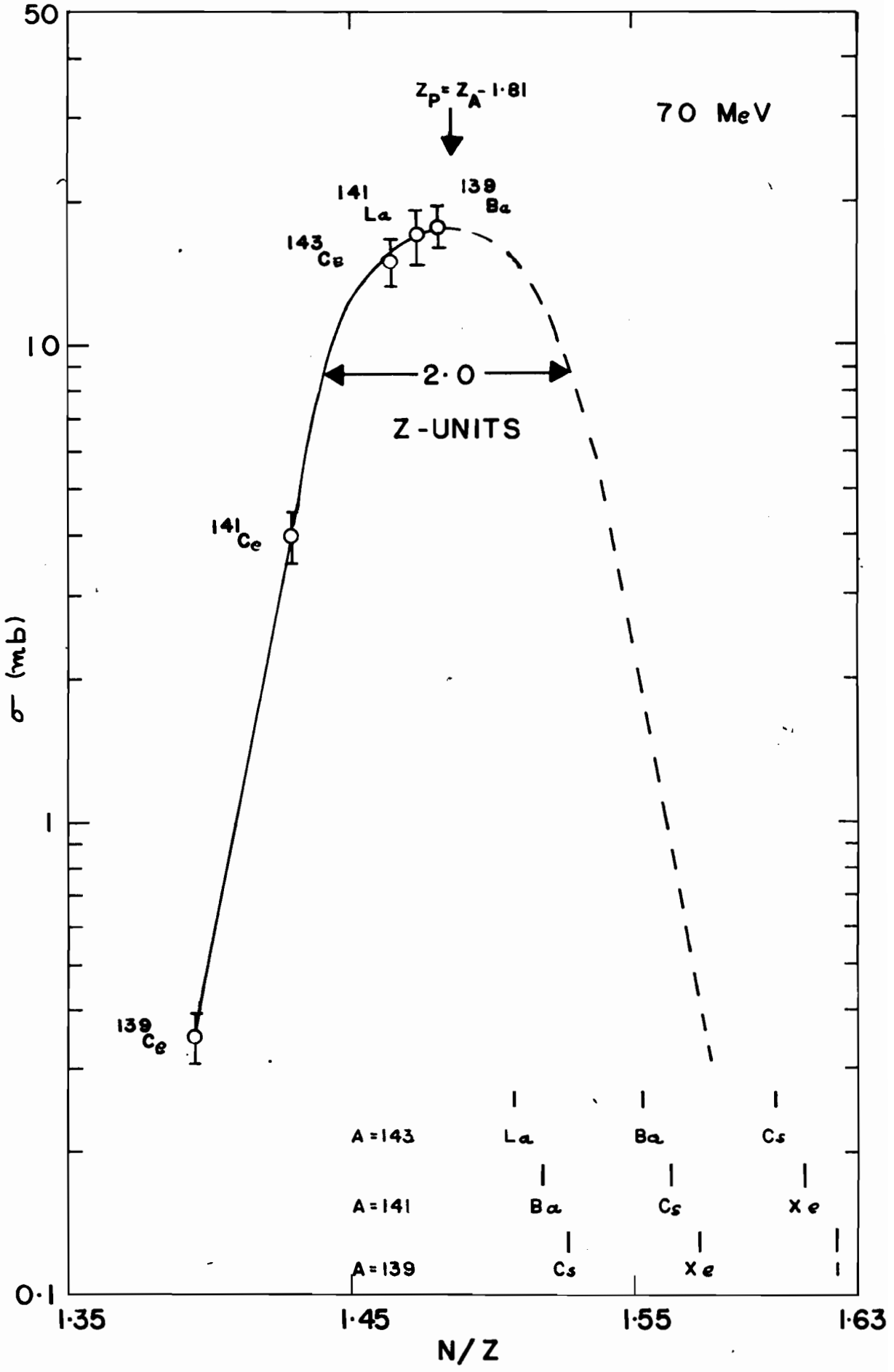
50
10
1
0·1
σ (mb)
$Z_P = Z_A - 1·81$
70 MeV
141 La
139 Ba
143 Ce
141 Ce
139 Ce
2·0
Z-UNITS
A=143
A=141
A=139
La
Ba
Cs
Xe
1·35
1·45
1·55
1·63
N/Z

FIGURE 35

CHARGE DISPERSION AT 80 MeV

[The right-hand (dashed) portion of the curve has been drawn so that the sums of the isobaric yields read off the curve approximate the experimental cumulative yields]

	σ(mb) Experimental	σ(mb) Curve
^{139}Cs	8	7
^{141}Ba	10	9
^{143}La	11	12.5

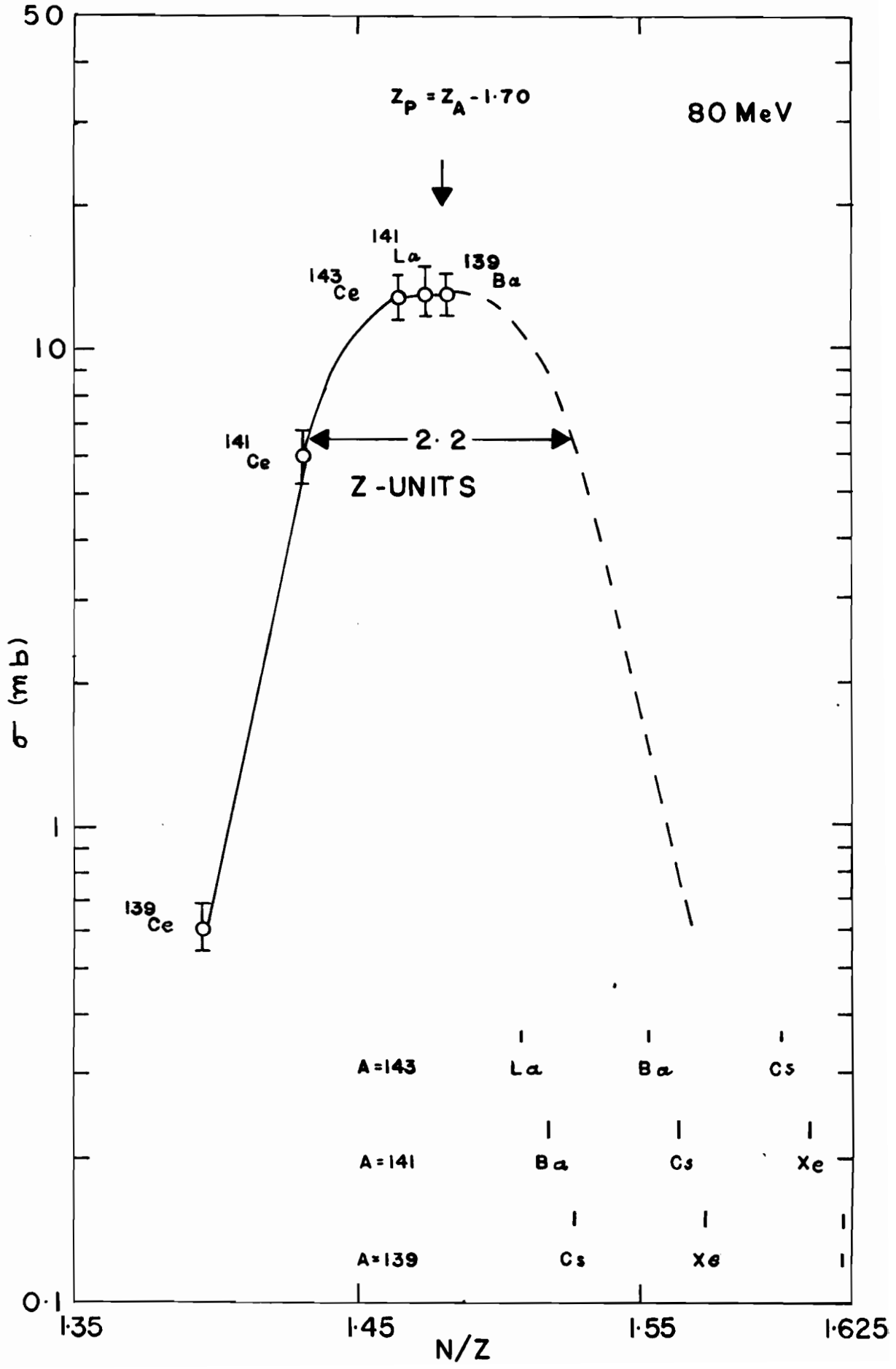
50
10
1
0·1
σ (mb)
$Z_P = Z_A - 1·70$
80 MeV
141 La
139 Ba
143 Ce
141 Ce
139 Ce
2·2
Z-UNITS
A=143
La
Ba
Cs
A=141
Ba
Cs
Xe
A=139
Cs
Xe
1·35
1·45
1·55
1·625
N/Z

FIGURE 36

CHARGE DISPERSION AT 85 MeV

[The right-hand (dashed) portion of the curve has been drawn so that the sums of the isobaric yields read off the curve approximate the experimental cumulative yields]

	σ(mb) Experimental	σ(mb) Curve
^{139}Cs	7.5	7
^{141}Ba	9	9
^{143}La	10	11

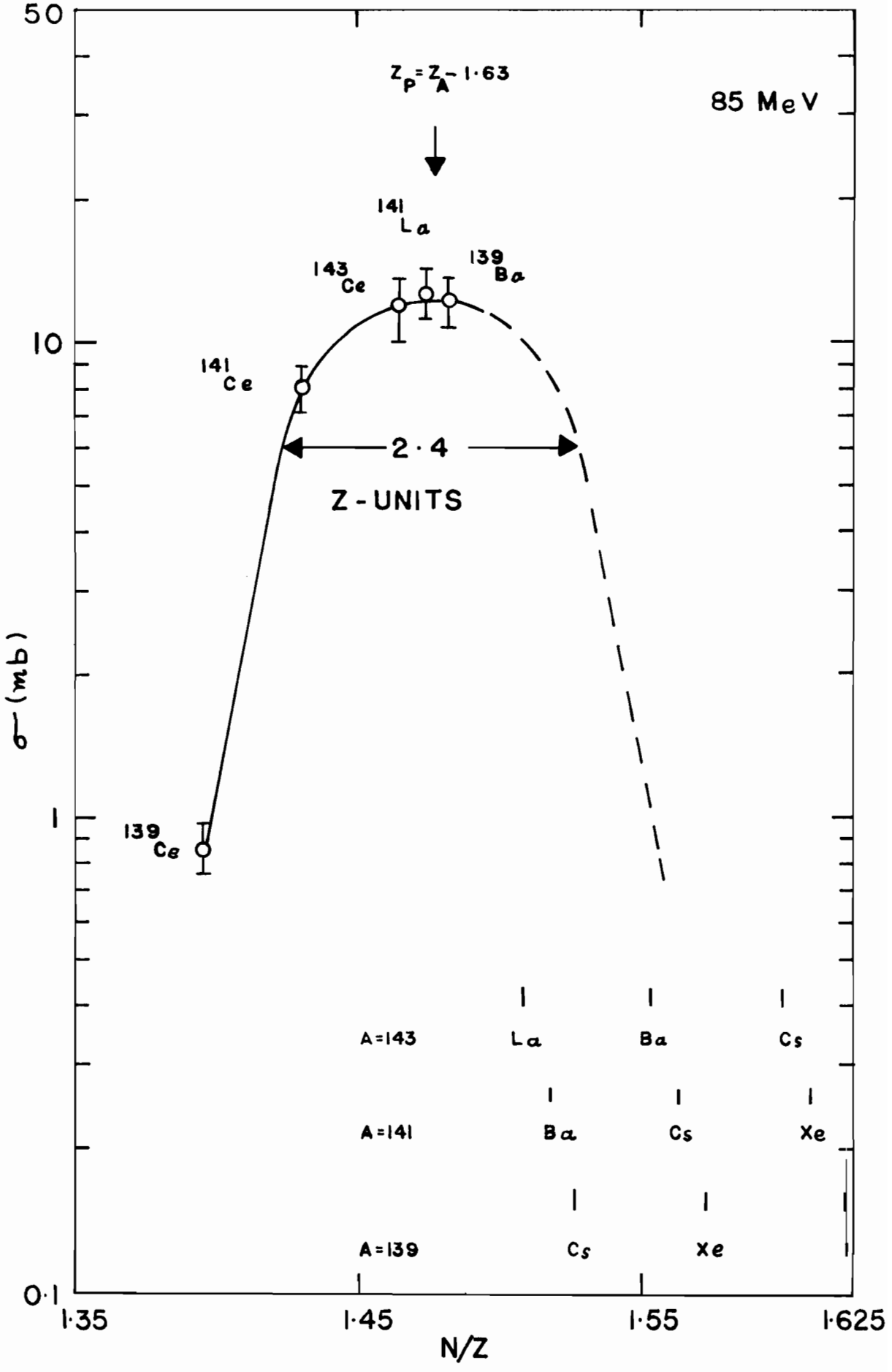
50
10
1
0·1
σ (mb)
$Z_P = Z_A - 1·63$
85 MeV
141 La
143 Ce
139 Ba
141 Ce
139 Ce
2·4
Z-UNITS
A=143
La
Ba
Cs
A=141
Ba
Cs
Xe
A=139
Cs
Xe
1·35
1·45
1·55
1·625
N/Z

criterion imposes severe restrictions and uniquely defines the right-hand portion of the charge dispersion curves. At lower energies the poor agreement between the experimental cumulative yields and those determined from the charge dispersion curves is attributed to the fact that the mass yield curve in this mass region is not flat at these energies.

As the bombarding energy is increased, the charge dispersion curves become broader and the peak position shifts to lower neutron-to-proton, N/Z, ratios. The full width at half-maximum and peak positions at each bombarding energy are given in Table XV (p. 116).

The N/Z value at the peak of the charge dispersion curves and N + Z = 141 are used to obtain the most probable charge, Z_p, for the 141 mass chain. The difference between the most stable charge, Z_A, and the most probable charge, Z_p, for this mass chain is given in Table XV. The Z_A value, as taken by Davies and Yaffe[84], is that of Coryell[81], neglecting shell effects, so that the two sets of data can be compared. Figure 37(a) shows such a comparison where the values of $Z_A - Z_p$ are plotted as a function of proton bombarding energies. Data are also included from 8 - 85 MeV proton-induced thorium fission by Pate, Foster, and Yaffe[38], and at 100 MeV from the work of Friedlander et al.[82] The results are in good agreement. The most probable charge, Z_p, approaches the beta stability line with increase in proton energies.

The values of neutron-to-proton ratios at half-maximum

TABLE XV

PARAMETERS OF CHARGE DISPERSION CURVES

Proton Energy	Full width at half-maximum		Peak Position		
(MeV)	N/Z	Z	N/Z	Z_p	$Z_A - Z_p$
20	0.073	1.6	1.525	55.84	2.71
30	0.073	1.6	1.510	56.17	2.37
40	0.074	1.7	1.500	56.40	2.15
50	0.078	1.8	1.495	56.51	2.04
60	0.082	1.9	1.491	56.60	1.95
70	0.087	2.0	1.485	56.74	1.81
80	0.095	2.2	1.480	56.85	1.70
85	0.103	2.4	1.477	56.92	1.63

$Z_A = 58.55$, for $A = 141$.

FIGURE 37

(a) DISPLACEMENT OF Z_p, TOWARDS BETA STABILITY, Z_A

(b) FULL WIDTH AT HALF-MAXIMUM OF CHARGE DISPERSION CURVE PLOTTED AGAINST INCIDENT PROTON ENERGY

O - This work

□ - Pate, Foster, and Yaffe[38]

▽ - Friedlander, Friedman, Gordon, and Yaffe[82]

X - Davies and Yaffe[84]

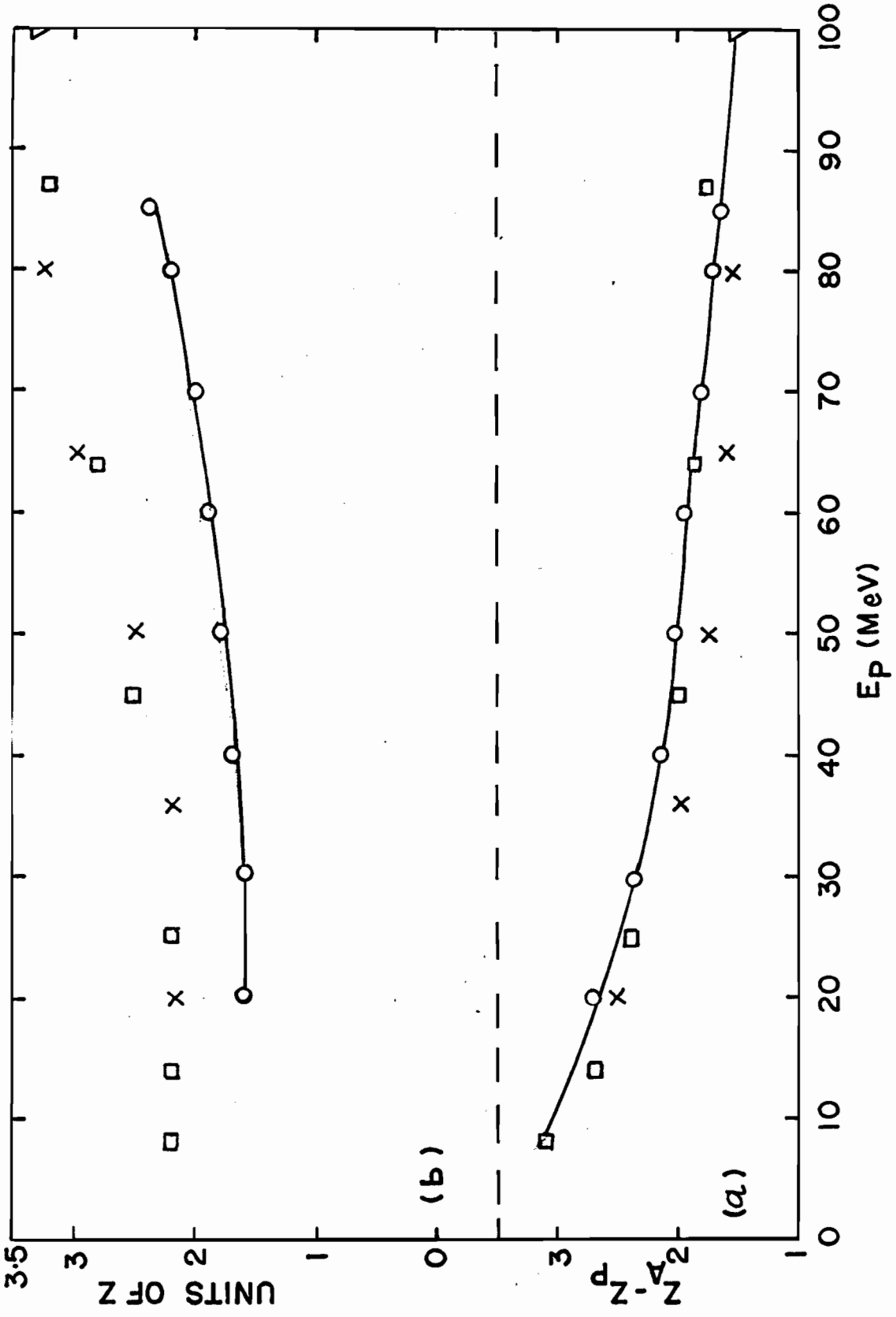
UNITS OF Z
3.5
3
2
1
0
(b)
$Z_A - Z_p$
3
2
1
(a)
0
10
20
30
40
50
60
70
80
90
100
E_p (MeV)

were converted to Z values for the same 141 mass chain to obtain the full width at half-maximum in Z units. These values, given in Table XV, are compared with data from other workers[38,82,84] in Fig. 37(b).

As seen in Fig. 37(b), the full width at half-maximum of the dispersion curves at all energies is narrower than the literature values, but the general trend with energy is the same, i.e. the half-width is constant up to 30 MeV then increases at higher energies. The narrower dispersion curves are probably due to the fact that these results are based on nuclides in which both the proton number and the neutron number are changing in contrast to the other data where mainly the neutron number is changing. An additional effect here may be the directing influence of the 82 neutron shell in the fissioning nucleus, which would be particularly felt in the mass and charge region investigated. A similar effect was observed in the alpha-particle induced fission of uranium isotopes by Colby and Cobble[78] where data for nuclides near to the 82 neutron shell have a narrower charge distribution than nuclides far away from this shell.

The shift of the peak positions of the charge dispersion curves to lower values of neutron-to-proton ratios is reflected in the shift of the most probable charge, Z_p, to beta stability with increasing bombarding energy. The appearance of the neutron-deficient nuclides at higher energies is seen from the measurable amounts of the ^{139}Ce observed from 70 MeV onwards. These two facts bear out the proposition that

increased neutron evaporation takes place either prior to or after fission at higher bombarding energies.[38,82,84] The broadening and lowering of the charge dispersion curves at higher energies then reflect the wider range of the fissioning species at these energies.

The total yields for each mass number were found by summing the individual independent yields of all the isobars for the particular mass chain from the charge dispersion curves. The total isobaric cross-sections for 139, 141, and 143 mass chains as a function of energy are given in Table XVI. No errors have been assigned to these values. The general behaviour is shown in Fig. 38 where the yields for mass number 141 only, the average of the mass region studied, are plotted against proton energies. The yields are seen to decrease continuously from the highest value at 20 MeV. This is in agreement with the work of Stevenson et al.[53] which shows that, as the valley of the mass distribution curve for ^{238}U proton fission fills in at high energies, the shoulders of the curve are pushed in to lower yields. Mass numbers 139 - 143 lie on the right-hand shoulder of the mass distribution curve.

V-C. COMPARISON OF EXPERIMENTAL YIELDS WITH THE WAHL EMPIRICAL CHARGE DISTRIBUTION CURVE

The experimental yields at proton energy of 20 MeV, 30 MeV, 70 MeV, and 85 MeV are compared with the empirical charge distribution curve reported by Wahl et al.[80] These energies are selected because compound nucleus formation will

TABLE XVI

TOTAL ISOBARIC CROSS-SECTIONS FOR A = 139, A = 141, and A = 143 AS A FUNCTION OF ENERGY*

E_p (MeV)	A = 139 σ(mb)	A = 141 σ(mb)	A = 143 σ(mb)
20	45.5	46.0	45.7
30	41.1	42.3	41.9
40	39	40	39.6
50	38.3	39.6	41.2
60	34.8	36	36.5
70	35	34.3	35.9
80	28.8	28.7	28.9
85	28.8	29	29.3

*Calculated from charge dispersion curves.

FIGURE 38

VARIATION OF TOTAL ISOBARIC

CROSS-SECTION FOR A = 141

WITH INCIDENT PROTON ENERGY

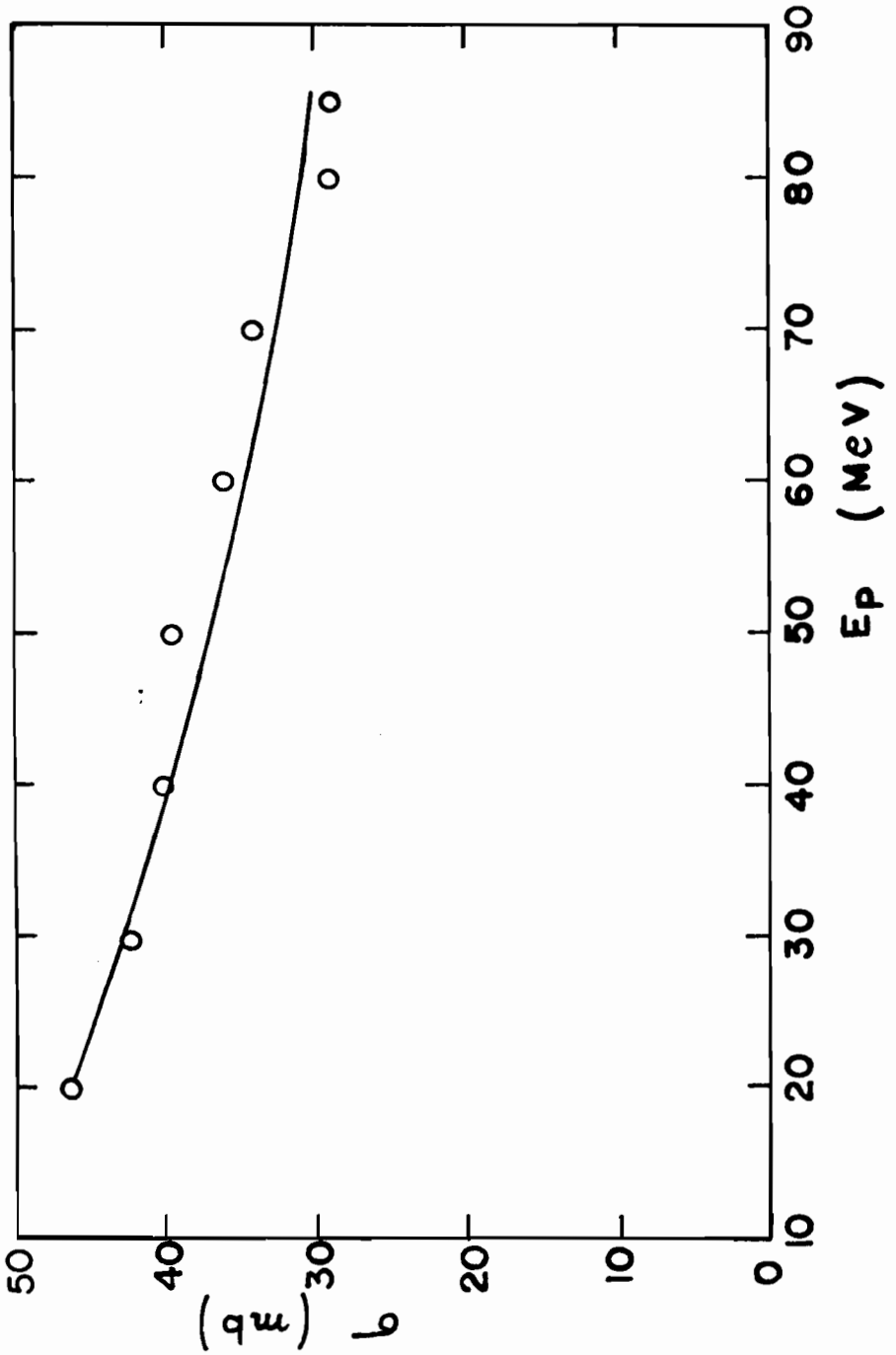
σ (mb)
0
10
20
30
40
50
10
20
30
40
50
60
70
80
90
Ep (MeV)

be the predominant mechanism for bombarding energies up to about 40 MeV and above that fission-neutron-evaporation competition becomes increasingly important. It will be of interest to make such a comparison since the present values of the most probable charge, Z_p, are experimental in contrast to the empirical Z_p values used by Wahl et al.[80] to construct the conventional charge distribution plot (fractional yield versus $Z-Z_p$).

The excitation functions reported in Section IV were used to obtain the independent and the cumulative yields of various fission products. The fractional chain yield of a particular nuclide was calculated from the total yield of the respective mass chain at a particular energy given in Table XVI (Section V-B). The most probable charge, Z_p, for mass chains 139 and 143, was calculated from the neutron-to-proton ratio at the peak of the charge dispersion curve at a given energy in the same way as that described for the 141 mass chain (Section V-B). These values, together with the difference between the nuclear charge, Z, of the particular isobar and the most probable charge, Z_p, of that mass chain, i.e. $Z-Z_p$, are given in Tables XVII to XX inclusive. These data are shown in Fig. 39 where the empirical charge distribution curve and the uncertainties associated with it are also shown. The agreement of the present data with others is quite satisfactory, even though the energy of the projectile varies considerably. Although the mass region ($139 \leq A \leq 143$) investigated here is almost the same as that studied by Wahl et al.[80], the

agreement seems to be more than coincidental. This leads one to believe that charge dispersion can be very adequately represented in the form of a Gaussian distribution as proposed by Wahl et al.[80]

TABLE XVII

FRACTIONAL CHAIN YIELDS AND $Z-Z_p$ FOR NATURAL URANIUM + 20 MeV PROTONS

Fission Product	Independent Yield (mb)	Cumulative Yield (mb)	Total Chain Yield (mb)	Fractional Chain Yield (%)	Z_p*	$Z - Z_p$
$^{139}_{55}Cs$	-	29	45.5	63.7	55.05	-0.05
$^{139}_{56}Ba$	11.1	-	45.5	24.4	55.05	0.95
$^{141}_{56}Ba$	-	43	46.0	93.5	55.84	0.16
$^{141}_{57}La$	9.0	-	46.0	19.6	55.84	1.16
$^{141}_{58}Ce$	0.7	-	46.0	1.5	55.84	2.16
$^{143}_{57}La$	-	26.2	45.7	57.3	56.63	0.37
$^{143}_{58}Ce$	5.0	-	45.7	10.9	56.63	1.37

*$\frac{N}{Z}$ = 1.525, at the peak position of charge dispersion curve.

TABLE XVIII

FRACTIONAL CHAIN YIELDS AND $Z-Z_p$ FOR NATURAL URANIUM + 30 MeV PROTONS

Fission Product	Independent Yield (mb)	Cumulative Yield (mb)	Total Chain Yield (mb)	Fractional Chain Yield (%)	Z_p*	$Z - Z_p$
$^{139}_{55}Cs$	-	21.6	41.1	52.5	55.38	-0.38
$^{139}_{56}Ba$	14.8	-	41.1	36.0	55.38	0.62
$^{141}_{56}Ba$	-	33	42.3	78.0	56.17	-0.17
$^{141}_{57}La$	13.6	-	42.3	32.15	56.17	0.83
$^{141}_{58}Ce$	0.9	-	42.3	2.1	56.17	1.83
$^{143}_{57}La$	-	23.8	41.9	56.8	56.97	0.03
$^{143}_{58}Ce$	8.6	-	41.9	20.5	56.97	1.03

*$\frac{N}{Z}$ = 1.510, at the peak position of charge dispersion curve.

TABLE XIX

FRACTIONAL CHAIN YIELDS AND $Z-Z_p$ FOR NATURAL URANIUM + 70 MeV PROTONS

Fission Product	Independent Yield (mb)	Cumulative Yield (mb)	Total Chain Yield (mb)	Fractional Chain Yield (%)	Z_p^*	$Z - Z_p$
$^{139}_{55}Cs$	-	10	35	28.6	55.94	-0.94
$^{139}_{56}Ba$	16.0	-	35	45.7	55.94	0.06
$^{139}_{58}Ce$	0.35	-	35	1.0	55.94	2.06
$^{141}_{56}Ba$	-	12.3	34.3	35.9	56.74	-0.74
$^{141}_{57}La$	16.4	-	34.3	47.8	56.74	0.26
$^{141}_{58}Ce$	3.2	-	34.3	9.3	56.74	1.26
$^{143}_{57}La$	-	13.8	35.9	38.4	57.54	-0.54
$^{143}_{58}Ce$	14.8	-	35.9	41.2	57.54	0.46

$^*\frac{N}{Z} = 1.485$, at the peak position of charge dispersion curve.

TABLE XX

FRACTIONAL CHAIN YIELDS AND $Z-Z_p$ FOR NATURAL URANIUM + 85 MeV PROTONS

Fission Product	Independent Yield (mb)	Cumulative Yield (mb)	Total Chain Yield (mb)	Fractional Chain Yield (%)	Z_p*	$Z - Z_p$
$^{139}_{55}Cs$	-	7.6	28.8	26.4	56.12	-1.12
$^{139}_{56}Ba$	12.8	-	28.8	44.4	56.12	-0.12
$^{139}_{58}Ce$	0.8	-	28.8	2.8	56.12	1.88
$^{141}_{56}Ba$	-	8.6	29	29.6	56.92	-0.92
$^{141}_{57}La$	12.3	-	29	42.4	56.92	0.08
$^{141}_{58}Ce$	8.1	-	29	27.9	56.92	1.08
$^{143}_{57}La$	-	10	29.3	34.1	57.73	-0.73
$^{143}_{58}Ce$	11.6	-	29.3	39.6	57.73	0.27

*$\frac{N}{Z}$ = 1.477, at the peak position of charge dispersion curve.

FIGURE 39

COMPARISON OF INDEPENDENT AND CUMULATIVE YIELDS WITH THE EMPIRICAL CHARGE DISTRIBUTION CURVE OF WAHL ET AL.[80]

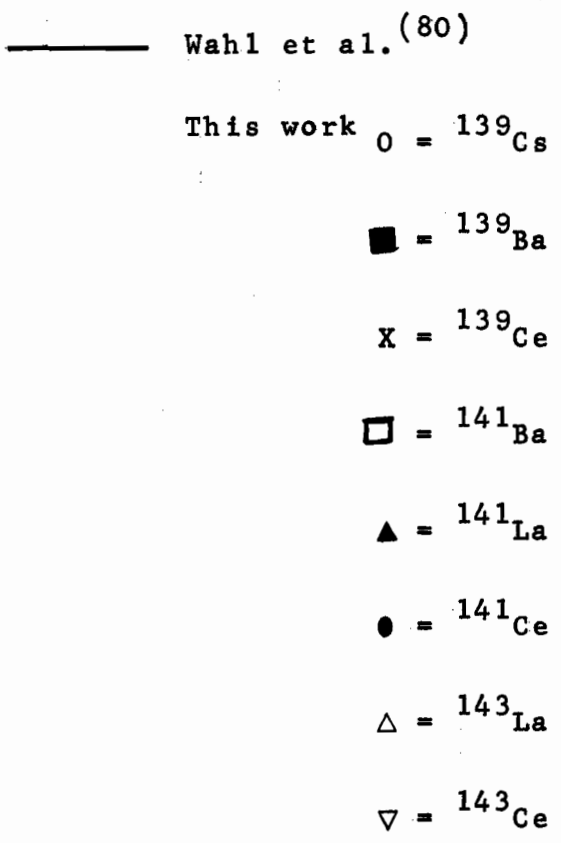

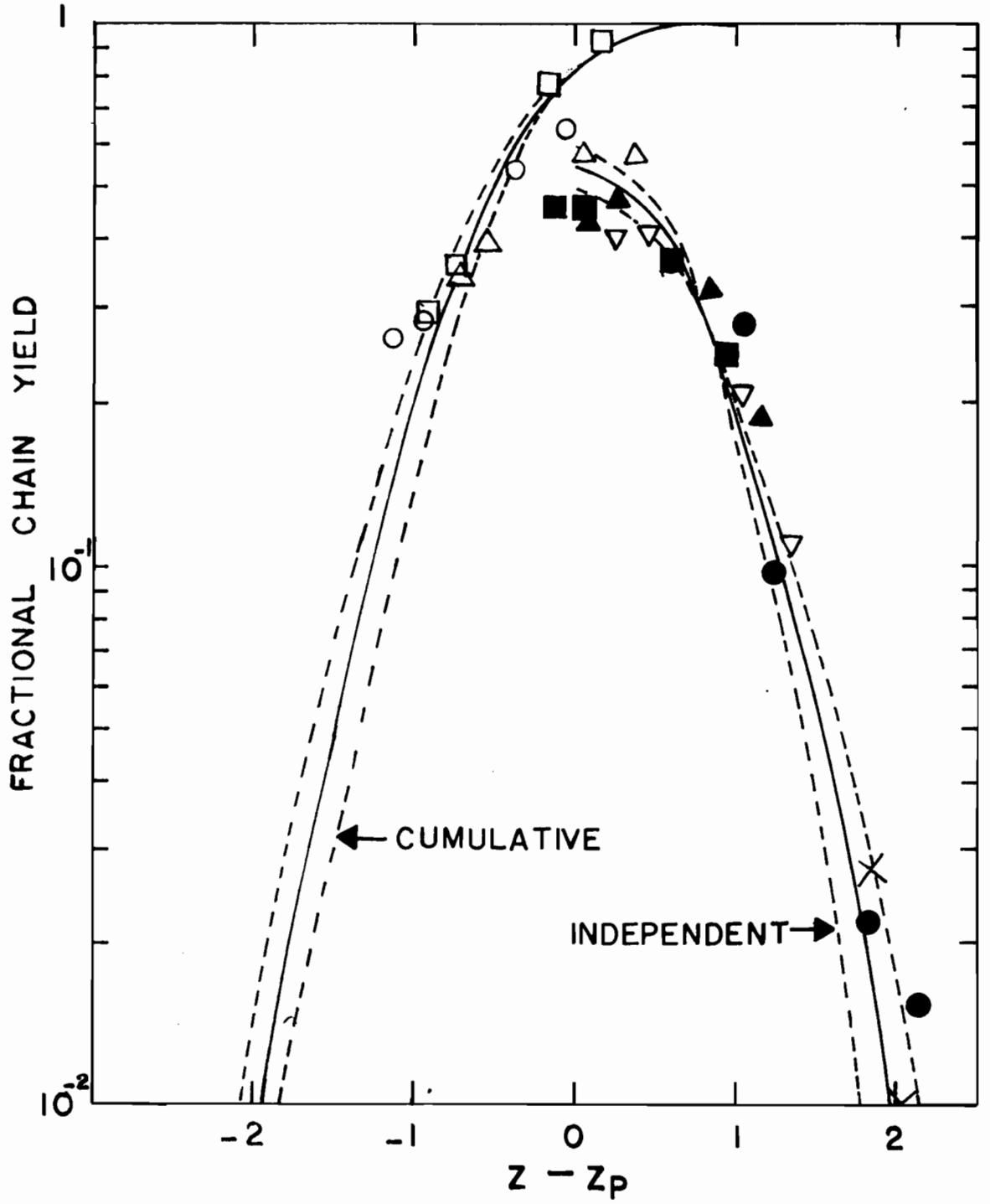
1
10^{-1}
10^{-2}
FRACTIONAL CHAIN YIELD
CUMULATIVE
INDEPENDENT
-2
-1
0
1
2
$Z - Z_P$

VI. SUMMARY AND CONTRIBUTION TO KNOWLEDGE

Isobaric yield distributions in the fission of natural uranium by 20 - 85 MeV protons have been studied. The mass region investigated was $139 \leqslant A \leqslant 143$.

The independent formation cross-sections of ^{139}Ba, ^{139}Ce, ^{141}La, ^{141}Ce, and ^{143}Ce and the cumulative formation cross-sections of ^{139}Cs, ^{141}Ba, and ^{143}La have been determined at various proton energies by radiochemical techniques.

Excitation functions for each of the fission products studied have been constructed and they were found to have the expected shapes and magnitudes. The excitation function for ^{143}Pr interpolated from charge dispersion curves is also reported.

The proton energies at which the excitation functions reach their maxima were plotted as a function of the neutron-to-proton ratio of the product. The data from the literature were also included to obtain the composite graph. The curve seems to indicate that the neutron-to-proton ratio of the product is a fundamental parameter and might be useful for the correlation of other fission data, as pointed out by Friedlander et al.[82]

Independent formation cross-section data were plotted as a function of neutron-to-proton ratio of the fission product to construct the nuclear charge dispersion curves at proton energies of 20, 30, 40, 50, 60, 70, 80, and 85 MeV. The cumulative yields were used to define the right-hand portion of

the curves. With increasing proton energy the curves broaden and the most probable charge approaches the line of beta-stability. These phenomena are accounted for qualitatively in terms of neutron evaporation. The charge dispersion curves were narrower than those reported in the literature from similar studies. Total isobaric cross-sections, as a function of energy, were interpolated from the charge dispersion curves.

Experimental yields were compared with Wahl's empirical charge distribution curve, and the agreement was very satisfactory. It seems that charge dispersion can be very adequately represented in the form of a Gaussian distribution as proposed by Wahl et al.[80]

APPENDIX A

EQUATIONS FOR CUMULATIVE FORMATION CROSS-SECTION CALCULATIONS

With a thin target approximation, when a target is bombarded with a beam of projectiles, the rate of formation of a product nuclide, A, is given as

$$\frac{dN_A}{dt} = \sigma_A \, I \, n_T \qquad (A\text{-}1)$$

where σ_A = formation cross-section of the nuclide, A, in cm^2, under the conditions of the reaction,

I = projectile beam intensity called 'flux', which is the number of particles per cm^2 per second,

N_A = number of atoms of the nuclide, A, and

n_T = number of target nuclei presented to the beam.

When a product nuclide is radioactive, it will decay during the time of bombardment. This can be accounted as follows:

$$\frac{dN_A}{dt} = \sigma_A \, I \, n_T - N_A\lambda_A \qquad (A\text{-}2)$$

where $N_A\lambda_A$ = decay rate of the product nuclide, A, and

λ_A = decay constant of the product nuclide, A.

If the beam intensity, I, is considered constant during the bombardment, and imposing the boundary condition

that at $t = 0$, $N_A = 0$, and denoting $t = t_o$, where t_o is the duration of bombardment, then equation (A-2) has the following solution for N_A at the end of bombardment, i.e. N_A^o.

$$N_A^o = \frac{\sigma_A}{\lambda_A} I\, n_T\, (1 - e^{-\lambda_A t_o}) \qquad (A-3)$$

or $$N_A^o \lambda_A = D_A^o = \sigma_A\, I\, n_T\, (1 - e^{-\lambda_A t_o}) \qquad (A-4)$$

where D_A^o is the disintegration rate of the product nuclide A at the end of bombardment.

Equation (A-4) can be used to calculate the formation cross-section of any shielded nuclide or any nuclide whose precursors have decayed completely at the time of chemical separation, i.e. the cumulative formation cross-section, provided the disintegration rate at the end of bombardment of that product nuclide is known. However, it is very difficult to determine the exact value of the beam intensity, I, and this is usually accomplished by monitoring the beam with an appropriate monitor reaction whose formation cross-section is well known. If the monitor is bombarded under similar conditions as the target itself, then equation (A-4) when applied to the monitor reaction gives,

$$D_M^o = \sigma_M\, I\, n_M\, (1 - e^{-\lambda_M t_o}) \qquad (A-5)$$

where the subscript M refers to the monitor.

The following expression is obtained by dividing equation (A-4) by equation (A-5) and rearranging.

$$\sigma_A = \sigma_M \times \frac{D_A^o}{D_M^o} \times \frac{n_M}{n_T} \times \frac{(1 - e^{-\lambda_M t_o})}{(1 - e^{-\lambda_A t_o})} \qquad (A\text{-}6)$$

The above expression can be rearranged as follows. One substitutes appropriate values for n_T and n_M, and also takes into account the natural abundance, N.A., of the particular isotope of the element, which is of interest in the nuclear reaction under study, in terms of the superficial density, S.D., in equation (A-6). Since the area presented to the beam of incoming particles is the same for both the target and monitor foils, then

$$\sigma_A = \frac{D_A^o}{(1-e^{-\lambda_A t_o})} \times \frac{(S.D.)_M}{(S.D.)_T} \times \frac{(N.A.)_M}{(N.A.)_T} \times \frac{(A.W.)_T}{(A.W.)_M} \times \frac{\sigma_M}{D_M^o} \times \frac{(1-e^{-\lambda_M t_o})}{1} \qquad (A\text{-}7)$$

or
$$\sigma_A = D_A^{\infty} \times F \qquad (A\text{-}8)$$

where $D_A^{\infty} = \dfrac{D_A^o}{(1 - e^{-\lambda_A t_o})}$,

$$F = \frac{(S.D.)_M}{(S.D.)_T} \times \frac{(N.A.)_M}{(N.A.)_T} \times \frac{(A.W.)_T}{(A.W.)_M} \times \frac{\sigma_M}{D_M^{\infty}} \quad , \quad \text{and}$$

$$D_M^{\infty} = \frac{D_M^o}{(1 - e^{-\lambda_M t_o})} \quad .$$

The subscripts T and M refer to the target and the monitor respectively. Equation (A-8) is of the same form as that given by Friedlander et al.[82]

APPENDIX B

EQUATIONS FOR CROSS-SECTION CALCULATIONS FOR A PARENT-DAUGHTER PAIR

The symbols used in the following equations have the same meaning as stated in Appendix A, otherwise they are defined for clarity.

Consider a chain A → B → C (stable). The fractional chain yield, f, of the nuclide B is given as

$$f = \frac{\sigma_B}{\sigma_A + \sigma_B + \sigma_C} \qquad (B\text{-}1)$$

where σ_A = cumulative formation cross-section of the parent nuclide, A,

σ_B = independent formation cross-section of the daughter nuclide, B, and

σ_C = independent formation cross-section of the stable nuclide, C.

If N_A is the number of nuclei of A at any time, t, which is the time of removal of A after the end of bombardment, the net rate of production of A, as given in Appendix A, is

$$\frac{dN_A}{dt} = \sigma_A I n_T - N_A \lambda_A \qquad (A\text{-}2)$$

And the amount of A present at the end of the

bombardment is

$$N_A^o = \frac{\sigma_A \; I \; n_T}{\lambda_A} \left(1 - e^{-\lambda_A t_o}\right) \qquad (A\text{-}3)$$

where t_o is the duration of bombardment.

Again, if N_B is the number of nuclei of B (daughter) at any time t, the net rate of production of B is

$$\frac{dN_B}{dt} = \sigma_A \; I \; n_T \left(1 - e^{-\lambda_A t}\right) + \sigma_B \; I \; n_T - N_B \lambda_B \qquad (B\text{-}2)$$

In equation (B-2), the first group of terms appears due to parent nuclide, A, the second term is from the independent formation of daughter nuclide, B, and the last term takes care of the decay of the daughter nuclide, B.

The amount of B present at the end of the bombardment is

$$N_B^o = \frac{I \; n_T \; (\sigma_A + \sigma_B)}{\lambda_B} \times \left(1 - e^{-\lambda_B t_o}\right) - \frac{I \; n_T \; \sigma_A \; \left(e^{-\lambda_A t_o} - e^{-\lambda_B t_o}\right)}{\lambda_B - \lambda_A} \qquad (B\text{-}3)$$

Also, during the interval between the end of the bombardment and the removal of A (the separation time), the amount of B growing from an initial amount of N_A^o in a time, t, is

$$\frac{\lambda_A \times N_A^o}{\lambda_B - \lambda_A} \times \left(e^{-\lambda_A t} - e^{-\lambda_B t}\right) \qquad (B\text{-}4)$$

And the amount of B remaining from an original amount of N_B^o, after time t, is

$$N_B^o \, e^{-\lambda_B t} \tag{B-5}$$

Therefore, when A is removed, the amount of B present is

$$N_B^s = \frac{\lambda_A N_A^o}{\lambda_B - \lambda_A} \times (e^{-\lambda_A t} - e^{-\lambda_B t}) + N_B^o \, e^{-\lambda_B t} \tag{B-6}$$

Substituting for N_A^o and N_B^o from equations (A-3) and (B-3), gives

$$N_B^s = I \, n_T \left[\frac{\sigma_A}{(\lambda_B - \lambda_A)} \left\{ (1 - e^{-\lambda_A t_o})(e^{-\lambda_A t} - e^{-\lambda_B t}) - (e^{-\lambda_A t_o} - e^{-\lambda_B t_o}) \times e^{-\lambda_B t} \right\} + \frac{(\sigma_A + \sigma_B)}{\lambda_B} \times (1 - e^{-\lambda_B t_o}) \times e^{-\lambda_B t} \right] \tag{B-7}$$

Multiplying equation (B-7) through by λ_B and rearranging, the disintegration rate, D_B^s, of the daughter nuclide B at time t after the end of the bombardment is given by

$$D_B^s(t_o, t) = I \, n_T \left[\sigma_A \left\{ \frac{\lambda_B}{(\lambda_B - \lambda_A)} \times (1 - e^{-\lambda_A t_o}) \times e^{-\lambda_A t} - \frac{\lambda_A}{(\lambda_B - \lambda_A)} \times (1 - e^{-\lambda_B t_o}) \times e^{-\lambda_B t} \right\} + \sigma_B (1 - e^{-\lambda_B t_o}) \times e^{-\lambda_B t} \right] \tag{B-8}$$

Equation (B-8) can be re-written in the following simple form:

$$D_B^s(t_o,t) = I\ n_T \left[\lambda_B(K_1\sigma_A + K_2\sigma_B)\right] \tag{B-9}$$

where $$K_1 = \frac{e^{-\lambda_A t}(1 - e^{-\lambda_A t_o}) - (\lambda_A/\lambda_B)e^{-\lambda_B t}(1 - e^{-\lambda_B t_o})}{\lambda_B - \lambda_A} \tag{B-10}$$

and $$K_2 = \frac{e^{-\lambda_B t}(1 - e^{-\lambda_B t_o})}{\lambda_B} \tag{B-11}$$

Again, for the beam intensity, I, as explained in Appendix A, recalling equation (A-5) which is

$$D_M^o = \sigma_M\ I\ n_M(1 - e^{-\lambda_M t_o}) \tag{A-5}$$

or $$\frac{D_M^o}{(1 - e^{-\lambda_M t_o})} = D_M^\infty = \sigma_M\ I\ n_M \tag{B-12}$$

Dividing equation (B-9) by equation (B-12) gives

$$\frac{D_B^s}{D_M^\infty} = \frac{n_T}{\sigma_M n_M} \times \left[\lambda_B(K_1\sigma_A + K_2\sigma_B)\right] \tag{B-13}$$

or $$D_B^s = \frac{D_M^\infty}{\sigma_M} \times \frac{n_T}{n_M} \times \left[\lambda_B(K_1\sigma_A + K_2\sigma_B)\right] \tag{B-14}$$

Substituting for n_T and n_M, and since the area presented to the beam of incoming particles is the same for both the target and monitor foils, equation (B-14) becomes

$$D_B^s = \frac{\lambda_B}{F} (K_1 \sigma_A + K_2 \sigma_B) \qquad (B-15)$$

where F is as defined in equation (A-8). Equation (B-15) is similar to that given by Friedlander et al.[82]

APPENDIX C

EQUATIONS FOR ^{140}Ba + ^{140}La CONTRIBUTION

$$\longrightarrow {}^{140}Ba\ (A) \xrightarrow{12.8\ d.} {}^{140}La\ (B) \xrightarrow{40.2\ h.} {}^{140}Ce\ (C)\ (stable)$$

The disintegration rate of ^{140}La activity, D_B, at any time, t, is

$$D_B = \frac{\lambda_B}{\lambda_B - \lambda_A} \cdot D_A^o \left(e^{-\lambda_A t} - e^{-\lambda_B t}\right) \qquad (C\text{-}1)$$

where D_A^o = disintegration rate of ^{140}Ba activity at zero time, and

λ_A and λ_B = decay constants of ^{140}Ba and ^{140}La respectively.

Again, the disintegration rate of ^{140}Ba activity, D_A, at any time, t, is

$$D_A = D_A^o\, e^{-\lambda_A t} \qquad (C\text{-}2)$$

Therefore

$$D_A + D_B = D_{total} = D_A^o\, e^{-\lambda_A t} + \frac{\lambda_B}{\lambda_B - \lambda_A} \cdot D_A^o \left(e^{-\lambda_A t} - e^{-\lambda_B t}\right) \qquad (C\text{-}3)$$

or

$$D_A^o = \frac{D_{total}}{e^{-\lambda_A t} + \frac{\lambda_B}{\lambda_B - \lambda_A}\left(e^{-\lambda_A t} - e^{-\lambda_B t}\right)} \qquad (C\text{-}4)$$

$$\text{or} \quad D_{total} = D_A^o \left[e^{-\lambda_A t} + \frac{\lambda_B}{\lambda_B - \lambda_A} \left(e^{-\lambda_A t} - e^{-\lambda_B t} \right) \right] \qquad \text{(C-5)}$$

Since D_{total} ($^{140}Ba + {}^{140}La$) at any time t, after ^{139}Ba has completely decayed to stable ^{139}La, is known from the tail portion of the gross decay curve, D_A^o can be calculated from equation (C-4). Knowing D_A^o, equation (C-5) can be used to calculate D_{total}, $^{140}Ba + {}^{140}La$, at various times.

Equations (C-4) and (C-5) were used to calculate the contribution due to $^{140}Ba + {}^{140}La$, which was then subtracted from the observed gross counts to determine the activity of ^{139}Ba.

REFERENCES

1. E. Fermi, E. Amaldi, O. d'Agostino, F. Rasetti, and E. Segrè, Proc. Roy. Soc., A146, 483 (1934).

2. O. Hahn and F. Strassmann, Naturwiss, 27, 11 (1939).

3. L. Meitner and O.R. Frisch, Nature, 143, 239 (1939).

4. G.N. Flerov and K.A. Petrzhak, Phys. Rev., 58, 89 (1940).

5. N. Bohr, Nature, 137, 344 (1936).

6. J.M. Blatt and V.F. Weisskopf, 'Theoretical Nuclear Physics', published by John Wiley and Sons, New York, (1952).

7. M.M. Shapiro, Phys. Rev., 90, 171 (1953).

8. S.N. Ghoshal, Phys. Rev., 80, 939 (1950).

9. W. John, Jr., Phys. Rev., 103, 704 (1956).

10. E.L. Kelly, (Thesis) University of California Radiation Laboratory Report UCRL-1044, Dec. 1950.
    E.L. Kelly and E. Segrè, Phys. Rev., 75, 999 (1949).

11. A.H. Armstrong and L. Rosen, Nucl. Phys., 19, 40 (1960).

12. R. Sherr and F.P. Brady, Phys. Rev., 124, 1928 (1961).

13. N.O. Lassen and N.O. Roy Poulsen, International Conference on Low Energy Nuclear Physics, Paris, July 1958.

14. R. Serber, Phys. Rev., 72, 1114 (1947).

15. J.W. Meadows, Phys. Rev., 91, 885 (1953).

16. P.C. Gugelot, Phys. Rev., 93, 425 (1954).

17. B.L. Cohen, Phys. Rev., 105, 1549 (1957).

18. R.M. Eisberg and G. Igo, Phys. Rev., 93, 1039 (1954).

19. A.A. Caretto and E.O. Wiig, Phys. Rev., 115, 1238 (1959).

20. M.L. Goldberger, Phys. Rev., 74, 1268 (1948).

21. G. Bernardini, E.T. Booth, and S.J. Lindenbaum, Phys. Rev., 88, 1017 (1952).

22. H. McManus, W.T. Sharp, and H. Gellman, Phys. Rev., 93, 924 (1954).

23. G. Rŭdstam, Thesis, Uppsala (1956).

24. N. Metropolis, R. Bivins, M. Storm, A. Turkevich, J.M. Miller, and G. Friedlander, Phys. Rev., 110, 185 (1958).

25. N. Metropolis, R. Bivins, M. Storm, J.M. Miller, G. Friedlander, and A. Turkevich, Phys. Rev., 110, 204 (1958).

26. K.J. Le Couteur, Proc. Phys. Soc. (London), A63, 259 (1950).

27. J.D. Jackson, Can. J. Phys., 34, 767 (1956).

28. I. Dostrovsky, P. Rabinowitz, and R. Bivins, Phys. Rev., 111, 1659 (1958).

29. I. Dostrovsky, Z. Fraenkel, and G. Friedlander, Phys. Rev., 116, 683 (1959).

30. A.A. Caretto and G. Friedlander, Phys. Rev., 110,1169 (1958).

31. S.S. Markowitz, F.S. Rowland, and G. Friedlander, Phys. Rev., 112, 1295 (1958).

32. R.W. Spence and G.P. Ford, Ann. Rev. Nuclear Sci., 2, 399 (1953).

33. R. Vandenbosch, T.D. Thomas, S.E. Vandenbosch, R.A. Glass, and G.T. Seaborg, Phys. Rev., 111,1358 (1958).

34. W.J. Nicholson and I. Halpern, Phys. Rev., 116, 175 (1959).

35. B.M. Foreman, Jr., W.M. Gibson, R.A. Glass, and G.T. Seaborg, Phys. Rev., 116, 382 (1959).

36. M. Lindner and A. Turkevich, Phys. Rev., 119, 1632 (1960).

37. B.D. Pate, Can. J. Chem., 36, 1707 (1958).

38. B.D. Pate, J.S. Foster, and L. Yaffe, Can. J. Chem., 36, 1691 (1958).

39. A.K. Lavrukhina and L.D. Krasavina, J. Nuclear Energy, 5, 236 (1957).

40. I. Halpern, Ann. Rev. Nuclear Sci., 9, 245 (1959).

41. G.T. Seaborg, Phys. Rev., 88, 1429 (1952).

42. H.G. Thode, C.C. McMullen, and K. Fritze, 'Advances in Inorganic Chemistry and Radiochemistry', 2, p. 315, published by Academic Press Inc., New York (1960).

43. D.C. Brunton and G.C. Hanna, Can. J. Research, A28, 190 (1950).

44. D.C. Brunton and W.B. Thompson, Can. J. Research, A28, 498 (1950).

45. S.S. Friedland, Phys. Rev., 84, 75 (1951).

46. J.S. Wahl, Phys. Rev., 95, 126 (1954).

47. R.B. Leachman, Phys. Rev., 87, 444 (1952).

48. J.C.D. Milton and J.S. Fraser, Can.J.Phys., 40, 1626 (1962).

49. H.C. Britt and S.L. Whetstone, Jr., Phys. Rev., 133, B603 (1964).

50. S.L. Whetstone, Jr., Phys. Rev., 133, B613 (1964).

51. J.C.D. Milton and J.S. Fraser, 'Symposium on the Physics and Chemistry of Fission', International Atomic Energy Agency, Salzburg, Austria, March 1965, Paper SM-60/45.

52. S. Katcoff, Nucleonics, 18, 201 (1960).

53. P.C. Stevenson, H.G. Hicks, W.E. Nervik, and D.R. Nethaway, Phys. Rev., 111, 886 (1958).

54. M. Lindner and R.N. Osborne, Phys. Rev., 94, 1323 (1954).

55. H.G. Hicks, P.C. Stevenson, R.S. Gilbert, and W.H. Hutchin, Phys. Rev., 100, 1284 (1955).

56. H.G. Hicks and R.S. Gilbert, Phys. Rev., 100, 1286 (1955).

57. G. Friedlander, Paper SM-60/63 in Ref. (51).

58. K. Way and E.P. Wigner, 'Radiochemical Studies: the Fission Products', published by McGraw-Hill Book Company, Inc., New York (1951), Paper No. 43, National Nuclear Energy Series, Plutonium Project Record, Vol. 9.

59. R.D. Present, Phys. Rev., 72, 7 (1947).

60. N. Sugarman and A. Turkevich, Private communication of Ref. (62), Paper No. 52 in Ref. (58).

61. R.H. Goeckermann and I.Perlman, Phys. Rev., 76, 628 (1949).

62. L.E. Glendenin, C.D. Coryell, and R.A. Edwards, Paper No. 52 in Ref. (58).

63. A.C. Pappas, M.I.T. Tech. Report No. 63 (1953); and 'Proceedings of the International Conference on the Peaceful Uses of Atomic Energy', Geneva (1955), United Nations, New York, 1956, Vol. 7, P. 19.

64. C.D. Coryell, M. Kaplan, and R.D. Fink, Can. J. Chem., 39, 646 (1961).

65. A.C. Wahl, Paper SM-60/22 in Ref. (51).

66. P. Armbruster, D. Hovestadt, H. Meister, and H.J. Specht, Nucl. Phys., 54, 586 (1964).

67. L.E. Glendenin, H.C. Griffen, and J.P. Unik, Paper SM-60/31 in Ref. (51).

68. T.D. Thomas, R.A. Atneosen, W.M. Gibson, and M.L. Perlman, Paper SM-60/57 in Ref. (51).

69. A.C. Wahl, Phys. Rev., 99, 730 (1955).

70. T.J. Kennett and H.G. Thode, Phys. Rev., 103, 323 (1956).

71. J.M. Alexander and C.D. Coryell, Phys. Rev.,108,1274 (1957).

72. W.M. Gibson, (Thesis) University of California Radiation Laboratory Report UCRL-3493 (1956).

73. N.T. Porile and N. Sugarman, Phys. Rev., 107, 1410 (1957).

74. A.C. Wahl, J. Inorg. Nuclear Chem., 6, 263 (1958).

75. Y.Y. Chu, (Thesis) University of California Radiation Laboratory Report UCRL-8926 (1959).

76. G. Friedlander and L. Yaffe, Phys. Rev., 117, 578 (1960).

77. G. Rüdstam and A.C. Pappas, Nucl. Phys., 22, 468 (1961).

78. L.J. Colby, Jr., and J.W. Cobble, Phys. Rev.,121,1410 (1961).

79. A. Kjelberg, H. Taniguchi, and L. Yaffe, Can. J. Chem., 39, 635 (1961).

80. A.C. Wahl, R.L. Ferguson, D.R. Nethaway, D.E. Troutner, and K. Wolfsberg, Phys. Rev., 126, 1112 (1962).

81. C.D. Coryell, Ann. Rev. Nuclear Sci., 2, 305 (1953).

82. G. Friedlander, L. Friedman, B. Gordon, and L. Yaffe, Phys. Rev., 129, 1809 (1963).

83. S. Kaufman, Phys. Rev., 129, 1866 (1963).

84. J.H. Davies and L. Yaffe, Can. J. Phys., 41, 762 (1963).

85. A.C. Wahl and D.R. Nethaway, Phys. Rev., 131, 830 (1963).

86. D.E. Troutner, A.C. Wahl, and R.L. Ferguson, Phys. Rev., 134, B1027 (1964).

87. P.P. Benjamin, N.T. Porile, and L. Yaffe - to be published.

88. N. Bohr and J.A. Wheeler, Phys. Rev., 56, 426 (1939).

89. J. Frenkel, Phys. Rev., 55, 987 (1939).

90. M.G. Mayer, Phys. Rev., 74, 235 (1948).

91. M.G. Mayer, Phys. Rev., 75, 1969 (1949).

92. M.G. Mayer, Phys. Rev., 78, 16 (1950).

93. W.J. Swiatecki, Phys. Rev., 83, 178 (1951).

94. Th. A.J. Maris, Phys. Rev., 101, 502 (1956).

95. P. Fong, Phys. Rev., 102, 434 (1956).

96. S.L. Whetstone, Jr., Phys. Rev., 114, 581 (1959).

97. P. Fong, Phys. Rev., 122, 1543 (1961).

98. R.B. Leachman, 'Some Recent Developments in Fission Physics', American Nuclear Society Meeting, Boston (1962).

99. S. Cohen and W.J. Swiatecki, University of California Radiation Laboratory Report UCRL-10450, (August 1962). Also, Ann. Phys., 22, 406 (1963).

100. J.R. Nix, University of California Radiation Laboratory Report UCRL-10695, (April 1963).

101. S. Cohen and W.J. Swiatecki, Ann. Phys., 19, 67 (1962).

102. J.R. Nix and W.J. Swiatecki, Nucl. Phys., 71, 1 (1965).

103. W.J. Swiatecki, Paper SM-60/1 in Ref. (51).

104. C.O. Minkkinen, in 'Collected Radiochemical Procedures', Los Alamos Report LA-1721 (1958).

105. F.J. Welcher, 'The Analytical Uses of Ethylenediaminetetraacetic Acid', published by D. Van Nostrand Co., Inc., New York (1957).

106. B.D. Pate and L. Yaffe, Can. J. Chem., 33, 15 (1955).

107. W.F. Boldridge and D.N. Hume, NNES, 9, Div. IV, Paper 294 (1951).

108. K.A. Kraus and G.E. Moore, J. Am. Chem. Soc., 75, 1460 (1953).

109. E.B. Sandell, 'Colourimetric Determination of Traces of Metals', published by Interscience Publishers, Inc., New York (1959).

110. B.D. Pate and L. Yaffe, Can. J. Chem., 33, 610 (1955).

111. B.D. Pate and L. Yaffe, Can. J. Chem., 33, 929 (1955).

112. B.D. Pate and L. Yaffe, Can. J. Chem., 33, 1656 (1955).

113. B.D. Pate and L. Yaffe, Can. J. Chem., 34, 265 (1956).

114. L. Yaffe and J.B. Fishman, Can. J. Chem., 38, 1113 (1960).

115. L. Yaffe and J.B. Fishman, 'Metrology of Radionuclides', International Atomic Energy Agency, Vienna, 1960, P. 185.

116. G.R. Grant, Thesis, McGill University (1961).

117. Nuclear Data Sheets - (National Academy of Sciences, National Research Council, Washington, D.C., 1959, 1960, etc.)

118. S. Meghir and L. Yaffe - to be published.

119. J.B. Cumming, Ann. Rev. Nuclear Sci., 13, 261 (1963).